Plasmonic Metasurfaces for Enhanced Pyroelectric Photodetection

by

Jon W. Stewart

Department of Electrical and Computer Engineering
Duke University

Approved:

____

Maiken H. Mikkelsen, Advisor

____

Steven A. Cummer

____

Michael E. Gehm

____

Willie J. Padilla

____

David R. Smith

Dissertation submitted in partial fulfillment
of the requirements for the degree of Doctor of Philosophy
in the Department of Electrical and Computer Engineering
in the Graduate School of Duke University

2020

ABSTRACT

Plasmonic Metasurfaces for Enhanced Pyroelectric Photodetection

by

Jon W. Stewart

Department of Electrical and Computer Engineering
Duke University

Approved:

Maiken H. Mikkelsen, Advisor

Steven A. Cummer

Michael E. Gehm

Willie J. Padilla

David R. Smith

Dissertation submitted in partial fulfillment
of the requirements for the degree of Doctor of Philosophy
in the Department of Electrical and Computer Engineering
in the Graduate School of Duke University

2020

Abstract

Thermal photodetectors are uniquely capable of sensing any incident wavelength and are only limited by the wavelength range of the integrated absorber, yet these detectors are commonly thought to be less sensitive and slower than their photoconductor (PC) or photovoltaic (PV) counterparts. As such, the use of thermal detectors for multispectral imaging has largely been ignored for spectral regions outside of the LWIR. However, recent theoretical and experimental developments have shown that thermal detectors with spectrally selective absorbers can outperform ideal PC and PV detectors in the MWIR and beyond. In this dissertation, thermal detectors integrated with spectrally selective, metasurface absorbers are theoretically and experimentally investigated. Large-area metasurface absorbers with resonances spanning from 340 to 2740 nm are developed that localize absorption and subsequent thermal generation in significantly subwavelength volumes. When integrated with a thermally sensitive pyroelectric film, the metasurface-pyroelectric detectors exhibit a sub-nanosecond response time with potential to match the response times of state-of-the-art, high-speed photodiodes. Overall, the spectrally selective thermal detectors developed here are a promising approach capable of disrupting the low cost, low form-factor spectral imaging market and providing an interesting platform to conduct research into photothermal generation and thermal diffusion at the nanoscale.

Dedication

For my wife and best friend, Ariana Stewart.

Contents

List of Tables

List of Figures

Acknowledgements

I would like to thank my advisor, Maiken Mikkelsen, for her mentorship and support during my graduate work. It is hard to recount everything I have learned under her mentorship, and I am grateful for the collaborative environment that she has cultivated in the group. I would like to thank Prof. Natalia Litchinitser, Prof. David Smith and Prof. Willie Padilla for allowing me to conduct research with their equipment.

I would like to acknowledge many of my colleagues. First, I would like to thank Dr. Jarrett Vella for training and teaching me about pyroelectric characterization and for all the pyroelectric samples. I would like to thank Dr. Gleb Akselrod for his mentorship and guidance during my first year. I would also like to thank my fellow lab-mates, Daniela Cruz, Qixin Shen, Wade Wilson, Andrew Boyce, Nathan Wilson, and Tamra Nebabu. I have enjoyed collaborating with all of you.

I would also like to earnestly thank my parents for participating in my education, pushing me to work through math textbooks during my summer vacations, and always believing I could accomplish whatever I set my mind to.

Last, I would like to thank Professors Maiken Mikkelsen, Steven Cummer, Michael Gehm, Willie Padilla, and David Smith for serving on my committee. I have thoroughly enjoyed discussing my research with you and I found our conversations helpful, stimulating, and challenging.

1. Introduction

Thermal photodetectors are uniquely capable of sensing any incident wavelength and are only limited by the wavelength range of the integrated absorber. Commercially, thermal detectors are commonly utilized for low-cost, uncooled photodetector arrays or focal plane arrays (FPAs) in the long-wave infrared (LWIR) where low-photon energies make photoconductive (PC) or photovoltaic (PV) detection difficult and noisy. Due to their low-cost, uncooled operation, and lower sensitivities than PC and PV FPAs, thermal FPAs are commonly used for civilian/non-military applications including autonomous vehicles, industrial process monitoring, firefighting, portable mine detection, night vision, and law enforcement.[1] Microbolometers are the most common thermal detectors comprising FPAs, however significant interest and recent research has been conducted on pyroelectric and thermoelectric approaches due to their higher thermal to electrical conversion efficiencies.[2–5]

The modern development of thermal detectors and nanophotonic absorbers promises to provide a new generation of low-cost, uncooled FPAs with broad wavelength ranges useful for a variety of spectral imaging applications. For example, three different PC and PV FPAs are required to cover the 400-2500 nm wavelength range due to their inherent sensitivity ranges. On the other hand, a single thermal FPA could potentially span this entire wavelength range reducing the cost, size, weight, and power use of a given spectral imaging system. An exemplary application requiring the full 400-

2500 nm range is aerial monitoring systems for agricultural crops, which are capable of identifying nutrient levels, stress, disease, insect attack, soil type, and overall health of crops.[6–12] This mapping of disease and nutrient levels could enable the targeted application of herbicides, pesticides, and fertilizers, referred to as 'precision agriculture'. This targeted application could reduce the amount of fertilizer by 4-46 percent, pesticide by 11-90 percent, herbicide by 28-70 percent, and water by 5-34 percent according to recent studies.[13,14] A low-cost, small form-factor spectral imager would enable farmers and companies to use small automated drones to monitor and track crop health cheaper and easier than chartering aircraft to fly the larger legacy spectral imagers.

For better insight into how thermal FPAs could disrupt the low-cost spectral imaging market, a better background on spectral imaging is provided. Spectral-based imaging relies upon the capture of spatial and spectral characteristics of scattered or emitted fields, providing unique information about the chemical or structural composition of the imaged object. Specifically for DoD applications, this technique enables the remote detection of chemical signatures useful for camouflage-environmental differentiation, harmful chemical mapping, civilian-military discrimination, and environmental characterization.[15,16] Typically, spectral imaging is categorized into either hyperspectral or multispectral imaging, where hyperspectral infers an approximately continuous sampling of the spectrum over a given range, and multispectral implies a rough or heavily discretized sampling. Spectral data is typically considered as a 3-dimensional 'data cube', where the first and second dimensions contain the spatial distribution of the incident field, and the third dimension encodes the spectral information for each spatial location. Measurement of hyperspectral data cubes has been realized through many approaches; however, the prevailing approaches capitalize on temporally multiplexing a 2D FPA—meaning two-dimensional slices of the cube are simultaneously captured by the 2D array and the cube is reconstructed by scanning over the third dimension and assembling these slices. For instance, one approach exploits a slit imaging system integrated with a diffraction grating to simultaneously capture a single spatial dimension and the associated spectral information on the photodetector array. Then the optical assembly is spatially scanned along the remaining spatial dimension to reconstruct the 3D cube. However, these techniques inherently require large, heavy, and often expensive opto-mechanical assemblies to spatially or spectrally scan the imaging system, which is not well suited for applications requiring small form factors and low weights.

One strategy to address this issue is to replace the scanning optical systems with focal plane arrays composed of spectrally selective pixels.[17–20] However, the poor spectral selectivity of naturally occurring materials beyond the visible spectrum makes the realization of spectrally selective pixels exceedingly challenging.[21] Bypassing the capabilities of natural materials, metasurfaces consisting of an ensemble of sub-wavelength resonators have demonstrated strong and spectrally selective absorption from the UV to mid-IR wavelengths, promising for the realization of multispectral devices. Recently, multispectral focal plane arrays have been demonstrated where each 'super-pixel' consists of a multitude of metasurface sub-pixels each with a unique spectral signature,[18–20] enabling the capture of both spectral and spatial dimensions simultaneously in an on-chip platform. For instance, a 3x3 super-pixel consists of nine different metasurface sub-pixels, which results in nine independent spectral points for each spatial location. Thus, this approach inherently trades off spectral and spatial resolution (e.g., if more spectral information is desired, larger super-pixels must be utilized, inherently reducing the spatial resolution). For applications with fixed, sparse spectral information, the reduced spatial/spectral resolution of multispectral imaging is typically not an issue. The use of thermal detectors and thermal FPAs for multispectral imaging has largely been ignored for spectral regions outside of the LWIR, however recent theoretical and experimental developments have shown that thermal detectors can outperform standard PC and PV detectors in the MWIR without the need for expensive cryocoolers or many stage thermoelectric coolers. In this dissertation, thermal detectors integrated with spectrally selective, metasurface absorbers are theoretically and experimentally investigated.

The remainder of this dissertation is organized as follows. First, in chapter 2 the theoretical limits of thermal detectors are derived and discussed for spectrally selective and unselective absorbers. Chapter 3 contains background on metasurface absorbers, plasmonics, and their associated fabrication. Chapter 4 includes my results on several colloidal metasurface absorbers that I experimentally and computationally investigated for photothermal conversion and subsequent integration with a thermal detector. In Chapter 5, I integrated a film-coupled metasurface absorber with a pyroelectric film to experimentally demonstrate a high-speed thermal detector, and my progress towards a multispectral thermal detector array is covered illustrating the promise of these pyroelectric-metasurface detectors.

2. Thermally Sensitive Photodetectors

Photodetectors leveraging thermally sensitive materials integrated with electromagnetic absorbers, such as bolometric, thermoelectric, and pyroelectric detectors are uniquely capable of sensing light at any wavelength. Light incident on these thermal detectors is absorbed and converted into heat, designated as photothermal conversion. The generated heat interacts with a thermally sensitive material converting the heat into an electrical signal. This thermal to electrical conversion is independent of the incident wavelength, as such the spectral dependence of a thermal detector is solely determined by the absorber. Traditionally, blackened absorbers comprised of thick disordered gold, aluminum, silicon, or carbon films[22–28] are utilized to provide the thermal detectors with a broad sensitivity range covering the visible (VIS) to long-wave infrared (LWIR). Metrology and spectroscopy systems such as FTIRs and laser power meters have found use for the broad sensitivity of thermal detectors, however the relatively low sensitivity of thermal detectors has discouraged their wide-spread usage when compared to photoconductors (PCs) and photovoltaic/photodiodes (PVs). Development of thermal detectors and associated FPAs has focused on low-cost, room-temperature, high-photon flux applications for the LWIR and very long-wave infrared (VLWIR), where thermal detectors can outperform PCs and PVs.[29,30] However, recent nanophotonic[31–33] and theoretical developments[21] have revealed that thermal detectors with spectrally selective absorbers could outperform their broadband counterparts, and even theoretically outperform PC and PV detectors under specific conditions in the MWIR and beyond.

Here recent nanophotonic developments and their impact on the sensitivity of thermal detectors are examined to challenge the idea that thermal detectors are less sensitive than PCs and PVs in the VIS to LWIR regime. Much of the thermal detector theory was developed in the mid-twentieth century following WWII[34–37] and prior to development of nanophotonic concepts and tailored thermal emission. More recently, an idealized thermal detector with a spectrally-selective absorber was analytically shown to outperform ideal PCs and PVs for wavelengths beyond the MWIR.[21] To better understand the mechanisms how nanophotonic absorbers can enhance thermal detectors, the thermal and noise dynamics are derived for both spectrally selective and unselective thermal detectors. The ensuing derivations reveal that the enhancement arises from the primary or secondary reduction in thermal fluctuation noise, thermal capacitance, and thermal conductance allowing for increased responsivities and decreased noise floors.

2.1 Ideal Thermal Detectors

For an ideal thermal detector, the dominant noise mechanism is assumed to be thermal fluctuation noise resulting from the random exchange of energy between a thermal mass and its surrounding environment. When in thermal equilibrium with the surrounding environment, the thermal noise power is expressed by Equation 1 below.[30,38,39]

$$\langle P_{th} \rangle = \sqrt{4k_b T^2 G_{th}} \tag{1}$$

Where k_b is the Boltzmann constant (1.38×10^{-23} [J·K^{-1}]), T is the temperature, and G_{th} is the thermal conductance between the detector and the environment. The thermal conductance [W/K] is a crucial parameter for thermal detectors and describes the ease at which the thermal energy can flow from the detector to the heat sink. For a fixed operation temperature, the thermal noise power will be minimized when G_{th} is minimized. As such, thermal detectors are typically isolated from their environment by suspension upon thin struts to minimize the heat flow to the environment. Equation 2 shows the thermal conductance for an isolated thermal detector.

$$G_{th} = \frac{1}{R_{th}} = G_{air} + G_{strut} + G_{rad} \tag{2}$$

The thermal conductance of such a detector to its surrounding environment accounts for multiple pathways including the conduction through air, G_{air}, conduction through the struts that suspend and thermally isolate the detector, G_{strut}, and thermal radiation conductance from the detector to the surrounding environment, G_{rad}. As such, the ideal thermal detector assumes the detectors are in a perfect vacuum and there is no conduction through the isolation legs, i.e. $G_{air} = G_{strut} = 0$. The thermal conductance from thermal emission/radiation when in equilibrium with the environment can be found from Equation 3.

$$G_{rad} = \frac{d}{dT}(A\sigma T^4\eta) = 4A\sigma T^3\eta \tag{3}$$

Where σ is the Stefan-Boltzmann constant (5.67×10^{-8} [$W\cdot m^{-2}\cdot K^{-4}$]), A is the detector area, and η is the detectors emissivity or absorptivity. This theory was derived when blackened metallic broadband absorbers were standard and as such, η is assumed to have little spectral dependence. Thus, the minimum detectible power or noise equivalent power (NEP) from an ideal thermal detector is given by Equation 4 with units of [$W\cdot Hz^{-0.5}$].

$$NEP = \frac{\langle P_{th}\rangle}{\eta} = \sqrt{\frac{16k_bT^5A\sigma}{\eta}} \tag{4}$$

The NEP is a parameter useful for quantifying the magnitude of radiant power incident on the detector that produces a signal equal to the root mean square (rms) noise. It is important to note, there is an ambiguity with the definition of the NEP as the units of [$W\cdot Hz^{-0.5}$] can be specified over the full operational bandwidth or for a 1 Hz bandwidth. Here the NEP will be specified with a 1 Hz bandwidth, and specific detectivity will account for the operational bandwidth of the detector. The normalized or specific detectivity, D^*, is another useful metric quantifying a detector's signal-to-noise (SNR) ratio at 1 W of input radiation normalized to the area and measurement bandwidth, Δf. The specific detectivity allows for comparison of detectors with different areas and bandwidths, where D^* for the ideal thermal detector is specified by Equation 5.

$$D^* = \frac{\sqrt{A\Delta f}}{NEP} = \sqrt{\frac{\eta \Delta f}{16 k_b T^5 \sigma}} \tag{5}$$

It is worth noting that the specific detectivity was originally formulated for quantum or photovoltaic detectors, where the noise power is proportional to the detector area. However, noise in thermal detectors does not always follow this scaling trend; for example temperature fluctuations do not necessarily scale with the detector area.[40] Thus, D^* should be interpreted cautiously as it tends to overestimate the performance of thermal detectors with larger areas and underestimate the performance of smaller detectors. Notwithstanding, D^* is a useful metric for general comparison of a detector's sensitivity, and in the case of an ideal thermal detector does capture the performance well as temperature fluctuations from thermal radiation do scale with area. The specific detectivity of the ideal thermal detector can thus be estimated by assuming $\Delta f = 1$ Hz, $T = 300$K, and $\eta = 1$. Under these conditions, the specific detectivity is 1.81×10^{10} [$cm\cdot Hz^{0.5}\cdot W^{-1}$], which is the maximum specific detectivity for a thermal detector with a broadband absorber. This specific detectivity for the ideal thermal detector is plotted in Figure 1 along with other experimental and theoretical detectors. From Figure 1, the ideal thermal detector can be seen to have worse performance than ideal PCs or PVs for all wavelengths shown which has led to the perspective that thermal detectors have slow response times and poor sensitivities. However, the ideal thermal detector derivation assumes a broadband absorber with a unity emissivity over the entire spectral range, which maximizes the thermal conductance from thermal emission for a given temperature. Recent theoretical developments have shown that the specific detectivity of thermal detectors can be substantially improved through integration with a spectrally-selective absorption and emission filters.[21]

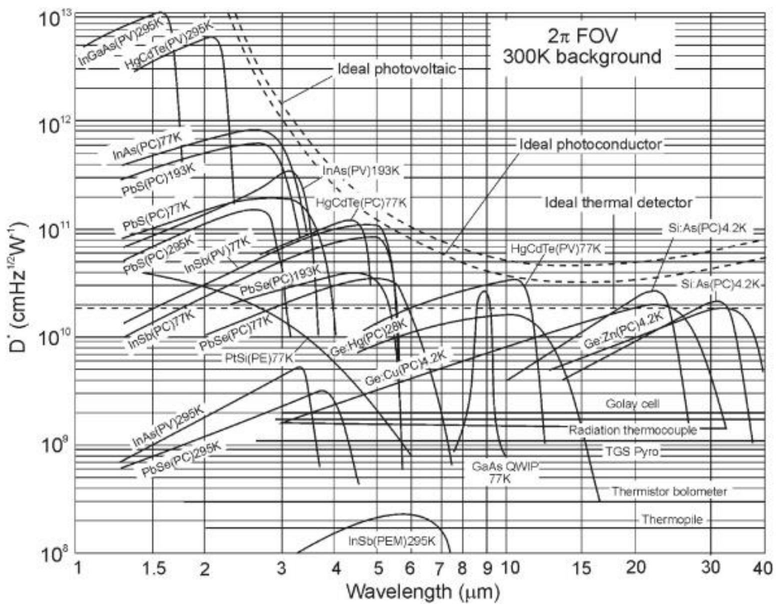

Figure 1: Comparison of the D* of common photodetectors. Chopping frequency is 1,000 Hz for all detectors except the thermopile (10 Hz), thermocouple (10 Hz), thermistor, bolometer (10 Hz), Golay cell (10 Hz), and pyroelectric detector (10 Hz). Each detector is assumed to view a hemispherical, surrounding at a temperature of 300 K. Theoretical curves for the background-limited D* (dashed lines), for ideal photovoltaic and photoconductive detectors and thermal detectors are also shown. PC, photoconductive detector, PV, photovoltaic detector, PEM, photoelectromagnetic detector, and HEB, hot electron bolometer. Figure from IOP Publishing.[41]

Conveniently, nanophotonic optical materials comprised of highly engineered subwavelength elements have enabled an unprecedented level of control over thermal emission and photothermal conversion.[42–46] By leveraging full control over the thermal emission spectrum, the radiative thermal conductance can be effectively reduced, which would increase the specific detectivity of an ideal, spectrally-selective thermal detector. Equation 6 describes the rms energy fluctuations arising from the photon quantization of the thermal radiation for a single frequency.[21]

$$\left\langle (\Delta E)^2 \right\rangle_f = N\left(hf\right)^2\left\langle n^2\right\rangle = \frac{8\pi h^2 f^4}{c^3}\frac{e^{\frac{hf}{k_b T}}}{\left(e^{\frac{hf}{k_b T}}-1\right)^2} \tag{6}$$

Where n is the number of photons in a mode, f is the frequency of the photon, N is the mode density in the region of interest, h is the Planck constant (6.626×10^{-34} [J·s]), and c is the speed of light. By integration over frequency and solid angle, the total rms energy fluctuations from thermal emission can be captured as shown in Equation 7.[21]

$$\left\langle (\Delta E)^2 \right\rangle = \int_{f_1}^{f_2}\int_0^{\pi}\int_0^{2\pi} \frac{2h^2 f^4}{c^3}\frac{e^{\frac{hf}{k_b T}}}{\left(e^{\frac{hf}{k_b T}}-1\right)^2}\eta\left(f,\theta,\phi\right)\sin\left(\theta\right) df d\phi d\theta \tag{7}$$

Equation 7 allows for calculation of thermal energy fluctuations $\langle(\Delta E)^2\rangle^{0.5}$ in units of [J·m^{-1}] from an arbitrary emissivity profile $\eta(f,\theta,\varphi)$. If the detectors are in thermal equilibrium with their surroundings and no substantial temperature changes occur during the measurement, the thermal fluctuations will be stationary. As such, the power spectral density can be calculated according to Equation 8 and the specific detectivity according to Equation 9.

$$\left\langle \left(\Delta P\right)^2 \right\rangle = \left\langle \left(\frac{\Delta E}{t_{meas}}\right)^2 \right\rangle = \left\langle \left(2\Delta f\,\Delta E\right)^2 \right\rangle = 4\left(\Delta f\right)^2 \left\langle \left(\Delta E\right)^2 \right\rangle \tag{8}$$

$$D^* = \sqrt{\frac{\Delta f}{\left\langle \left(\Delta P\right)^2 \right\rangle}} = \sqrt{\frac{1}{4\Delta f \left\langle \left(\Delta E\right)^2 \right\rangle}} \tag{9}$$

Where t_{meas} is the integration or measurement time and the measurement bandwidth $\Delta f = 0.5 \cdot t_{meas}^{-1}$. To minimize ΔE and maximize D^*, a nanophotonic absorber for a thermal detector should be designed to only absorb in the desired spectral region. This will reduce the number of absorbed/emitted photons at wavelengths unimportant to the designer, which leads to a significantly lower background noise when compared to a detector absorbing uniformly across the visible and infrared. Assuming a Lambertian thermal emission profile with a square spectral filter with a 1 μm spectral width centered at 10 μm, the specific detectivity would be ~5×10^{10} [$cm\cdot Hz^{0.5}\cdot W^{-1}$], which is almost three times more sensitive than the broadband thermal detector. With this simple filter, an ideal spectrally selective thermal detector would outperform ideal PC and PV detectors for wavelengths longer than 10 μm. If the integrated filter is improved to a 100 nm spectral width at 10 μm, the specific detectivity would increase to ~1.4×10^{11} [$cm\cdot Hz^{0.5}\cdot W^{-1}$], which would outperform any other detectors for wavelengths longer than 5 μm. The traditional notion that thermal detectors have worse sensitivities than PCs or PVs only holds for traditional blackened absorbers. Updated theories accounting for spectral selectivity and generation-recombination noise show that thermal detectors could potentially outperform other technologies in the MWIR and beyond.

2.2 Simple Thermodynamic Model

Apart from reducing the thermal conductance by spectrally screening unwanted thermal emission, nanophotonic absorbers can further improve thermal detectors by decreasing their thermal capacitance enhancing both the detector's sensitivity and response time. To understand the thermodynamics of such thermal detectors, a simple analytical solution is derived below. While the mechanisms of bolometric, thermoelectric, and pyroelectric detectors are quite different, the thermal design and isolation are similar between approaches which is shown in Figure 2. Most thermal detectors consist of a i) supporting film for the struts/thermal isolation, ii) electrical contacts, iii) a thermally sensitive material, and iv) an absorber. For example, the bolometer in Figure 2 consists of a i) 400 nm Si_3N_4 supporting film, ii) a Ti and Au electrical contact, iii) an 85 nm thermally sensitive VO_x film, and iv) an optical absorber from a 50/5/50 nm stack comprised of Si_3N_4/NiCr/Si_3N_4. Equation 10 is the simplest heat balance equation for a passive thermal detector for temperature fluctuations around an equilibrium temperature T. This equation assumes that little to no energy is removed from the system by the thermal to electrical conversion and that there are no influences from the electrical detection method such as bias currents for bolometric detectors.

$$C_{th}\frac{d}{dt}\Delta T + G_{th}\Delta T = \eta\Phi \tag{10}$$

Where C_{th} is the thermal capacitance, η is the absorption/emissivity at the wavelengths incident upon the detector, and Φ is the radiant power. The thermal capacitance in units of [$J \cdot K^{-1}$] is the capacity of the detector to hold thermal energy. Assuming a periodically varying radiant power, i.e. $\Phi = \Phi_0 e^{i\omega t}$, the amplitude of temperature variation is shown in Equation 11. The conversion factor of the given thermal detector in [$V \cdot K^{-1}$] or [$A \cdot K^{-1}$] is given by Equation 12.

$$\Delta T = \frac{\eta \Phi_0}{\sqrt{G_{th}^2 + \omega^2 C_{th}^2}} = \frac{\eta \Phi_0 R_{th}}{\sqrt{1 + \omega^2 \tau_{th}^2}} \tag{11}$$

$$K_V = \frac{\Delta V}{\Delta T}; K_I = \frac{\Delta I}{\Delta T} \tag{12}$$

Where thermal resistance is defined as $R_{th} = 1/G_{th}$, the characteristic response time is $\tau_{th} = C_{th}/G_{th}$, and K_V or K_I are the thermal to electrical conversion factors. The subsequent responsivity in [$V \cdot W^{-1}$] of the thermal detector is given by Equation 13.

$$R_V = \frac{K_V \Delta T}{\Phi_0} = \frac{\eta K_V R_{th}}{\sqrt{1 + \omega^2 \tau_{th}^2}} \tag{13}$$

Equation 11 and 13 illustrate several important features of thermal detectors to maximize ΔT and R_V for a given radiant power. In order to maximize the temperature change, ΔT, the thermal capacitance and conductance need to be minimized, while maximizing the absorption for the wavelength of interest. It was shown with Equation 7 that an ideal absorber for a thermal detector should perfectly absorb the signal wavelength and have no absorption otherwise. This allows for complete absorption of the signal, while reducing the thermal conductance associated with thermal emission to the detector's surroundings. As such, thermal detectors should seek the smallest possible detector mass, minimize thermal emission, and utilize the thinnest/longest thermal isolation legs possible to connect the detector to the heat sink.[47] Temporally as ω is increased, the $\omega^2 C_{th}^2$ term will eventually exceed the G_{th}^2 term in magnitude and ΔT will decrease inversely as ω. Thus, the characteristic response time, $\tau_{th} = C_{th}/G_{th}$, is analogous to the RC time constant of an RC (resistor and capacitor) circuit and models the thermally limited response of the detectors. An optimal thermal detector would have the smallest thermal capacitance possible and the thermal conductance would be engineered to achieve the desired response time and noise floor.

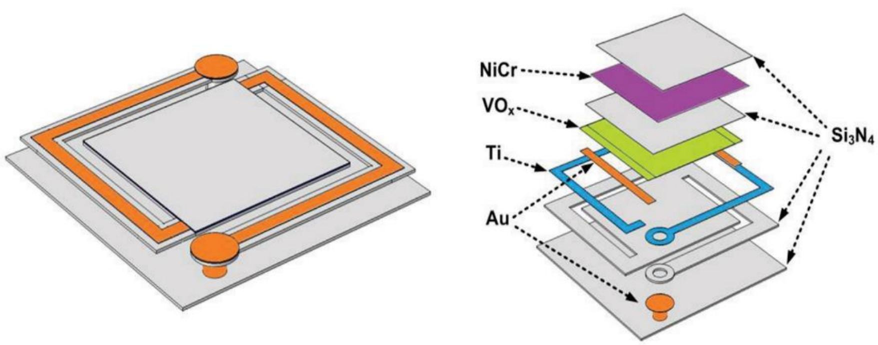

Figure 2: Geometry and composition of thermally isolated thermal detector. A 25x25 μm VOx microbolometer is shown here, where the resistance of the VOx changes in response to the temperature of the film. Two thermal isolation struts can be seen along the outside of the detector that connect it to the substrate with 4 μm widths and 50 μm lengths. The Ti and Au conductors are used to electrically contact the thermally sensitive VOx film of 95 nm in thickness. The 400 nm Si_3N_4 film at the bottom of the heterostructure is the film supporting the structure, and the top Si_3N_4/NiCr/Si_3N_4 stack is the optical absorber with thicknesses of 50/5/50 nm. Figure adapted from AIP Publishing.[48]

Focusing on the absorber, the use of nanophotonic absorbers due to their subwavelength features and localized absorption can directly reduce the thermal capacitance of the detector, which will result in an increased responsivity and improved thermal response time. Additionally, these absorbers can have a secondary effect of reducing the thermal conductance in addition to the reduction of the thermal emission. Equation 2 showed that the thermal conductance depends on the physical design of the detector support structure or the isolation struts. The support structure itself is designed to provide mechanical support for the contacts, thermally sensitive, and absorber materials. As such, if the absorber mass is decreased, the struts can be made thinner and longer while providing the same comparative support. The strut conductance can be modeled as the sum of individual materials comprising the strut as shown by Equation 14.

$$G_{strut} = N_{strut} \sum_i \frac{k_i A_i}{\ell_i} \tag{14}$$

Where N_{strut} is the number of struts isolating the detector, k_i is the thermal conductivity, A_i is the cross-sectional area, and ℓ_i is the length of the strut for the i^{th} material. In most cases, the strut only consists of i) a low stress oxide or nitride film acting as the support for the detector structure and ii) a conductor to electrically contact the thermally sensitive material as shown in Figure 2. For recently demonstrated microbolometers, the struts commonly have thicknesses on the order of 100's nm, widths on the order of 1's μm, and lengths in the 10's μm resulting in ~10^{-7}-10^{-8} [$W\cdot K^{-1}$]

strut conductances.[1,47,49–53] Other than improved fabrication techniques and design, there is little that can be done to reduce the thermal conductance of the strut other than reducing the mass of the suspended thermal detector. This reduction in the detector mass, from integrating a nanophotonic absorber for instance, would allow for the struts to be thinner and longer reducing the thermal conductance and improving the specific detectivity. In a similar form to the thermal conductance, the thermal capacitance can be minimized directly by reducing the mass of the thermal detector. The thermal capacitance as calculated by Equation 15 is found from the sum of capacitances for each constituent material.

$$C_{tot} = \sum_i C_i \tag{15}$$

$$C_i = c_{pi} \rho_i V_i \tag{16}$$

C_i is the thermal capacitance of the i^{th} material in the detector heterostructure, which is calculated from the specific heat c_{pi}, the density ρ_i, and the volume V_i for the i^{th} material. The thermal capacitance can be minimized by reducing the volume of the support, contacts, thermally sensitive, and absorber materials while choosing materials with low densities and specific heats. Any reduction in the absorber or thermally sensitive material would allow for a concomitant reduction in the support material, which compounds the reduction in thermal capacitance. Since the absorber and thermal-electrical conversion can be designed separately, each can be optimized independently.

For a specific thermal detection mechanism, such as bolometric, pyroelectric, or thermoelectric detectors, the thermally sensitive elements and contacts will be optimized and effectively fixed to produce the largest responsivities. The thermal to electrical conversion will be optimized according to the NEP and D^* shown in Equations 17 and 18.

$$NEP = \frac{V_{noise}}{R_V} = \frac{I_{noise}}{R_I} \tag{17}$$

$$D^* = \frac{\sqrt{A\Delta f}}{NEP} = \frac{\sqrt{A\Delta f}}{V_{noise}} R_V \tag{18}$$

Where V_{noise} is the rms voltage noise in [$V \cdot Hz^{-0.5}$] arising from the various noise sources of the thermal detector. Equation 18 demonstrates, that the specific detectivity is directly proportional to the responsivity of the detector and inversely proportional to the noise. Since the absorber and thermal to electrical conversion mechanism are assumed to be independent, the thermal to electrical conversion can be optimized by minimization of the noise to responsivity ratio or the NEP. The thermal to electrical optimization will be specific to the desired mechanism and material system, and the selection of the optimal parameters for each mechanism and material system is beyond the scope of this work. For the remaining section, the thermal to electrical conversion mechanism will be assumed to be optimized in terms of minimizing noise and maximizing responsivity through geometrical and material selections. In this case, the only further improvement to such a thermal detector is through the absorber design. Theoretically, these derivations have shown that nanophotonic absorbers can directly enhance the sensitivity of thermal detectors through the primary or secondary reductions in thermal fluctuation noise, thermal capacitance, and thermal conductance.

2.3 Nanophotonic Absorbers for Thermal Detectors

Recent experimental developments in nanophotonics has allowed for the creation of laterally and vertically structured optical absorbers that localize incident electromagnetic energy into significantly subwavelength volumes. This localization allows the volume and mass of a spectrally selective optical absorber to be minimized. For instance, a perfect absorber can be realized with an array of holes in a metallic or semiconductor film,[54] where the holes not only improve the ability of the film to absorb incident radiation but also reduce the thermal capacitance of the absorber. In general, an ensemble of nanophotonic components on a surface can be designated as a metasurface or metamaterial. Metasurfaces can be split into two main categories dielectric/semiconductor metasurfaces and metallic/plasmonic metasurfaces, which are classified according to the materials comprising the nanophotonic elements.

Each thermal detection has unique mechanisms responsible for the electrical to thermal conversion, and the nanophotonic absorber must be designed around this mechanism so not to adversely impact its' performance. Recent demonstrations of nanophotonic absorbers with the three main thermal detector approaches (i-iii) are examined briefly below. i) Bolometric detectors measure thermal signals through the temperature-dependent electrical resistivity of a thin material such as amorphous Si or VO_x films. Typically, a bias current is applied to a bolometric detector and any resultant change in the electrical current can be attributed to thermal changes of the material. As such, dielectric metasurfaces are commonly used for bolometric detectors in order to prevent any leakage currents from flowing through the absorber.[33,50] However, metallic metasurfaces have been integrated with bolometric films by utilizing nanostructured metallic contacts to simultaneously inject current into the bolometric film while providing an enhanced absorption.[55–57] ii) Thermoelectric/thermocouple detectors operate from charge transfer across a heterojunction of two dissimilar metals or a p- to n-type semiconductor junction with different Fermi levels. A temperature difference sustained across the junction allows higher temperature/energy charges in the hot material to generate a diffusion current into the cold material creating a voltage across the junction. The Seebeck coefficient is used to describe the magnitude of this effect and has units of [$V \cdot K^{-1}$]. Nanophotonic thermoelectric detectors have been demonstrated with both dielectric and metallic metasurfaces depending upon the contacting geometry and materials used for the thermoelectric junction.[32,58–61] iii) The mechanisms of pyroelectric detectors are discussed in more detail in section 5.1, but are essentially capacitors where the pyroelectric material is sandwiched between two conductors. In this case, a metallic absorber with minimal thermal capacitance is desired to generate the largest signal with recent demonstrations showing pyroelectric detectors with sensitivities ranging from the visible (~600 nm) to millimeter (~2 mm).[19,31,62,63]

3. Plasmonic Metasurface Absorbers

Metasurfaces are crucial for next generation thermal detectors, since they allow for unparalleled control of electromagnetic waves that circumvent the limitations of naturally occurring optical materials. For these thermal detectors, light absorption and subsequent thermal generation is essential, but natural materials in the UV to MWIR have limited absorption ranges corresponding to inherent electron and phonon excitations. Metallic metamaterials on the other hand can be designed to realize high-efficiency absorption for nearly any wavelength by taking advantage of metallic nanostructures with recent demonstrations spanning from the UV to millimeter regimes.[31,62,64–69]

3.1 Plasmonic Nanocavities for Metasurfaces

Metallic nanostructures with subwavelength features enable unprecedented control of interactions between optical waves and nanoscale materials through the exploitation of localized surface plasmon resonances. Light incident upon the metallic nanostructures excites localized surface plasmons i.e., coherent oscillations of free electrons confined to the surface of a highly conductive material. These plasmons are resonant oscillations that are highly dependent on the geometry and materials of the metallic nanostructures, and as such are highly suited for designable metamaterials. Plasmonic metasurfaces in the visible to near IR regime have exhibited wide spectral ranges, non-fading colors, and have been demonstrated for a diverse set of applications ranging from photodetection[70–79] to color printing.[80–84] A promising geometry capable of constructing strongly absorbing, spectrally-narrow metasurfaces is the gap-plasmon resonator or plasmonic nanocavity[71,73–76,78–82] due to its high field enhancements,[85–89] strong resonant modes,[90,91] and large electric and magnetic responsivities.[67,92,93] When packed to a specific surface density, the collective electric and magnetic response can destructively interfere with incident radiation, resulting in near perfect absorption at the plasmon resonance as shown in Figure 3.[94,95]

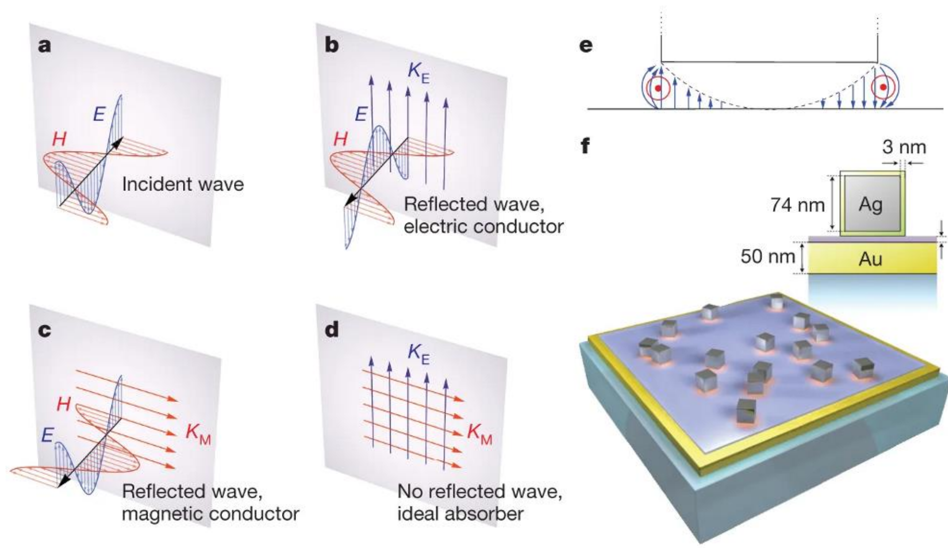

Figure 3: Perfect Absorbers with Plasmonic Metasurfaces. a) Light incident on a conductive surface. b) Light reflects due to either the excitation of electric surface current densities, K_E, or c) fictitious magnetic surface current densities, K_M. d) If both responses exhist then the back reflected wave represents the electric field response, E, and the magnetic field response, H, which can exactly cancel the reflected wave. e-f) A plasmonic-based absorber formed by an ensemble of plasmonic nanocavities for which the enhanced electric field (blue) is equivalent to effective magnetic currents (red). Figure adapted from Nature Publishing.[67]

Typically, these gap-plasmon or plasmonic nanocavity structures are realized by realized by separating nanoscale metallic particles, such as cubes,[65] platelets,[96] disks,[92] or other facetted shapes[97–99], from a smooth metallic film with a dielectric spacer to create two planar metallic surfaces. Coupling between the two planar plasmonic surfaces makes the nanocavity which confines or localizes generated plasmons at the interface between the metallic NPs and the metal films. Thus, these nanocavities can generate the large electric and magnetic responses needed for perfect absorption and integration with thermal detectors.

3.2 Metasurface Fabrication Approaches

Typically, in the visible and infrared spectral ranges, high-resolution photolithography or electron beam lithography is needed because individual coupled-mode plasmonic resonators need to have feature sizes down to ~10 nm.[89,100,101] State-of-the-art, top-down lithographic patterning with 10 nm resolution, such as electron beam lithography, not only inherently limits the scalability and commercialization potential of metasurface absorbers, but also typically deteriorates the properties and interfaces of any electrically active material exposed to the process. Techniques such as i-Line stepper photolithography can readily pattern lateral feature sizes down to 300 nm, which is useful for metasurfaces at longer wavelengths, but realizing controllable, economical, and wafer-scale patterning below 40 nm has been an active area of research. Lithography-free approaches such as planar metasurfaces have shown spectrally-selective absorbing surfaces from visible to mid-wave infrared,[102–107] but lack full spatial control over the absorbed power and heat generation. Alternative fabrication techniques, such as imprint lithography[108,109] and colloidal self-assembly,[110] have showed promise for realizing ~10 nm resolutions over wafer-scale areas with non-damaging fabrication strategies. As such, a scalable, facile metasurface fabrication technique would play a crucial role in facilitating technology transfer and development of novel optoelectronic devices in the 400-3000 nm regimes.

Focusing in, colloidal fabrication approaches are uniquely capable of producing large-area plasmonic metasurfaces with nanometer accuracies with a range of techniques using the NPs as etch masks for an underlying metal film,[66] shadow deposition masks to pattern a deposited metal,[111] or through direct use of metallic NPs.[67,110,112] Recent demonstrations in Prof. Smith[64,87,110,113] and Prof. Mikkelsen's[65,112,114] group have shown plasmonic metasurfaces with attractive absorptive properties by depositing silver nanocubes onto metallic films with a dielectric coating as shown in Figure 4. These spectrally selective metasurfaces have been shown to absorb from 650 to 1420 nm, where the absorption resonance is passively tuned by changing the cube size between 75-140 nm or the dielectric spacer thickness between 1-7 nm. Furthermore, these Ag nanocube metasurfaces were deposited over an entire 50 mm wafer and showed little to no variability over the entire surface, promising for future large-area device fabrication.

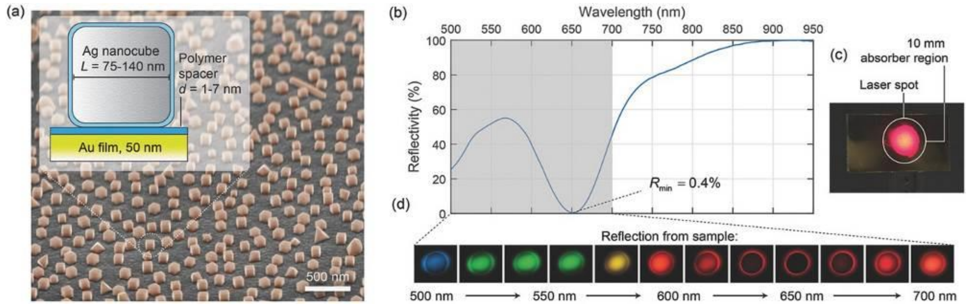

Figure 4: Metasurface Perfect Absorber Based on Colloidal Silver Nanocubes. a) SEM image of perfect absorber surface consisting of a gold film covered with silver nanocubes, where the inset shows the dimensions of the metasurface elements. b) Reflection spectrum from an absorber with a resonance at 650 nm, utilizing 75 nm nanocubes and a 7 nm spacer. c) Picture of sample with a 10 mm metasurface, while surrounding region is coated only with gold. A defocused laser with a diameter of ≈13 mm illuminates the absorber region. d) Images of the laser beam after reflection from the absorber sample shown in (c), as the laser wavelength is swept from 500 to 700 nm. Figure from Wiley Publishing GmbH.[110]

However, the creation of practical thermal detectors and optoelectronic devices based on these plasmonic nanocavities is contingent upon a fabrication method providing full control on multiple length scales. First, the plasmonic gap needs to be fabricated with nanometer accuracies in order to consistently control the plasmon resonance. Second, the sub-wavelength plasmonic resonators must be arranged spatially to form an impedance matched metasurface, resulting in perfect absorption on resonance. Third, these metasurfaces must be patterned on the micron scale into individual pixels forming multispectral arrays and finally the pixels must be patterned over wafer-scale areas to allow the fabrication of large-scale devices. To date, such plasmonic devices have yet to be demonstrated due to the lack of suitable fabrication methods with these multiscale properties. As such, these colloidal self-assembly approaches are capable of nanometer scale accuracies over wafer-scale area, but lack the capability to laterally pattern the metasurfaces into pixel arrays. In order to improve these colloidal metasurfaces for practical fabrication of thermal detectors, section 4.1 outlines my effort to hybridize colloidal self-assembly with photolithography to make multispectral metasurface arrays, and in section 4.2, I demonstrate the ability of colloidal metasurfaces to spatially control nanoscale thermal generation from light absorption spanning from 340-2740 nm.

4. Colloidal Metasurfaces for Thermal Detectors

4.1 Multispectral Metasurface Arrays

In this section, I demonstrate the creation of spectrally selective, highly absorbing metasurface pixel arrays exhibiting greater than 85 percent absorption and ~100 nm spectral widths by patterning plasmonic resonators in micron-scale pixels using a fusion of bottom-up and top-down fabrication techniques over wafer-scale areas. The plasmonic resonators, tuned from 580 to 1125 nm, are composed of colloidally synthesized silver nanocubes separated from a gold film with a 4 to 10 nm spacer layer. To display the capability of this technique, I fabricate a multispectral metasurface pixel array consisting of six resonances and reconstruct a RGB image with a combinatorial pixel scheme exhibiting 9261 color combinations.

The presented multiscale fabrication method utilizes a combination of bottom-up colloidal assembly to form the individual resonators and top-down photolithography to define the deposition of metasurfaces into multispectral patterns over multiple length scales. The only steps required for this process are dip coating, photolithography, and colloidal synthesis, which inherently makes this fabrication method appealing for large-scale device fabrication. Leveraging this fabrication technique, two structures were fabricated demonstrating the unique capabilities of this plasmonic system. First, a wafer-scale multispectral metasurface pixel array was fabricated with six different resonances spanning from 580 to 1125 nm. Second, an RGB image was reconstructed in the near-IR with combinatorial metasurface pixels that achieve 9261 different color combinations.

The plasmonic metasurfaces are formed from colloidally synthesized metal nanocubes deposited on top of a metal film and separated by a polymer spacer with nanometer accuracies as shown in Figure 5. There are several appealing nanoscale properties of this plasmonic architecture. First, the plasmon resonance between the metal nanocubes and the film can be precisely controlled by varying the thickness of the gap layer, d, and the cube size, L, enabling the resonance to be tuned anywhere from 580 nm to 1420 nm.[65] Secondly, the gap size can be precisely maintained for individual particles across arbitrarily large samples through uniform coating techniques such as dip-coating or atomic layer deposition. Furthermore, the effective properties of the surface can be tuned by varying the density of the nanocubes or by utilizing other plasmonic materials such as aluminum or silver.

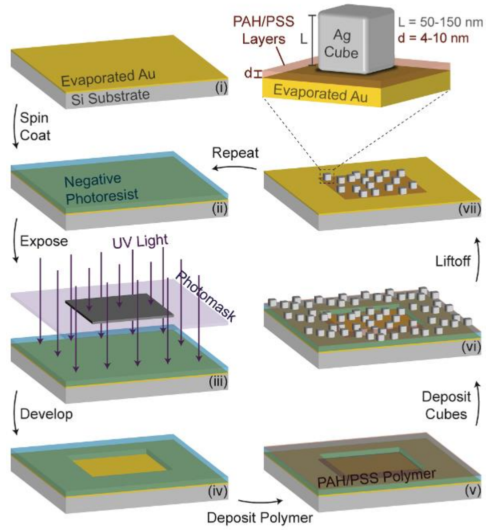

Figure 5: Multispectral Metasurface Fabrication Procedure. Diagram illustrating the fabrication steps used to create multiple different self-assembled metasurface pixels on a single substrate. On the top right is a schematic of a single subwavelength absorber consisting of a silver nanocube separated from a gold substrate with a 4 to 10 nm polymer spacer layer. Figure from Wiley Publishing GmbH.[112]

A summary of the fabrication steps used to create the multispectral metasurfaces is illustrated in Figure 5, where the process utilizes colloidally synthesized silver nanocubes, layer-by-layer deposition of polyelectrolytes, and repeated lift-off photolithography. Initially, a gold film is evaporated on a silicon substrate (i) followed by spin-coating of a negative photoresist (ii). Next, a photomask is used to determine the nanocube deposition area by exposing (iii) and developing (iv) the photoresist. A nanoscale spacer layer is then deposited using layer-by-layer dip coating of alternating polyelectrolyte (PE) layers composed of a positively charged poly(allylamine) hydrochloride (PAH) polymer and a negatively charged polystyrene sulfonate (PSS) polymer with layers of ~1 nm thickness (v).[115] Next, the substrate is incubated in a solution of nanocubes, where the nanocube stabilizer coating is PVP, a negatively charged polymer, which facilitates the nanocubes to electrostatically adhere to the positively charged PE layer. The final film-nanocube separation distance is the sum of the PE layers and the 3 nm stabilizer coating. The silver nanocubes themselves are colloidally synthesized following a well-established process.[116,117] Lastly (vii), the photoresist is removed, leaving nanocubes only in the defined regions. This fabrication process can be utilized to pattern any number of different nanocube resonances created with different gap thicknesses and nanocube sizes across large-scales by repeating the process starting with step (ii). The result of this process is a sample with film-coupled plasmonic resonators with nanometer gap precisions, patterned into micron-scale pixels via photolithography over wafer-scale areas. This fabrication method can be extended to high-volume fabrication by automating the photolithography process with commercially available machines and by dip-coating many substrates in parallel in polymer and nanocube baths.

Utilizing this method, a multispectral pixel array with six different metasurface resonances was patterned as illustrated in Figure 6. A photomask that consisted of 20x20 μm squares determined the locations of the nanocube deposition and the fabrication steps depicted in Figure 5 were repeated for each resonance. Resonances were chosen to vary from 580 nm to 1125 nm by using three different gap thicknesses, d, and three different sizes of nanocubes, L (Figure 6b). The SEM image in Figure 6a shows the uniform patterning of the multispectral pixel array over a small region of the full sample which covers a 1x1 cm area. The basic pixel unit of this structure is shown in Figure 6b where the cube sizes and gap thicknesses for each pixel are also indicated. The SEM image in Figure 6c shows that the metasurfaces are composed of an ensemble of randomly oriented nanocubes which also can be seen in an angled SEM in Figure 6d. The spectral response of each individual resonance was measured with a spectrometer with an integrated spot size of 5 μm in diameter and is shown in Figure 6e.

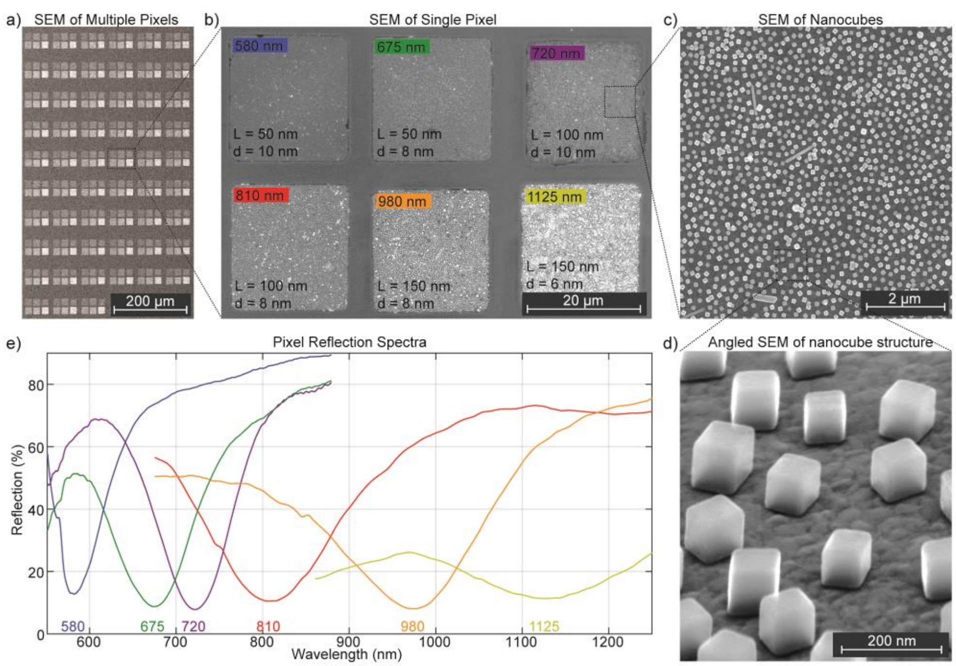

Figure 6: Multispectral Pixel Array. a) SEM image of multiple pixels showing the uniformity of patterning. b) SEM image of a single pixel labeled according to their corresponding spectrums. The nanocube size, L, and the gap thickness, d, are labeled for each resonance. c) SEM image of the uniform distribution of cubes within the 20x20 μm squares. d) Angled SEM image showing silver nanocubes (L = 75 nm) on a gold substrate. e) Spectrum of six different plasmonic resonances across the visible to near infrared patterned on a single substrate. Figure from Wiley Publishing GmbH.[112]

By fitting the spectra of each metasurface with a Lorentzian lineshape, the best quality factors were determined to be 8.7 for the 580 nm resonant pixel and 6.3 for the 720 nm pixel. An analysis of the SEM image in Figure 6c reveals that 88% of the particles in the 720 nm metasurface were cubes with a ±6 nm size distribution as shown in Table 1 of the supplementary information. Figure 12 and Table 1 display the analysis results for the other metasurface pixels. The residual particles in the size distribution statistics are either clustered nanocubes, pyramids, rods, or other shapes. A peak absorption upwards of 85% on resonance was achieved for each patterned metasurface. In this sample, the highest absorption peak of 90% occurs for the 720 nm resonance, which had the highest nanocube fraction of 88% with a ±6 nm size distribution that filled 16.1% of the surface area. The nanocube absorbers have previously demonstrated absorptions up to 99.7% where the solution was 91% nanocubes with a ±6 nm size distribution that filled 19.2% of the surface area and maintain absorptions above 95% out to 50 degree angles of incidence.[37] The smaller peak absorptions observed in this work might be due to residual photoresist on the gold surface or interference of the photoresist walls with nanocube diffusion and adhesion causing the lower fill fractions exhibited here. While factors potentially weaken the absorption performance of the metasurfaces, the performance could likely be improved with commercial photoresists or filtering the nanocube solutions to remove undesired larger particles.

Taking advantage of this multiscale fabrication technique, a second structure was designed that could reconstruct an arbitrary macroscopic RGB image using combinatorial plasmonic pixels as depicted in Figure 7. Former plasmonic image reconstruction techniques have typically relied upon small variations in the plasmonic resonator to create up to 100 different colors with spatial resolutions up to ~100,000 dots per inch (dpi).[70–77,79] Several recent approaches have demonstrated the capability of combinatorial plasmonic pixels to achieve a higher number of colors.[78,81] The multiscale fabrication technique presented here is uniquely suited to the creation large-area plasmonic pictures reconstructed through the combination of multiple elemental colors with different intensities such as in RGB or CMYK displays. The upper limit on the amount of colors is determined by the desired dpi and the accuracy with which the metasurfaces can be patterned. Here, each "RGB" pixel is mapped to a 45x45 μm square where the pixel color is changed by varying the length of a rectangular-shaped subpixel metasurface as depicted in Figure 7a. With 2 μm variations in length and a maximum length of 40 μm, each plasmonic subpixel can achieve 21 different absorption intensities for each color corresponding to 1 percent variations in the absorption of the R, G, or B channels which is easily measurable on commercial spectrometers. Thus, with the 2 μm variations, this pixel scheme is readily capable of creating 9261 color combinations at a resolution of 560 dpi. An SEM picture in Figure 7b shows pixels with varying "RGB" sizes that were fabricated. With this reconstruction method, each "RGB" channel can be mapped to any color between 570 nm to 1420 nm. In this specific case, the R channel was mapped to 810 nm, the G to 720 nm, and the B to 570 nm as shown in the spectrum of Figure 7e. Normalized microscope images of pixels were taken with ±10 nm bandpass filters around each resonance, shown in Figure 7f. The strong selectivity of the bandpass filters on the metasurfaces can be seen in the microscope images where the on-resonant pixels appear black.

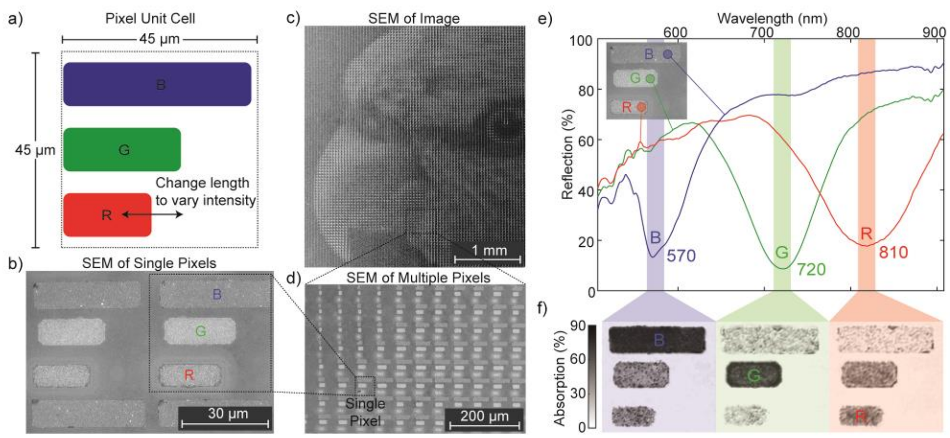

Figure 7: Metasurface RGB Pixel Structure. a) Diagram of the pixel unit cell used to reconstruct an RGB image with the nanocube absorbers. The intensity of each color is tuned by varying the length of the rectangles in 2 μm increments. b) SEM image depicting actual pixels of the reconstructed RGB image. c) SEM image showing pixels with varying rectangle lengths along edge of parakeet head. d) SEM image of the parakeet head. e) Spectrum of three different colors used to reconstruct the RGB image. f) Images of pixels taken with ±10 nm bandpass filters around each resonance. Figure from Wiley Publishing GmbH.[112]

An RGB image of a rainbow lorikeet was chosen to be reconstructed with the nanocube absorbers (Figure 8) and the image was down sampled from 256 intensities to the 21 intensities possible with the reconstruction method described above. Each pixel was then converted into three photomasks for the three different nanocube resonances needed. An SEM image demonstrating the variation of pixels along the edge of the lorikeet head is shown in Figure 7d. A macroscale SEM image in Figure 7c clearly shows how the lorikeet head is composed of individual three-color pixels. The sample was imaged with a custom built imaging system, in a white light reflection mode. The same bandpass filters used for Figure 7d were installed in front of the CCD camera, and the images were normalized for each different filter. Figure 8a shows images of the lorikeet in the separate color channels, with the images shown in false RGB color. The reconstructed image of the lorikeet head is shown in false color in Figure 8c with all three color channels. The image was reconstructed by simply resizing and superimposing the images to account for chromatic aberrations in the imaging system. The aliasing of the images is a result of slightly oversampling the image to where the individual pixel structures could be resolved. The original down-sampled image is shown for comparison in Figure 8b. The red hue is observed to be less vibrant in the reconstructed metasurface image compared to the original, which is likely due to a slight degradation of the sample that occurred between fabrication and measurement. Typically, the PVP coating around the silver nanocubes protects the sample from degradation for up to a week, however the acetone liftoff used in the fabrication process affected the PVP coating resulting in faster degradation such as in the red pixels. The spectral effects of further oxidation on the sample can be seen in Figure 11. However, this image reconstruction is a clear visual demonstration of the precision with which the nanocube absorbers can be patterned on a macroscopic scale, with much finer features possible, limited only by the photolithography resolution.

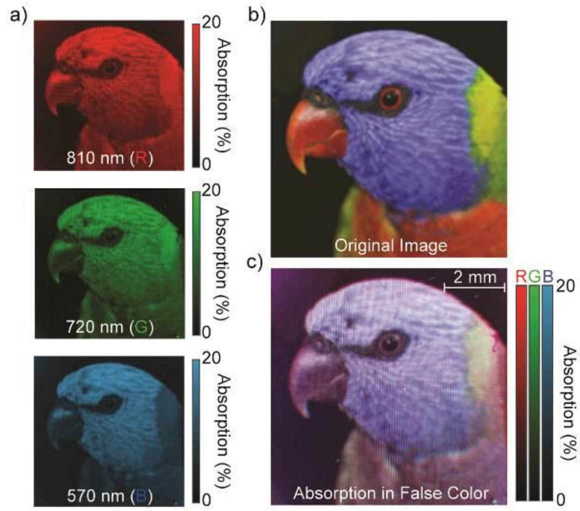

Figure 8: Reconstructed RGB Image. a) Absorption images at the three different resonances taken with same bandpass filters as in Figure 3f. b) Original down-sampled image used to create the photomasks. c) The final reconstructed image from the three different absorption images. Figure from Wiley Publishing GmbH.[112]

The original 330x330 pixel parakeet image was reconstructed using 45x45 μm plasmonic pixels, which corresponded to a final 15x15 mm plasmonic picture. Figure 9 shows a scattered light image from the 15x15 mm lorikeet sample as well as the original image used for the reconstruction, which has been downsampled from 256 to 21 intensity variations. The reflection imaging setup used to image the lorikeet head is only capable of achieving a 6 mm field of view. A custom imaging setup was built with normally incident white light and a relatively large field of view. Utilizing two high NA and low magnification objectives, I achieved an imaging system with a magnification of 0.3X with low aberrations. This system could provide uniform illumination over a field of view of 6 mm by adjusting the focus of the beam using the collimating lens. A broadband 50/50 beam splitter was used to couple the white light into the path for normally incident reflection measurements.

Figure 9: Full-sized Images of Original and Reconstructed Lorikeets. The original 330x330 pixel image is shown on the left downsampled from 256 to 21 intensity variations. The scattering off the reconstructed plasmonic image is shown on the right for the full 15x15 mm sample size. Figure from Wiley Publishing GmbH.[112]

The metasurfaces are robust against the use of common photoresist solvents and developers. The spectra of the 580 nm resonant pixel are shown below in Figure 10 before the acetone liftoff, after one liftoff, and after three liftoffs. The acetone liftoff has little to no effect on the reflection spectrum of the metasurfaces, indicating that the liftoff does not change the density or adhesion of the nanocubes. The absorption peak of the reflection spectra does not significantly change on resonance. The off-resonance changes are a result of varying normalization effectiveness.

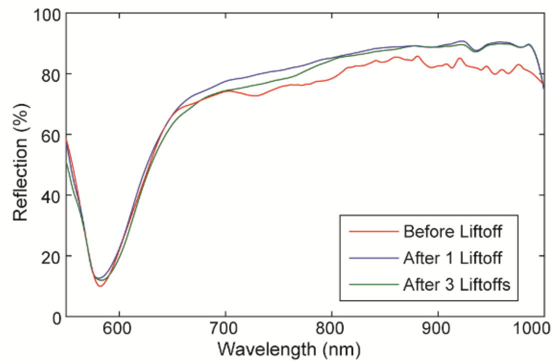

Figure 10: Reflection Spectra Before and After Liftoff. The reflectance of the 580 nm pixel in the metasurface array was taken before and after several acetone liftoffs to assess the effect of solvents on the metasurface. Figure from Wiley Publishing GmbH.[112]

One adverse effect of using the solvents was that the oxidation rate of the silver nanocubes increased due to the removal of the PVP stabilizer coating protecting the cubes. Thus, the faster degradation of the red pixels of the reconstructed parakeet image were attributed to the oxidation of the nanocubes between measuring the spectrum and taking the macroscale reflection image. Typically, the 3 nm PVP stabilizer coating prevents the silver nanocubes from oxidizing for up to a week in ambient conditions. However, the red pixels in the parakeet image were exposed to an acetone liftoff first which damaged the PVP stabilizer resulting in faster oxidation rates compared to the blue or green channels. The spectra of the RGB pixels is shown in Figure 11 before and after oxidation. As the samples oxidize the spectral selectivity and absorption is destroyed.

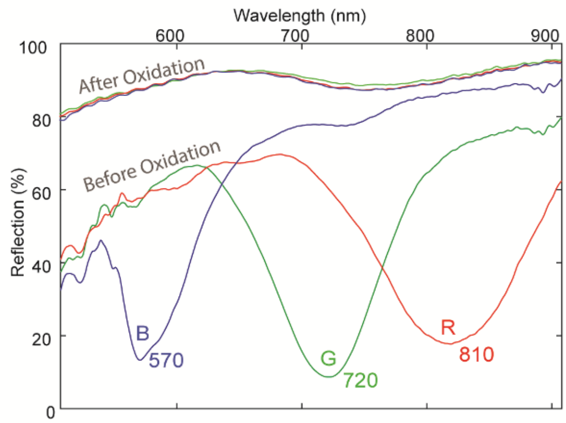

Figure 11: Oxidation of Metasurfaces. The reflectance spectra for the RGB image reconstruction are shown before and after oxidation. The oxidized spectra were taken after the sample was exposed to ambient conditions for over a week. Figure from Wiley Publishing GmbH.[112]

The absorption performance of the metasurface is directly related to three main characteristics of the colloidal particles on the surface. These characteristics can be determined through analyzing SEM images of the surfaces for each nanocube solution (Figure 12). First, the fill-fraction of the nanocubes on the gold substrate will determine the effective impedance of the surface and will change the magnitude of the absorption peaks on resonance. Second, the percentage of nanocubes versus other types of particles will determine the peak absorption of the sample. Other particles scatter light resulting in worse absorption performance and will increase the FWHM of the resonance. Third, the size distribution of the nanocubes chiefly determine the FWHM of the absorption resonance. Ideally to achieve perfect absorption, the fill-fraction would be tuned to perfectly match the impedance of free space, and the nanocube percentage would be

100% with a monodisperse size distribution. These parameters often vary as depicted in Table 1 resulting in worse absorption performance. With the nanocube solutions used here, the percentage of nanocubes to other particles can reach up to 91 percent in the best case. The fill-fractions of the metasurfaces vary between 16.1% and 17.7% in this paper. On the multispectral pixel sample, one problematic pixel (1125 nm resonance) showed significant aggregation of nanocubes resulting in 61% of the particles being single nanocubes and a fill-fraction of 9.4%. Thus, the poor absorption performance of this metasurface pixel can be attributed to the aggregation of the nanocubes. Table 1 lists the different metasurface parameters extracted for each different cube size from the SEM images shown in Figure 12.

Table 1: Metasurface Characteristics for Different Nanocube Sizes. Table from Wiley Publishing GmbH.[112]

SEM Nanocube Size	Nanocube Percentage	Nanocube Area Fill-Fraction	FWHM
59±5	84%	17.1%	105 nm
96±6	88%	16.1%	91 nm
146±8	79%	16.2%	200 nm

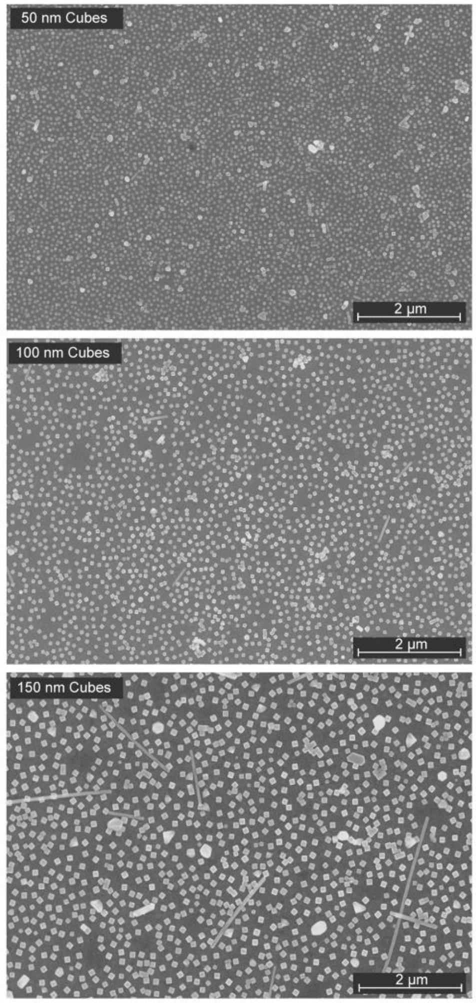

Figure 12: SEM Characterization of Metasurfaces. SEM images of the three different size nanocubes used for the metasurfaces are shown here. Most particles are nanocubes, with a small minority being nanorods, nanocube aggregates, or other geometries. Figure from Wiley Publishing GmbH.[112]

This work demonstrated the creation of a large-scale multispectral metasurface pixel array and the reconstruction of a detailed macroscopic image using a hybrid top-down, bottom-up fabrication approach. The resonance of the film-coupled resonators could be extended beyond the near infrared by utilizing colloidal nanocubes larger than

150 nm[118] or other large faceted nanoparticles. The patterning resolution could be significantly improved through the use of deep-UV lithography[119] promising for diffraction-limited plasmonic structures.

4.2 Metasurfaces for Control of Nanoscale Heat Generation from UV to SWIR

Bottom up synthesis approaches are capable of growing large quantities of metallic nanoparticles with planar facets and monodisperse sizes, but necessitate a crystalline growth process that can limit the size and material selection.[65] No current metasurface platform has been capable of producing strongly absorbing filters that span the UV to SWIR over large-areas, while allowing for the spatial losses, heat, or hot-electron generation to be fully designed for a chosen application. Here I demonstrate a new metasurface architecture which has realized absorbing metasurfaces ranging from 330-2740 nm over wafer-scale areas through the utilization of colloidal nanoparticles (NPs) of various shape, size, crystallinity, and composition. Due to the stochastic self-assembly process of the colloidal deposition, the metasurfaces are comprised of randomly oriented plasmonic nanocavities. In this work, the plasmon resonance is passively controlled by varying the size, material, and geometry of the nanostructures. In order to fabricate the plasmonic resonators with variously shaped nanoparticles (NPs), a new fabrication technique was developed in order to create two closely spaced metallic surfaces separated by a dielectric gap as shown in Figure 13a. This fabrication approach incorporates NPs of different shapes that arise during colloidal synthesis and creates highly absorbing metasurfaces from NPs previously uncapable of doing so.

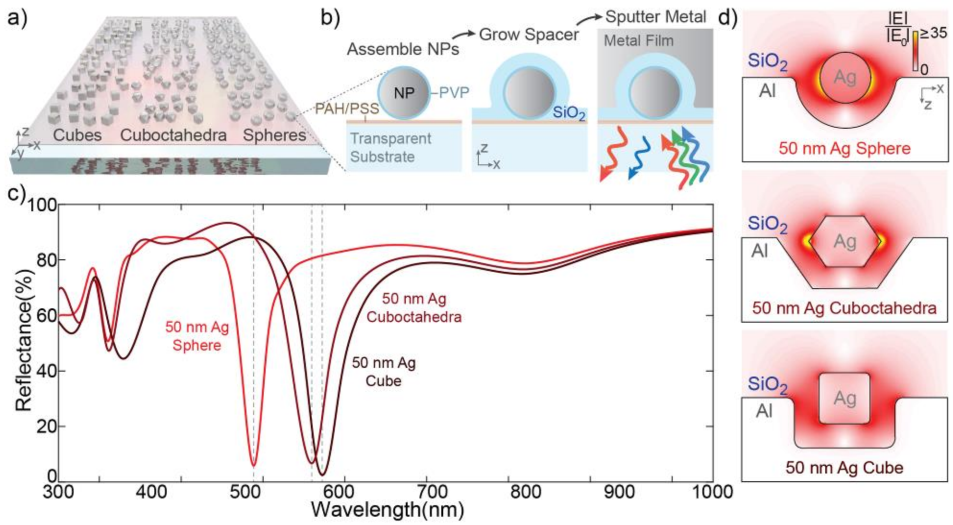

Figure 13: Embedded Metasurface Concept. a) Depiction of various colloidal nanoparticle (NP) shapes self-assembled onto a transparent substrate. b) Process of fabricating a plasmonic metasurface shown with a single metasurface unit cell. First the NPs are self-assembled onto a transparent substrate, next a dielectric spacer such as SiO2 is grown around the NPs, and lastly a metal film is sputtered around the dielectric coated NPs to form a conformal plasmonic cavity around the NP. c) Simulated reflection spectra for three metasurfaces comprised of the three NP shapes shown in (a) depicting that the wavelength of resonant absorption depends upon the geometry of the plasmonic cavity. d) Simulated electric-field enhancement for the three metasurface elements at their resonant wavelength demonstrating the plasmonic coupling between the Ag NPs and the Al film. Manuscript is currently under review.

This fabrication is initiated by conformally depositing the plasmonic NPs onto a substrate by coating the substrate in alternating PAH/PSS (cationic/anionic) polymer layers. The top cationic layer polymer facilitates an electrostatic self-assembly of the NPs with an anionic coating from their host solution resulting in the first diagram of Figure 13b. Next, a dielectric coating is grown around the nanoparticles with plasma-enhanced chemical vapor deposition (PECVD) and a metal film is physically sputtered around the dielectric-coated NP. By using a transparent substrate within the desired wavelength range, the light incident through the substrate will excite the plasmonic resonances between the NP and sputtered metal films as shown in the last panel of Figure 13b. Finite-element simulations were used to model the optical response of three different geometries with 50 nm NPs, a 24 nm SiO_2 spacer, and a 150 nm Al film. The simulated reflectance spectra in Figure 13c show peak absorptivity at the fundamental plasmon resonance occurs at 575 nm for the cubic NPs, 560 nm for the cuboctahedra NPs, and 490 nm for the spherical NPs as indicated by the grey dashed lines. The electric field enhancement at the fundamental plasmon resonance for each of these geometries is included in Figure 13d. The electric field enhancement shows that most of the electric field is contained in and near the surfaces of the NP. This plasmon oscillation confined to the NP is coupled to an oscillation of opposite phase in the sputtered metal film. This coupled mode between the NP and film reduces or cancels the electric field in the far-field preventing re-radiation of the incident energy, which results in the significant absorption of metasurfaces comprised of these elements.

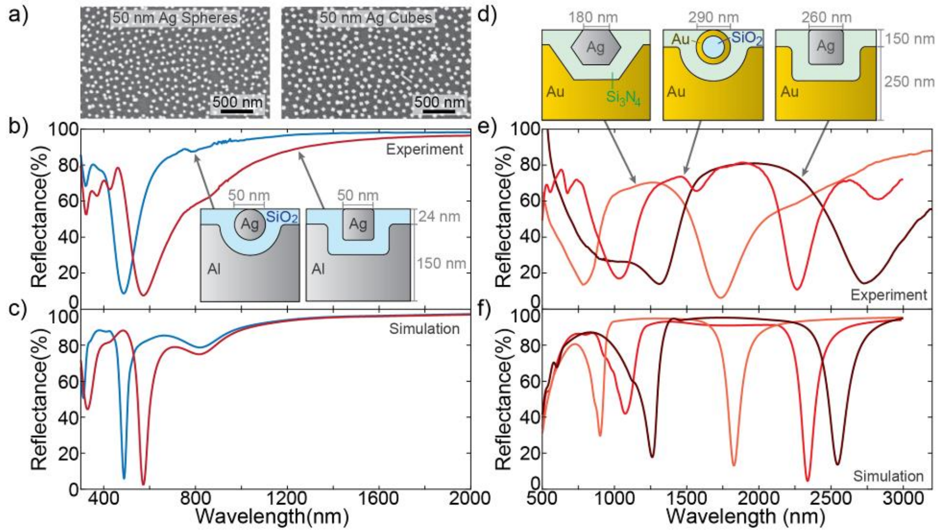

Figure 14: Fabricated Embedded Metasurfaces from UV to SWIR. a) SEM images of 50 nm Ag spheres and cubes assembled onto a coverslip before growth of the SiO2 spacer. b) Experimental reflectance spectra for metasurfaces from the 50 nm Ag spheres and cubes shown in part (a) along with labeled metasurface cross-sections. c) Simulated spectra for the metasurfaces created with 50 nm Ag spheres and cubes. d) Three SWIR metasurface cross-sections comprised of a 180 nm Au cuboctahedron, a 50 nm Au shell around a 200 nm silica core, and a 250 nm Ag cube. e) Experimental reflectance spectra for these metasurfaces showing fundamental resonances in the SWIR and a second order resonances in the near-IR. f) Simulated spectra of the three SWIR metasurfaces closely following the spectral features of the experimental results. Manuscript is currently under review.

Experimentally, the metasurfaces were realized following the procedure laid out in Figure 13b where a more detailed fabrication process is described in the experimental section. First, the NP shape dependence was tested experimentally with 45 ± 4 nm Ag spheres and 48 ± 5 nm Ag cubes, where the size distributions are calculated from SEM images. These NPs were self-assembled onto coverslips, and an SEM image of both NPs assembled onto a coverslip is shown in Figure 14a. Next, a SiO_2 spacer layer was grown around the NPs, where the optimal absorption was achieved with a thickness of 30 nm or ~60 percent of the NP size. Lastly, a 150 nm thick Al film was sputtered and the reflection spectra were measured through the coverslip. Reflection spectra of the samples were collected with a Shimadzu UV-3600 commercial spectrometer at normal incidence and were integrated over an area with a 5 mm diameter. The reflection spectra from the 50 nm Ag sphere and cube metasurfaces are shown in Figure 14b along with a dimensionally-labeled diagram. The Ag sphere metasurface has a peak absorption at 485 nm and possesses a 115 nm full width at half maximum (FWHM), and the Ag cube metasurface possesses a peak absorption at 575 nm with a 195 nm FWHM. Finite-element simulations were used to estimate the reflection spectra of these metasurfaces in Figure 14c, and the optimal SiO_2 thickness from simulations was found to be ~48 percent of the NP size in contrast with the ~60 percent found experimentally. When compared with the simulations, the experimental results possess increased FWHMs due to the non-uniform size distribution of the colloidal NP solutions and a small number of NPs aggregating during deposition. The polycrystalline 50 nm Ag spheres and have an ±8.9 percent size deviation and 90 percent of the NPs were un-aggregated spheres after self-assembly as determined from SEM images. The colloidal 50 nm Ag cubes possess a ±10.4 percent size deviation where 91 percent of the NPs were un-aggregated cubes after deposition. The FWHMs can be improved through filtering the NP solutions for tighter size distributions. However, this metasurface platform is capable of producing highly-absorbing metasurfaces with colloidal NPs of varied shape and crystallinity with commercially provided NP solutions. To further establish the spectral flexibility of these metasurface, larger colloidal NPs were developed and synthesized with Nanocomposix Inc. to realize resonances out into the SWIR. Figure 14d shows three such metasurfaces with 180 nm Ag cuboctahedra, 45 nm Au shells around a 200 nm silica core, and 260 nm Ag cubes. The three metasurfaces consist of 108, 170, and 150 nm Si_3N_4 spacers with a 250 nm sputtered Au film, where their experimental reflection spectra are shown in Figure 14e. Each spectra shows a primary absorption peak in the SWIR at 1740, 2260, and 2740 nm corresponding to the fundamental plasmonic mode of the cuboctahedra, shell, and cube, where secondary absorption peaks exist in the near-IR at 780, 1030, and 1320 nm respectively. Simulated reflection spectra from Figure 14f show fundamental modes at 1830, 2350, and 2540 nm with secondary modes at 900, 1080, and 1260 nm, which closely follow the experimental modes. Experimentally, the 290 nm Au shells show the narrowest FWHM of 260 nm due to the smaller 2.7 percent size distribution of the 288 nm shell NPs when compared to the 6.6 and 6.5 percent distribution of the 180 nm cuboctahedra and the 260 nm cubes. These results demonstrate that this versatile fabrication approach is clearly capable of achieving strongly absorbing surfaces from varying NP shapes, crystallinities, and materials while covering wavelengths from the visible to SWIR.

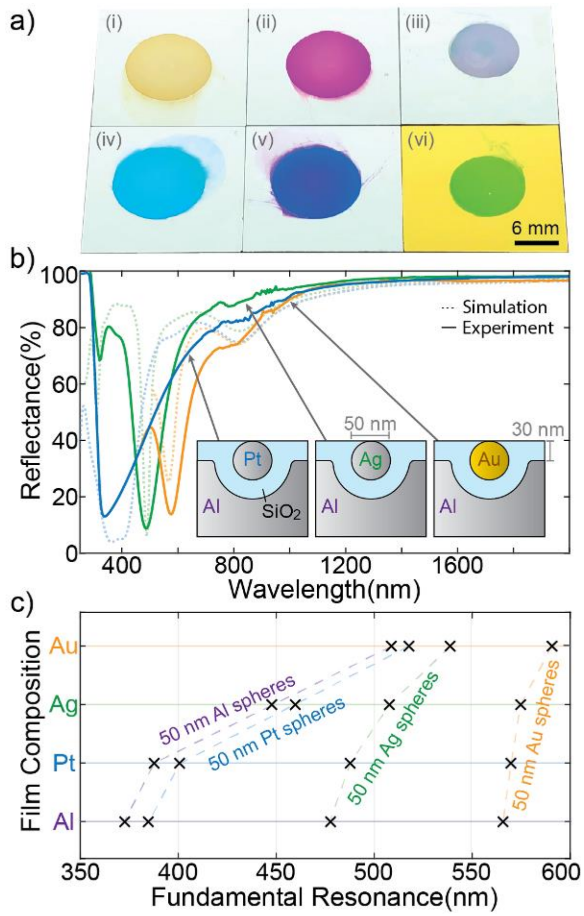

Figure 15: Varied Composition of Embedded Nanospheres. a) Image of reflected light from select metasurfaces with resonances in the visible and UV, where each metasurface is realized with 50 nm NPs, a 30 nm SiO2 layer, and a 150 nm Al film unless otherwise noted. The metasurfaces are as follows: (i) Pt sphere (ii) Ag sphere (iii) Au sphere (iv) Ag cube with 20 nm SiO2 (v) Ag cube and (vi) Au sphere with an Au film. b) Experimental and simulated spectra for metasurfaces comprised of 50 nm spheres of various compositions along with their corresponding diagrams. c) Depiction of various fundamental resonances achievable for various 50 nm NP and Film compositions as computed from simulations. Manuscript is currently under review.

To further demonstrate the versatility of this approach, various metasurfaces were fabricated with resonances in the visible and UV regimes through utilization of smaller NPs and various plasmonic materials. These metasurfaces are comprised of 50 nm cubic or spherical NPs and plasmonic materials ranging between Al, Pt, Ag, and Au. Images of select metasurfaces were captured to show the large-area uniformity and color of these metasurfaces, which is shown in Figure 15a. For example, the top three metasurfaces (i)-(iii) are 50 nm spherical NPs with a 30 nm SiO_2 layer, and a 150 nm Al film where the NP material is (i) Pt, (ii) Ag, and (iii) Au. The reflectance spectra for these three metasurfaces are shown in Figure 15b along with their simulated spectra and a labeled diagram. The Pt metasurface shows a peak absorption at 330 nm, the Ag metasurface at 490 nm, and the Au metasurface at 575 nm. The peak absorptions for all possible combinations of Al, Pt, Ag, and Au films and 50 nm spherical NPs are plotted in Figure 15c, which were obtained by finite-element simulations. With a fixed geometry, variation of the constituent metasurface materials allows for a range of resonant wavelengths to be achieved. As such, use of NPs with different materials, sizes, and shapes has allowed for the absorption spectra to be passively tuned across the ultraviolet to SWIR with a single fabrication approach.

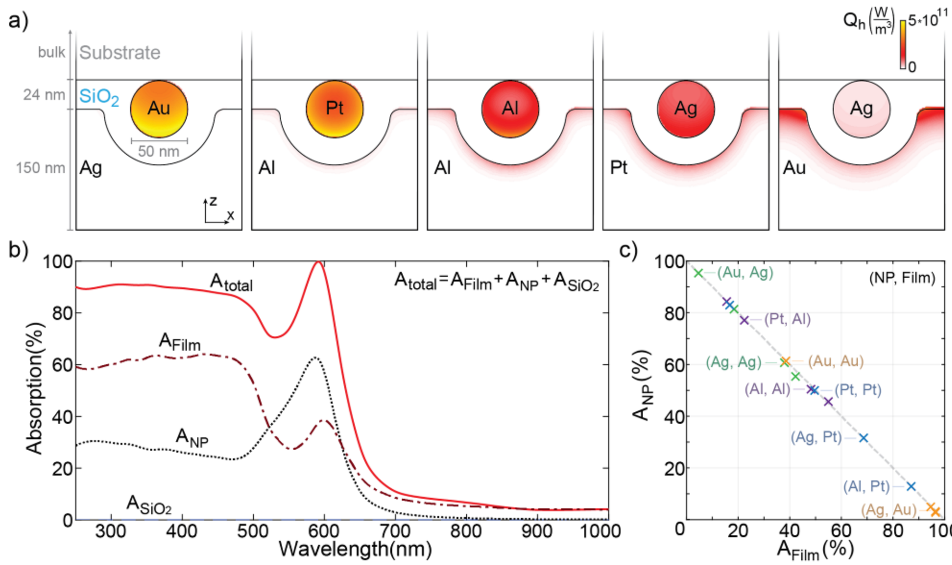

Figure 16: Nanoscale Spatial Heat Control with Embedded Metasurfaces. a) Simulated absorbed power density of metasurface unit cells comprised of 50 nm spheres embedded in films with varied compositions. The losses can thus be engineered to occur in either the NP or film through alteration of their composition. b) Simulated absorption spectra of a 50 nm Au sphere with an Au film along with the absorption spectra localized in each constituent material of the metasurface calculated according to Equation 19. c) Absorption percentage occurring in the NP and the Film for metasurfaces comprised of 50 nm spheres, where the dashed line indicates 100 percent total absorption. This demonstrates that with only four plasmonic materials the fractional losses between the NP and the film can be nearly engineered over the full parameter space. Manuscript is currently under review.

Beyond the wavelength flexibility of these large-area metasurfaces, the versatility of material choice allows for the nanoscale losses and subsequent heat generation to be spatially engineered. At the fundamental plasmonic mode, the incident electromagnetic energy is converted into localized surface plasmons confined to the metasurface resonators. These localized plasmons decay at femtosecond timescales and generate heat due to electron-phonon scattering on the picosecond timescales[74,114,120,121]. The power loss density in this system in units of W/m^3 can be estimated classically via resistive/ohmic losses due to the collective movement of charges (i.e. plasmon) in a lossy conductor[120]. The power loss density for the metasurface element, Q_h, is calculated from Equation 19 shown below.

$$Q_h\left(\vec{r},\lambda\right)=\frac{c}{2\lambda}\varepsilon''\left(\lambda\right)\left|\vec{E}\left(\vec{r},\lambda\right)\right|^2 \tag{19}$$

Where **r** is spatial location in the metasurface unit cell, c is the speed of light, λ is the wavelength, ε'' is the imaginary component of the permittivity, and $\mathbf{E}(\mathbf{r},\lambda)$ is the electric field vector. Intentional choices for the NP geometry and material composition allow for control over the spatial electric field distribution. With design of this spatial electric field distribution and its relative placement in high-loss or low-loss materials, i.e. materials with high or low imaginary permittivities, the power loss density can be spatially engineered. For example, the spatial losses and subsequent heat generation can be controlled for a fixed geometrical design through material choice, as seen in Figure 16a with 50 nm spheres of various compositions. The power loss density, Q_h, is shown for five representative metasurface elements, where the spatial losses can be tuned between the 96 percent occurring in the NP with the Au NP/Ag film geometry and 96 percent occurring in the film with the Ag NP/Au film. The fractional absorption occurring within a specific region, denoted as $A_{region}(\lambda)$, can be calculated from Equation 20 below.

$$A_{region}\left(\lambda\right)=\frac{1}{A_{total}\left(\lambda\right)}\iiint_{region}Q_h\left(\vec{r},\lambda\right)d\vec{r} \tag{20}$$

Where is the total absorption of the metasurface element, where the power loss density is integrated over the volume of the desired region, such as the NP, spacer, or film. Figure 16b demonstrates the fractional spectral absorption for an Au NP/Au film calculated with Equation 20, where the fractional absorption for the film, NP, and spacer are shown. For wavelengths shorter than 500 nm, the interband transition of Au governs the large absorptions occurring in both the film and NP[114]. Past interband transitions, the fundamental plasmonic resonance dominates at 590 nm, showing a significantly enhanced absorption in the Au NP due to the electric field confinement in and around the NP. At the peak absorption of 99.8 percent, over 62 percent is absorbed in the Au NP and 38 percent in the Au film. Figure 4c shows the absorption percentages occurring in the NP and film for simulated metasurfaces at their resonance wavelength. All the simulated metasurfaces have the same geometry with a 24 nm SiO_2 spacer, but the NP and film material is varied between Au, Ag, Al, and Pt. The highest fraction of power absorbed in the NP occurs with an Au NP and an Ag film, showing 96 percent of all absorption occurring in the NP on resonance. The lowest fraction of power absorbed in the NP occurs with an Ag NP and an Au film, where 4 percent of all absorption occurs in the NP at its' resonance as shown in Figure 16c. These two cases are shown pictorially in Figure 16a on the far left and far right images, where most of the absorption is either happening in the NP or film. By utilizing other material combinations, the relative absorption and subsequent heat generation in the metasurface can be spatially engineered for resonances spanning the UV to SWIR.

The finite-element simulations were conducted in COMSOL Multiphysics utilizing the Wave Optics module for the absorptive characteristics and calculating the power loss density. The electromagnetic (EM) simulation was conducted in the frequency domain with the boundary conditions laid out in Figure 17, where periodic boundary conditions and perfectly match layers are used to simulate an infinitely periodic array of the plasmonic resonators. The electric field enhancement and spatial loss density were calculated with the frequency domain simulation results.

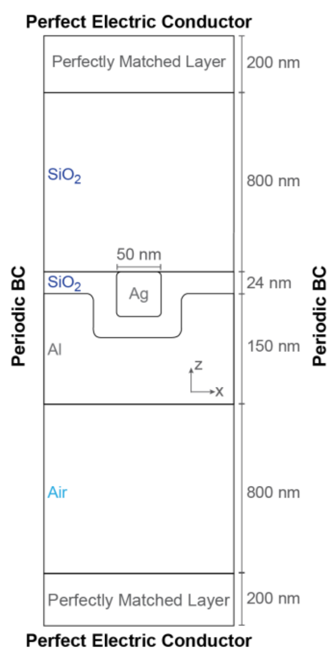

Figure 17: Finite-Element Simulation Schematic. An illustration of the simulated geometry for a 50 nm Ag cube with a 24 nm SiO2 spacer and a 150 nm Al film. Periodic boundary conditions were used on the x-z and y-z faces while a perfectly matched layer was used to cap the top and bottom x-y faces to prevent reflections from the simulation boundaries. Manuscript is currently under review.

To expose the face of the metasurface for applications such as photocatalysis, the fabrication approach can be altered to allow for the metasurfaces to be template-stripped from the substrate. First, a smooth substrate with a weak adhesion to the selected dielectric spacer is needed. In this case a p-type Si wafer is cleaned and prepared. Initially, an adhesion layer is deposited according to the experimental section with alternating PE layers. Following the nanoparticle deposition, PE layers are utilized again to conformally coat the NPs forming the dielectric spacer that will separate the metallic NP from the metal film. After deposition of the dielectric layer, the NP/dielectric structure was surrounded in an Au film of 150 nm thickness via sputtering. To expose the metasurface from the substrate, the metasurface is bonded to a new substrate and heated to 150˚C to cure the epoxy bonding agent. The metasurfaces were then template stripped off the silicon wafer exposing the metasurface. Here the template-stripping approach is demonstrated with three different sizes of Ag cubes (Figure 18) and Au spheres (Figure 19) at three different spacer thicknesses. The exposed metasurface allows for the SEM images to directly image the final metasurface produced from this fabrication approach. The reflection spectra in Figure 18b and Figure 19b were integrated over an area with a 5 mm diameter on a Shimadzu UV-3600 at normal reflectance.

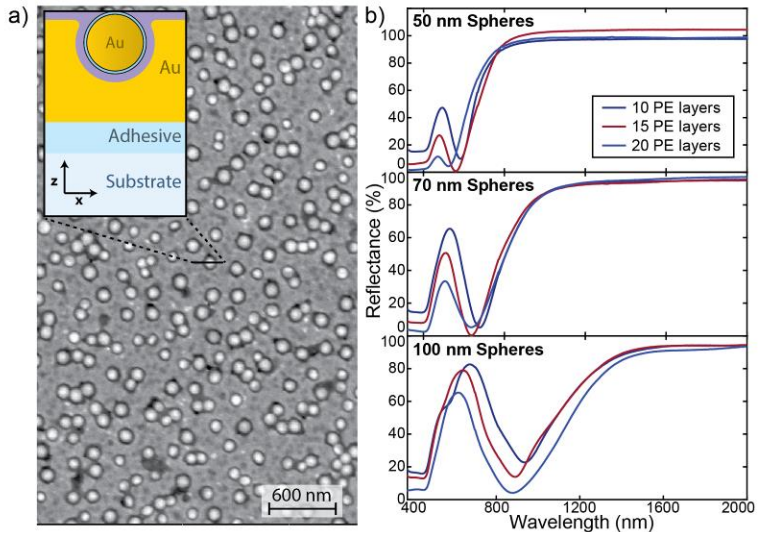

Figure 18: Template-Stripped Embedded Nanospheres. a) SEM image of 140 nm Ag cubes with a 10 PE layer spacer layer overlaid with the metasurface cross section. b) Reflection spectra of three Ag cube sizes with three different spacer layers after template-stripping from Si substrate. Manuscript is currently under review.

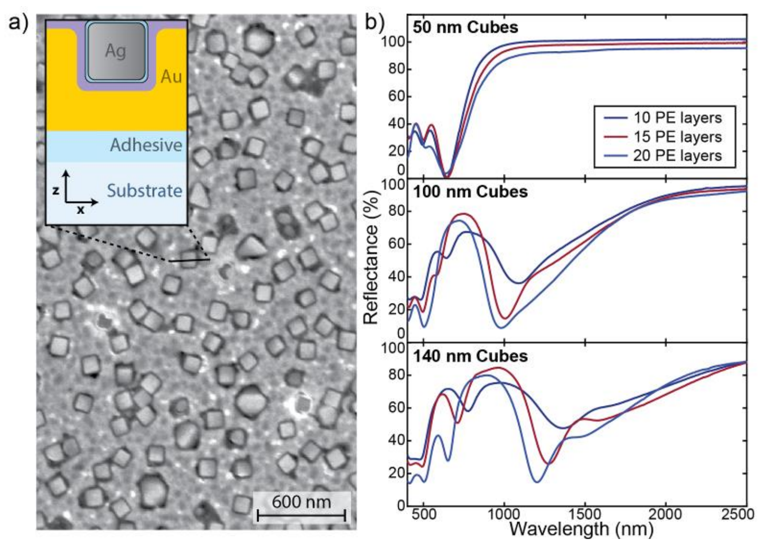

Figure 19: Template-Stripped Embedded Nanocubes. a) SEM image of 100 nm Au sphere with a 10 PE layer spacer layer overlaid with the metasurface cross section. b) Reflection spectra of three Au sphere sizes with three different spacer layers after template-stripping from Si substrate. Manuscript is currently under review.

The presented metasurface architecture leverages the strengths of colloidal synthesis, self-assembly, and large-area deposition processes to demonstrate nanometer to millimeter scale control of absorption processes from 330-2740 nm. Furthermore, the absorbing metasurfaces have spectral, environmental, and geometrical characteristics promising for filling a spectral niche for optical metasurfaces with feature sizes below the resolution of standard I-line photolithographic systems. The influence of NP shape and material composition were analyzed both experimentally and with finite-element simulations to show the flexibility of this method with various crystallinities, materials, shapes, and sizes. This flexibility provides this platform with a unique capability for complete design of the spatial losses and heat generation at the nanoscale for a variety of hot electron or photothermal processes. For instance, integration of a thermally-sensitive film, such as a pyroelectric material, into the gap of the plasmonic nanocavity would allow for an optical-thermal-electrical conversion device for creation of photodetectors[31,63,122] sensitive from UV to SWIR. Incorporation of actively tunable materials into these metasurfaces would allow for dynamic control of their reflection spectra[106,123–126] for spectrally-tunable photodetectors or beam-steering surfaces.

4.3 Dynamically Tunable Metasurfaces

A dynamically tunable metasurfaces are a key development for increasing the spectral resolution of a spectrally selective thermal detector. For a standard multispectral focal plane array with fixed absorption resonances, the spectral regions will have to be designed around regions of interest in the target scene. However, if a dynamically tunable absorber was utilized with a multispectral FPA, the FPA could capture more spectral information in a manner similar to hyperspectral imagers, lending the FPA more versatility and accuracy for material characterization.

Plasmonic nanostructures provide an ideal platform for realizing dynamically tunable materials due to their inherent sensitivity to the surrounding dielectric materials. Incorporating active materials with plasmonic nanostructures promises to provide novel materials with dynamically controllable optical properties. Active metasurfaces have been demonstrated using a wide array of tuning mechanisms, including electrical modulation,[123,124,127–130] polarization of incident light,[109] mechanical strain,[131,132] hydrogen gas flow,[133,134] UV exposure,[126,135] femtosecond laser pulses[136,137] and heating.[138–143] While there have been several demonstrations of robust tuning at mid-IR and longer wavelengths,[127,130,143] active metasurfaces in the visible and near-IR have generally been limited by tuning mechanisms that are ill-suited for practical devices, for reasons such as lack of reversibility or degradation of switching over multiple cycles.[123,126,131,144]

4.3.1 Photochromic Materials

One promising approach for a dynamically tunable material is that of photochromic polymers such as spiropyran.[145–148] Here I demonstrate reversible photoisomerization of photochromic molecules integrated into plasmonic nanopatch antennas consisting of film-coupled silver nanocubes. The plasmonic resonance of individual nanoantennas was reversibly tuned up to 71 nm in the visible regime by exposing the photochromic molecules in the nanocavity with UV light to induce a photoisomerization reaction. Resetting the isomerization process was realized with white light exposure. Single particle spectroscopy measurements verified the tuning of individual nanopatch antennas before and after the photoisomerization process. The large experimental tuning as confirmed through finite-element simulations results from resonant coupling of the plasmonic resonance with the photochromic molecules after photoisomerization.

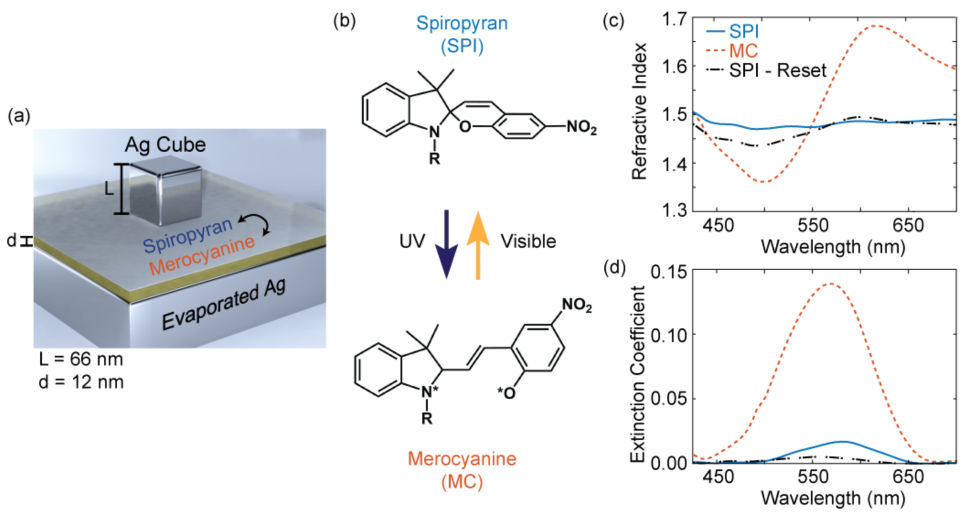

Figure 20: Photochromic Active Tuning Concept. (a) Schematic of film coupled nanopatch antenna with 66 nm nanocube and 12 nm photochromic spacer layer over a 75 nm silver film. (b) Chemical structure diagram showing two isomers of SPI that can be alternated through either UV or visible light exposure. (c-d) Refractive index and extinction coefficient of a 12 nm layer of SPI/PMMA before (blue “SPI”) and after UV exposure (red “MC”) and after being thermally reset (yellow “SPI-Reset”). Figure from ACS Publications.[126]

The plasmonic nanoantennas are comprised of silver nanocubes separated from a silver film by a composite spiropyran (SPI) and poly(methyl methacrylate) (PMMA) spacer layer as shown in Figure 20a. They act as both a small mode volume nanocavity for extreme field confinement and a nanopatch optical antenna for efficient coupling of light to localized plasmons. The fundamental resonance of this structure shown in the electric field profile of Figure 21a depends strongly on the nanocube size, gap layer thickness and the dielectric properties of the material in the gap.[64,65,149] The controllable optical properties of the SPI thin films make them ideal candidates for altering the resonance of these nanostructures. The thin films were prepared by spin coating 3:2 weight ratio solutions of SPI and PMMA in anisole onto a 75 nm template-stripped silver film. A sub-nanometer layer of cationic poly(allylamine hydrochloride) (PAH) was self-assembled onto the SPI-PMMA thin film to facilitate better adhesion of the anionic poly(vinyl pyrrolidone) (PVP) coated silver nanocubes. The colloidal silver nanocubes were then drop-casted and electrostatically adhered to the PAH polymer layer using a dilute solution of nanocubes to ensure that only a single nanoantenna is contained within a diffraction limited spot. A more detailed fabrication procedure is described in the Sample Fabrication section of the Supporting Information. Figure 20b shows the chemical structure of the photochromic isomers before and after UV exposure and depicts the C-O ring opening reaction that induces the change in optical properties. The photoisomerization to merocyanine (MC) can be reversed through visible light or thermal exposure and the switching process can be repeated.[150,151] The optical characteristics of 12 nm thick SPI-PMMA films were probed using variable angle spectroscopic ellipsometry. The optical parameters were extracted from fitting the ellipsometry data to a Lorentzian oscillator model and the results are consistent with previously reported data.[145–147,150–153] Figure 20c-d shows the refractive index and extinction coefficient before and after the photoisomerization reactions. The data clearly shows a significant change in the refractive index centered around 550 nm coinciding with a large increase in the extinction coefficient with a peak at 560 nm. Ellipsometry measurements allowed for the characterization of damage and switching thresholds prior to integration with the plasmonic structure. The switching threshold for the 3:2 SPI-PMMA thin films was found to be a 4 minute exposure using a 340 nm light emitting diode (LED) at a ~1 mW/cm^2 power density.

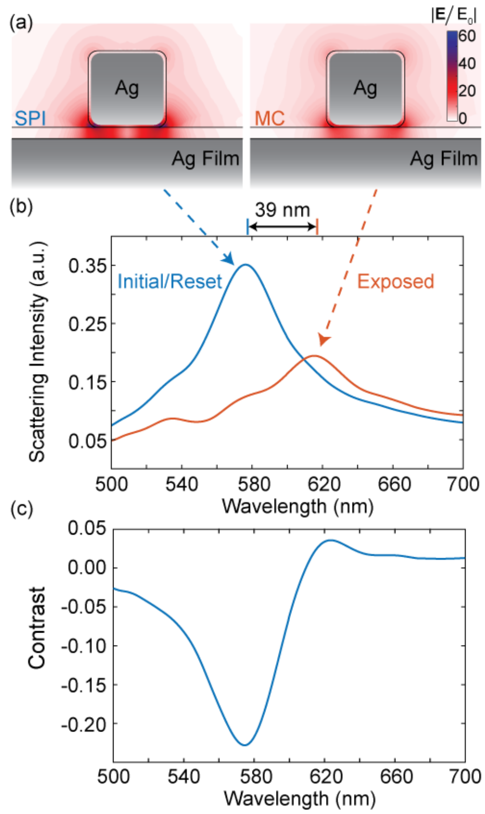

Figure 21: Active Tuning of Single Plasmonic Nanocavity. (a) Simulated electric field enhancement for nanoantennas with SPI and MC in the gap region shown at the fundamental resonance (565 nm and 610 nm, respectively). (b) Representative nanoantenna dark-field scattering spectra taken before and after UV exposure. (c) Contrast between scattering spectra taken before and after UV exposure. Figure from ACS Publications.[126]

As depicted in Figure 21, the fundamental resonance of the plasmonic nanoantenna can be tuned by incorporating the photochromic thin film into the gap region and exposure to UV light to induce the photoisomerization process. Figure 21a shows the simulated electric field enhancement of the fundamental plasmonic mode before and after photoisomerization for a nanoantenna composed of a 75 nm silver film, a 10 nm SPI-PMMA film and a 66 nm cube with a 3 nm PVP coating. The field enhancements are calculated by dividing the magnitude of the electric field vector, denoted as **E**, by the incident field magnitude, E_0, used to excite the resonance. The simulations demonstrate the effect of the SPI and MC isomers on the fundamental plasmonic mode, where the maximum field enhancement reached 60 times for the SPI case and 38 times for the MC case. The smaller simulated field enhancements for the MC simulations arise from the increased extinction coefficient of MC evident in Figure 20d, which introduces higher losses into the system resulting in a weaker plasmonic resonance. Experimentally, single particle spectroscopy measurements were taken of the plasmonic nanoantennas before and after UV exposure using a custom-built microscope depicted in Figure S1 of the Supporting Information. The UV LED was integrated into the microscope with a power density between 0.99-1.07 mW/cm^2 and a 10.6 μm diameter excitation spot size. Each nanoantenna was identified using an EM-CCD camera with bandpass filters around the resonance of the nanostructures. Once identified, a white light scattering spectrum was taken by integrating over an area with a 3 μm diameter on the sample. Next, the nanoantennas were irradiated with UV light for 10 minutes to ensure full conversion of the SPI molecules to MC, and another white light scattering spectrum was taken to compare to the initial scattering resonance. After blocking the UV light, another spectrum was taken after 10 minutes of exposure to white light to verify the reversibility of the switching process. Figure 21b shows the experimental data from exposing a representative single nanoantenna with a resonance initially centered at 577 nm. The nanoantenna was composed of a 75 nm silver film, a 12 nm PMMA/SPI spacer, a sub-nanometer polymer adhesion layer, and a silver nanocube with a 66nm nominal side length. After UV exposure, the resonance of the nanoantenna was spectrally shifted by 39 nm which corresponds to 0.75 times the full width at half maximum (FWHM) of the initial resonance often denoted as the tuning figure of merit (FOM – spectral shift divided by the FWHM of the initial spectrum). The decreased scattering intensity between the initial resonance and switched resonance is due to resonant coupling of the plasmonic resonator to the MC isomer which introduces losses to the system. Figure 21c shows the contrast between the initial and switched nanoantenna states defined as the difference between their scattering intensities. At the initial resonance wavelength the contrast is 65 percent, while at the switched resonance the contrast is 13 percent. The simulations and experimental data in Figure 21b-c both depict that the photoisomerization reaction shifts and damps the fundamental mode of the plasmonic nanoantennas.

To elucidate the mechanisms underlying the large peak wavelength shifts and investigate the effect of resonant coupling between the nanoantennas and MC, the resonance wavelength of the nanoantennas was varied. For this investigation, nanoantennas with a fundamental resonance between 550 and 720 nm were fabricated by altering the thickness of the SPI-PMMA film from 2 to 25 nm and through the inherent size distribution of the 66 ± 5 nm silver nanocubes. Through this, the dependence between the tuning range and the gap thickness of the nanoantenna is investigated while keeping the nanocube size fixed within 7.5 percent.

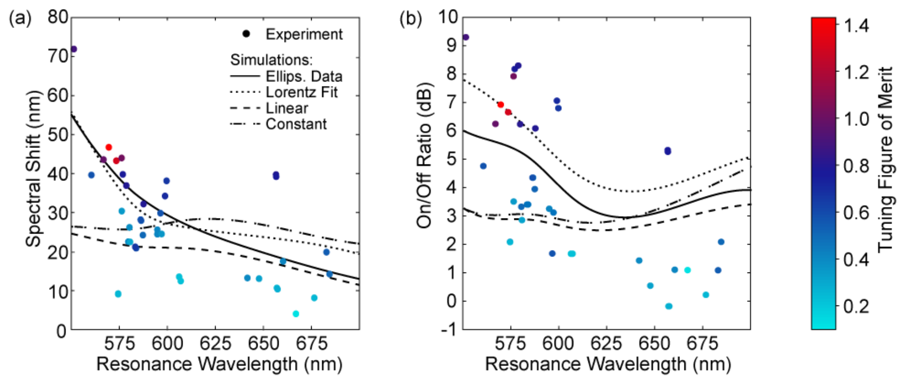

Figure 22: Spectral Dependence of Nanocavity Tuning. (a) Experimental and simulated change in the peak scattering wavelength for nanoantennas with different resonance wavelengths. (b) Experimental and simulated on/off ratio for nanoantennas with different resonance wavelengths. The colors of the data points indicate the tuning figure of merit (spectral shift divided by the FWHM of the initial resonance). The simulation labels denote different dispersion models for the refractive index of MC. The dispersion in refractive index and extinction coefficient used for the "Ellips. Data" simulation was taken from ellipsometry measurements on a thin SPI(MC)-PMMA film. The "Lorentz Fit" simulation used an ideal Lorentzian oscillator fit of the ellipsometry data. The "Linear" and "Constant" simulations used linear dispersion and a dc shift in the refractive index respectively, with no extinction. Figure from ACS Publications.[126]

Switching data was taken for 41 individual nanoantennas across the visible spectrum. Figure 22a depicts the analyzed experimental data where each point corresponds to a single plasmonic nanoantenna plotted according to its resonance wavelength and amount of spectral shift. The color of each data point indicates the FOM for the nanoantenna calculated from the linewidth of the initial resonance. The FOM was selected as a representation of the quality of tuning due to its isolation of the spectral switching properties from the absolute scattering intensity. Figure 22a shows that as the resonance wavelength is blue-shifted towards 550 nm the spectral shift increases. Furthermore, the FOM is the highest for nanoantennas with a 12 nm film thickness and resonance wavelengths near 570 nm. Thicknesses beyond 25 nm result in nanoantennas that are poorly coupled to the metallic substrate and cannot blue shift the resonance beyond 550 nm. Figure 22b shows the scattering on/off ratio at the initial resonance for the same nanoantennas shown in Figure 22a and similarly depicts the FOM with their respective color. Similar to the spectral shift, the on/off ratio exhibits increased performance for blue-shifted resonances. It is important to note that if the scattering intensity and FWHM do not change upon switching, the on/off ratio will be directly related to the FOM. However, since the scattering FWHM and the intensity do change upon photoisomerization as shown in Figure 21b, the nanoantennas with the highest FOM do not necessarily have the highest on/off ratios. The largest spectral shift and on/off ratio occurs for the nanoantenna with its initial resonance centered at 550 nm, which exhibits 71 nm of spectral shift and 9.2 dB of selectivity. On average the highest on/off ratios, FOMs, and spectral shifts arise from nanoantennas with initial resonances centered between 550-580 nm coinciding with the molecular transition of the MC isomer. To the first order when the index of refraction in a plasmonic gap changes, there is a corresponding change in the plasmon resonance. From this, it would be expected that the largest spectral shifts and on/off ratios would be observed when the nanoantenna resonance overlaps with the largest refractive index change between the SPI and MC isomers at 615 nm. However, the largest spectral shifts and on/off ratios observed experimentally occur around the minimal change in the index of refraction near 550 nm, suggesting that a more complex phenomenon is responsible for the large spectral shifts.

For further insight into the mechanisms underlying the large experimental tuning, finite-difference frequency domain (FDFD) finite-element scattering simulations were conducted utilizing varying dispersion models for the refractive index of MC. The simulation results are overlaid with the experimental data in Figure 22a-b where the solid and dashed black lines correspond to the scattering simulations for 66 nm nanocubes with 2-12 nm spacer thicknesses and are labeled according to the dispersion profile used for the MC-PMMA refractive indices. The different dispersion profiles are plotted in Figure S1 of the Supporting Information along with the simulation results. The constant dispersion profile uses the largest index change at 615 nm in the ellipsometry data and models the photoisomerization reaction as a constant index change from 1.49 to 1.68 over the entire wavelength range. The linear dispersion profile is similar but accounts for the negative dispersion of the MC not included in the constant dispersion case. Simulations utilizing the ellipsometry data from Figure 20c-d for the refractive index of the spacer layer agrees well with the observed experimental spectral shifts and on/off ratios. Fitting the ellipsometry data with a Lorentzian oscillator dispersion model similarly results in good agreement with the experimental data. The Lorentzian dispersion model was chosen to enable investigation of the macroscopic effects of dipolar coupling of the MC molecules to the plasmonic mode. The Lorentzian dispersion model is a homogenized material response derived from assuming the material is comprised of many dipoles within a subwavelength volume, which as seen in Figure 22a-b is a good approximation for the dense MC-PMMA photochromic films used in this work. Comparing the simulation results using these four dispersion profiles it is further evident that the nanoantenna tuning does not directly result from a change in refractive index in the gap region.

As shown in Figure 22a, the linear and constant dispersion models consistently underestimate the amount of spectral shift at wavelengths near the transition of MC. The overlay of the simulations with experimental results in Figure 22a-b show that the large spectral shifts observed in this work are described better by the refractive index profiles modeled with a resonant dipolar response centered at 550 nm. The good agreement between experiment and simulations that used a Lorentzian oscillator to model a resonant dipole with respect to the spectral shift, on/off ratio, intensity change, and linewidth broadening of the plasmonic resonances leads to the conclusion that the mechanism responsible for the large tuning demonstrated here is weak-coupling between the MC isomer and the fundamental plasmonic resonance. As the plasmonic resonance and the resonance of the MC isomers are overlapped, the coupling strength increases and larger spectral shifts are observed despite minimal change in the index. Because no characteristic evidence of strong coupling is observed, such as peak splitting and anti-crossings as shown in other recent demonstrations,[145,146] the MC isomers are most likely weakly coupled to the plasmonic resonator. However, the switchable resonant coupling shown here results in larger spectral shifts and on/off ratios as compared to non-resonant changes in refractive index at the expense of increased losses.

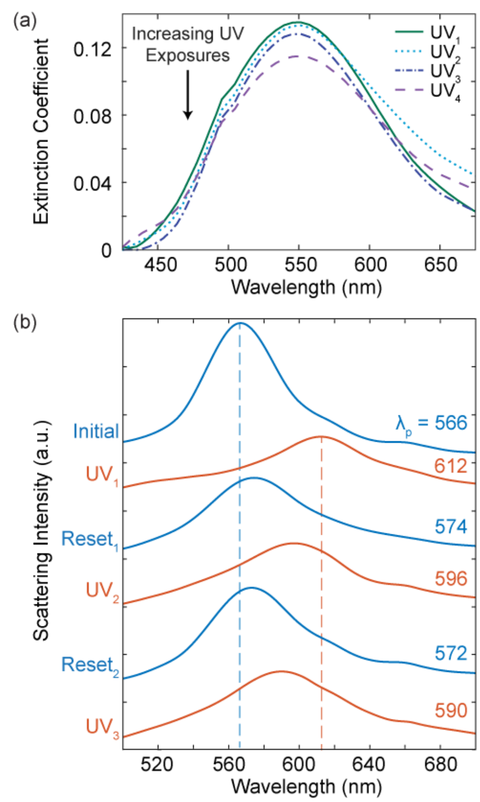

Figure 23: Multi-Cycle Tuning and Reversibility. (a) Extinction coefficient extracted from ellipsometry measurements after multiple UV exposure- reset cycles. (b) Scattering spectra from a representative nanoantenna after multiple UV exposure-white light reset cycles, where λp denotes the wavelength where peak scattering intensity occurs. Figure from ACS Publications.[126]

Beyond the tuning mechanisms, another important aspect to characterize with dynamic devices is the reversibility beyond a single switching cycle. In this work, ellipsometry was used to evaluate the performance of the SPI/MC isomerization for several switching-reset cycles. Using the same switching parameters as described earlier, Figure 23a demonstrates the extinction coefficient alteration of the MC/PMMA composite through four consecutive switching cycles, labeled respectively as UV_{1-4}. It is seen that after these four cycles the extinction coefficient decreases by 14 percent relative to the initial switch, indicating fatigue of the SPI molecules. The fatigue of SPI from UV exposure is a result of side reactions leading to modified molecular structures with a lack of photoresponsive properties.[151] It is important to note, the fatigue of SPI is minimized when embedded in PMMA as compared to other polymer host matrices.[150] The fatigue evident in the ellipsometry data is similarly seen in reduced spectral shifts of the nanoantenna after multiple cycles as shown in Figure 23b. The scattering resonance of a single nanoantenna is shown through three cycles with a 62 percent reduction in the spectral shift after the third cycle. The increased fatigue in the nanoantenna is most likely a result of the extreme environment in the nanometer-scale plasmonic cavity and due to accumulation of semi-stable but optically inert isomers of SPI. When reset thermally these states can be eliminated but using visible light to revert the MC back to SPI does not fully recover all the molecules in the time scale of 10 minutes. Other photoswitchable molecules have greater fatigue resistance but exhibit smaller changes in the optical constants upon photoisomerization.[154]

Here I have demonstrated reversible tuning of the plasmon resonance of over 40 distinct nanoantennas in the visible regime through the photoisomerization of SPI integrated between silver nanocubes and a silver film. The plasmon resonance was actively tuned over multiple cycles by up to 71 nm corresponding to a FOM of 1.43 which to the best of our knowledge is the highest reported in the visible spectrum. The scattering spectra of single nanoantennas were actively red-shifted by varying amounts depending on their initial resonance wavelength and nanoparticle size, correlating with the coupling strength between the MC isomers and the plasmonic resonance. The experimental results show good agreement with finite-element simulations, demonstrating dynamic control over plasmon resonances with an all optical approach. Furthermore, the inherent switching rate of SPI isomers to MC in solution have been shown to surpass 40 ps[155] promising for applications requiring ultrafast tuning with high on/off ratios. However, this approach requires an optical signal for switching which is not ideal for integration with a multispectral FPA.

4.3.2 Phase-Change Materials

One option for overcoming the limitations of photochromic materials is through utilizing the phase-change material vanadium dioxide (VO_2), which offers robust switching via heating above 68°C. At this temperature, VO_2 undergoes a first-order, crystalline phase transition with an accompanying change in its refractive index, which is fully reversible by cooling below the transition temperature.[156] It has also been reported that this phase change can be induced electrically with a less than 2 ns response time,[157] increasing the promise of VO_2 for integration into practical, active metasurface devices. Previously, VO_2 has been used to create active metasurfaces over a broad wavelength range[138,142,143,158–160], typically with bulk materials or sputtered films with thicknesses of 50-150 nm[161–166]. However, integrating nanometer-scale films of VO_2 with nanocavity structures has remained an outstanding challenge, yet offers the promise for robust, deeply subwavelength tunable optoelectronic devices to enable e.g. nanoscale optical memories and dynamic control of fluorophores and quantum emitters.

Here I demonstrate reversible tuning of near-IR absorption resonances from active plasmonic metasurfaces via the insulator-to-metal phase transition of a 6 nm VO_2 film grown by atomic layer deposition (ALD).

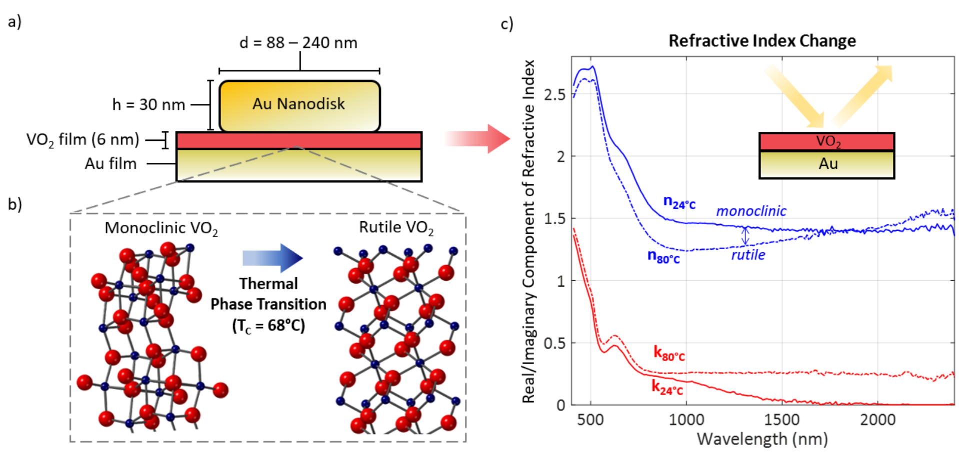

Figure 24: VO_2 Dynamic Tuning Concept. (a) Schematic of sample structure consisting of Au nanodisks (height = 30 nm) separated from an Au ground plane by 6 nm of VO2. (b) Illustration of phase transition of VO2. Upon heating to ~68°C, the crystal structure shifts from monoclinic to rutile leading to a corresponding change in its refractive index. (c) Ellipsometry-measured real and imaginary components of the refractive index of a 6 nm VO2 film on gold at room temperature and after heating to 80°C. Manuscript is under review.

The tunable metasurfaces consist of arrays of plasmonic nanodisks on top of the VO_2 and Au films, where a single nanocavity is shown in Figure 24a. The resonances are statically controlled by varying the nanoparticle diameter and dynamically controlled through the refractive index tuning of the VO_2 layer. Upon heating to ~68°C, VO_2 undergoes a phase transition which alters the corresponding crystal structure from monoclinic to rutile as depicted in Figure 24b. In the monoclinic phase, VO_2 is transparent and insulting in the IR and possesses a bandgap of 0.7 eV.[167] When transitioned to the tetragonal phase, the bandgap closes resulting in lossy metallic behavior or a metallic phase. Beyond a purely electronic transition, this insulator-to-metal transition possesses a concomitant change in the real and imaginary components of the refractive index. Figure 24c depicts the refractive index change for a 6 nm film deposited on Au and measured by ellipsometry at 24°C and 80°C for wavelengths spanning from 400-2400 nm. Spectrally, the largest refractive index change of -0.28 occurs at 720 nm for the real component and 0.25 at 2390 nm for the imaginary component. In the monoclinic phase, the VO_2 film exhibits normal dispersion for wavelengths longer than 500 nm indicative of the insulating or dielectric state. When in the tetragonal phase at 80°C, the refractive index shows anomalous dispersion at wavelengths longer than 1000 nm indicative of metallic behavior. As such, the refractive index change in Figure 24c distinctly shows the insulator-to-metal transition induced upon heating.

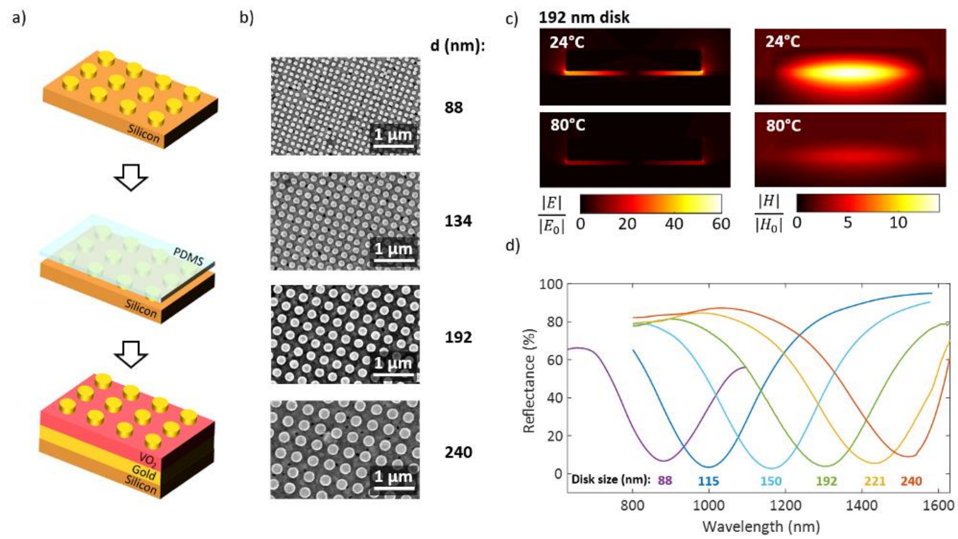

Figure 25: EBL Metasurface Transfer onto VO_2 Films. (a) Fabrication process for transferring EBL-fabricated gold nanodisks onto the VO2 film. (b) SEM images of gold nanodisks for a few of the fabricated sizes. (c) Simulated electric (left) and magnetic (right) field profiles at 24°C and 80°C for the nanogap cavity structure with 192 nm gold nanodisks. An incident plane wave with wavelength matching the room-temperature resonance of the nanocavity at 1495 nm is utilized. (d) Room-temperature reflectance spectra for metasurfaces consisting of six different sizes of nanodisks where additional spectra are shown in the SI. Manuscript is under review.

Fabrication of the structure began with growing the VO_2 on a 75-nm-thick Au film via ALD, which was then annealed to form a poly-crystalline film from the initially amorphous material and had the effect of ensuring that the metasurface switching was fully reversible. Next, the VO_2 films were embedded into plasmonic nanocavities by transferring Au nanodisks on top of them. The Au nanodisks were fabricated using electron-beam lithography (EBL) on a Si substrate. Due to the weak adhesion of Au to the Si substrate, the Au nanodisks could be exfoliated from the Si wafer after removing the native SiO_2 and deposited onto the VO_2 film using a PDMS stamp as shown in Figure 25a. This technique was utilized due to the sensitivity of VO_2 to electron-beam exposures and subsequent development processes. In all, ten metasurfaces were fabricated by varying the diameter of the nanodisks (from 88 nm to 240 nm), where SEM images of representative metasurfaces are shown in Figure 25b. The plasmonic nanocavities possess a large effective electric and magnetic response on resonance as shown in Figure 25c, which is strongly localized in the VO_2 film below the disks. As such, a sufficient fill fraction of nanocavities on the surface can result in near-perfect absorption at the plasmonic resonance, which can intuitively be thought of as the destructive interference of the reflected wave with the multitude of plasmonic modes.[67,168]

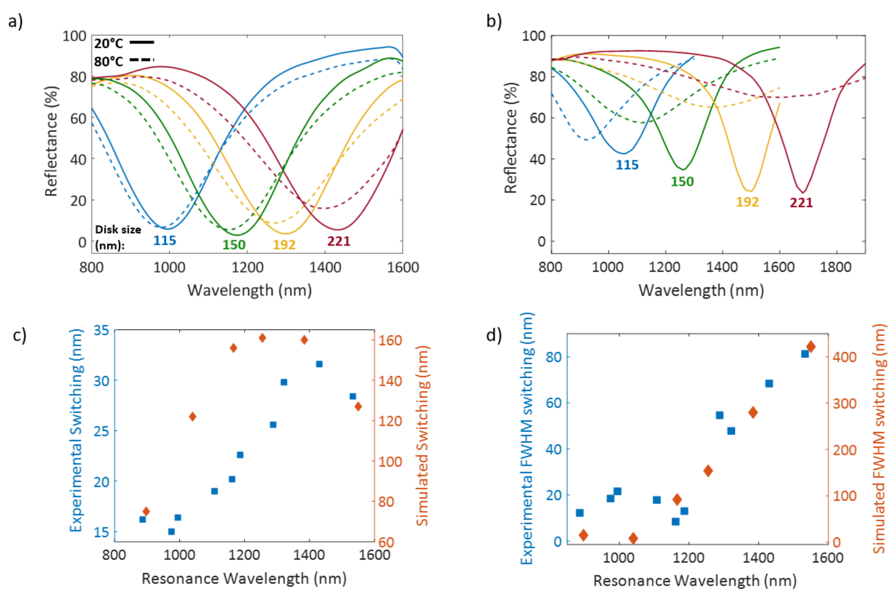

Figure 26: Spectral Dependence of VO_2 Metasurface Tuning. (a) Thermal switching spectra for metasurfaces consisting of 115, 150, 192 and 221 nm diameter Au nanodisks. Spectra for the remaining sizes are shown in the SI. (b) Simulated switching spectra for the same size nanodisks as in (a). (c) Comparison of the amount of switching predicted in simulations and measured experimentally as a function of the resonance wavelength. (d) Comparison of the amount of switching in the full-width at half-maximum (FWHM) predicted in simulations and measured experimentally as a function of the resonance wavelength. Manuscript is under review.

Due to the spectrally dependent variations in the insulator-to-metal transition, ten spectrally distinct metasurfaces were used to assess the dispersion of the active tuning. The resonant wavelengths for these absorbing metasurfaces range from ~900 nm to >1500 nm, and span above and below the anomalous dispersion of the tetragonal VO_2 phase. The room-temperature reflection spectra of the metasurfaces was measured with a white light source focused through a 0.15 NA objective as shown in Figure 25d. All the metasurfaces demonstrate near-perfect absorption of incident light on resonance, with typical peak absorption values of ~95%. The switching spectra for the 115, 150, 192 and 221 nm nanodisk metasurfaces are shown in Figure 26a. In addition to producing a spectral shift in the resonance, heating the metasurfaces was also observed to modulate the peak absorbance by as much as 12%, contributing further to the dynamic nature of this structure.

To provide additional insight into the spectral dependence of the switching behavior, the active metasurfaces were simulated with a finite-difference solver to model the temperature-dependent reflection spectra for the various metasurfaces. The simulated spectra for the same sizes of nanodisks as in Figure 26a are shown in Figure 26b. The amount of switching and the change in the resonance full-width at half-maximum (FWHM) versus the resonance wavelength for both simulations and experimental data are shown in Figures 26c and 26d, respectively. Both the simulations and experimental results show that spectral switching can be maximized for a given geometry and resonant wavelength. In both simulations and experiment, the amount of switching increases with increasing resonance wavelength from ~900 to ~1400 nm and decreases slightly if the resonance wavelength is red shifted further. Similarly, both simulations and experiment show very little change in the FWHM up until ~1100 nm and a steady increase past this wavelength. However, simulations show a significantly larger magnitude of switching and change in the FWHM than the experimental results, which likely result from nanoscale inhomogeneities in the thin film, including variations in vanadium oxide morphology, especially faceting, pinholes or areas of dewetting.[169] With furthered optimization of the VO_2 deposition, the simulations show the promise to observe up to 160 nm of switching.

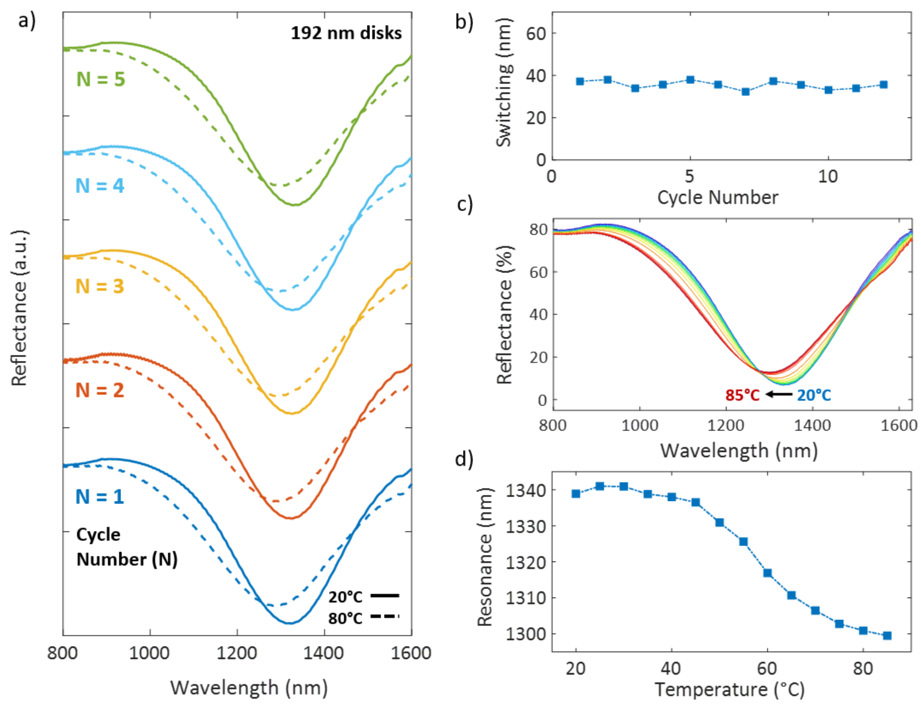

Figure 27. Reversibility and Temperature Dependence of Tuning. Characteristics of thermal switching for a metasurface consisting of 192 nm gold nanodisks (a) Thermal switching spectra over five cycles, which shows fully reversible switching. (b) Magnitude of switching over twelve cycles of the temperature (c) Switching spectra over one heating cycle taken in 5°C increments from 20°C to 85°C. (d) Extracted resonance wavelength as a function of temperature for the spectra displayed in (c). Manuscript is under review.

For further characterization of the VO_2 switching, the amount of switching for the 192 nm metasurface is analyzed over multiple cycles and smaller temperature steps. The temperature-dependent reflectance spectra of the 192 nm nanodisk metasurface over five cycles is shown in Figure 27a. In all, reflection spectra for this metasurface were collected over twelve temperature cycles; the shift in peak wavelength measured during each cycle is plotted in Figure 27b instead of the full spectra for clarity. For each cycle the magnitude of shift was observed to be 36 ± 2 nm, demonstrating the repeatable nature of the thermal switching. The reflection spectra of the 192 nm nanodisk metasurface was also measured at 5°C increments to characterize the continuity of the switching in more detail, and the results are shown in Figure 27c. The extracted resonance wavelength is shown as a function of temperature in Figure 27d. The resonance wavelength of the 192 nm metasurface displays little change until the temperature approaches 45°C. The resonance then begins to blue-shift with increasing temperature, reaching a maximum rate of change at 60°C. This implies a transition temperature of ~60°C for the fabricated VO_2 gap layer, which is slightly less than the reported value in literature for bulk VO_2.[156] Previous investigations of ALD-grown VO_2 have similarly shown a lowered transition temperature of 61°C.[170] Above 80°C, the resonance wavelength stabilizes at a final value of 1300 nm, which is blue-shifted by 40 nm compared to the resonance wavelength at room temperature. The lowered transition temperature and gradual phase shift occurring over a 40°C range when compared to bulk VO_2 is characteristic of the effect of boundary conditions on the VO_2 thin films.

In summary, I have demonstrated thermally tunable nanogap absorbers, which rely upon a robust, solid-state switching mechanism and possess a range of resonant wavelengths spanning more than 600 nm in the near-IR. These metasurfaces display up to 40 nm of switching that is fully reversible over more than 10 temperature cycles. The amount of switching increases with increasing resonance wavelength before tailing off slightly at around 1400 nm, a trend which is confirmed by finite-difference, time-domain simulations. With improvements to the VO_2 thin film deposition, such that the switching is increased to amounts similar to what is predicted in simulations, a variety of additional deeply subwavelength, all-solid-state, optoelectronic devices could be created using this platform including tunable photodetectors for multispectral FPAs.

5. Metasurface-Pyroelectric Photodetectors

Isolated thermal detectors, such as bolometric, pyroelectric, and thermoelectric devices, typically possess slow thermal response times on the millisecond scale.[32,54,62,171–174] However, if thermal detectors are not thermally-isolated, their response times can be much faster approaching that of state-of-the-art photovoltaic or photodiode detectors.[31] Several demonstrations in the 1970s achieved rise times at the nano- to pico-second scales with bulk pyroelectric crystals at room-temperature;[175–177] however, these devices exhibited prohibitively low responsivities in the nV/W-μV/W regime and relied upon intrinsic absorption features of the pyroelectric material, restricting operation to specific wavelengths and discouraging further development. Recent work with pyroelectric films have focused on leveraging pyroelectricity for hot-electron capture by using the inherent polarization of the material for charge separation. However, the large bandgap of pyroelectric materials restricts their applicability to the ultraviolet (UV) range and the fastest devices show a 53 μs response time.[178,179] Pyroelectric detectors are a promising detector technology capable of realizing nano and picosecond responses from transient, non-sinusoidal optical signals.

5.1 Pyroelectric Detectors

Pyroelectricity is the phenomena of a crystalline or polycrystalline material that exhibits a temperature dependent spontaneous electrical polarization. The pyroelectric effect was initially discovered in the 4th century BCE by the Greek philosopher, Theophrastus, when heated tourmaline crystals attracted pieces of wood, straw, copper and iron foils.[180,181] In modern times, pyroelectric materials have been used for photodetectors,[31,171,172,175,182–186] x-ray generators,[187] waste-heat harvesters,[2,3] particle accelerators,[188] among many other applications. Pyroelectric materials are anisotropic crystals with a non-centrosymmetric unit cell – i.e. crystals with an axis that do not have inversion symmetry – where out of the possible 32-point group symmetries of crystalline solids only 10 polar point groups satisfy this condition. The lack of inversion symmetry in these polar point groups generates a net polarization along a specific axis, which is dependent upon the temperature and mechanical strain of the material. As such, all pyroelectric materials are piezoelectric and a subset of pyroelectric materials are ferroelectric – materials were the spontaneous polarization can be reversed – shown pictorially in Figure 28.

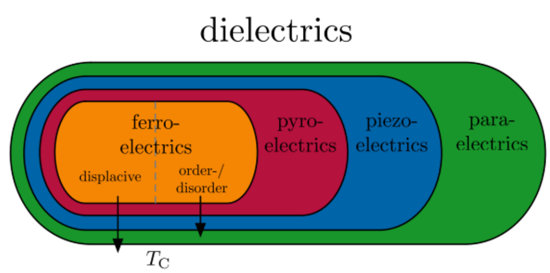

Figure 28: Classification of Dielectric Materials. The enclosed circles represent distinct subsets of dielectric materials. The ferroelectric arrows indicate the type of phase transformation at the Curie temperature, T_C. Figure from AIP Publishing.[189]

When pyroelectric materials are sandwiched between two conductors, the inherent polarization vector, $\mathbf{P}_S$, in [C·m^{-2}] will generate a surface charge density equal to the inherent polarization normal to the surface of the conductors. The electrostatics of a pyroelectric material in between two conductors are derived below in Equation 21.

$$\vec{D} = \varepsilon_0 \vec{E} + \vec{P} \tag{21}$$

Where **D** is the electric displacement field vector, **E** is the electric field vector, ε_0 is the free space permittivity, and **P** is the polarization vector. Vectors in the main text will be denoted with bold face text. The polarization of the pyroelectric material is the sum of the induced polarization from externally applied fields and the spontaneous polarization inherent to the material as shown in Equation 22. Thus, the electric displacement vector can be given according to Equation 23.

$$\vec{P} = \vec{P}_{ind} + \vec{P}_S \tag{22}$$

$$\vec{D} = \varepsilon_0 \vec{\varepsilon}_r \vec{E} + \vec{P}_S \tag{23}$$

The spontaneous polarization of pyroelectric materials is dependent upon the temperature and strain applied to the material. The pyroelectric coefficient, p, is a metric quantifying the slope of temperature dependence upon the electric displacement field as shown according to Equation 24.

$$p = \frac{d\vec{D}}{dT} = \frac{d\vec{P}_S}{dT} \tag{24}$$

In most cases, the electric field is much smaller than the spontaneous polarization and the pyroelectric coefficient can be written as the temperature derivative of the spontaneous polarization. Figure 29 shows an exemplary ferroelectric/pyroelectric material with its' temperature dependent spontaneous polarization, where past the Curie temperature, T_C, the material completely depolarizes. The pyroelectric coefficient is temperature dependent, where the highest values occur slightly below T_C.

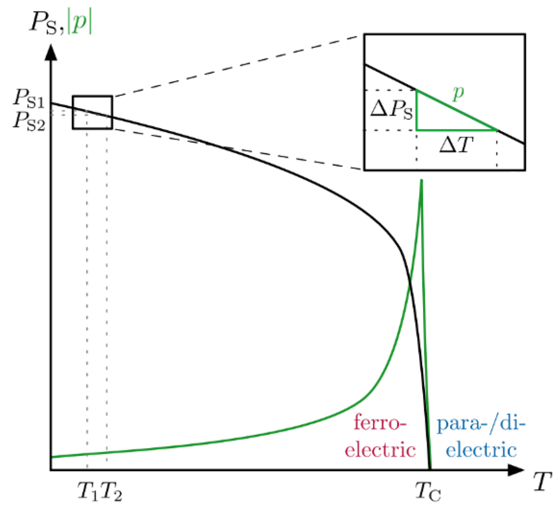

Figure 29: Spontaneous Polarization of a Pyroelectric Material. Example of the spontaneous polarization, $P_S(T)$, for a ferroelectric/pyroelectric material at several temperatures. Figure adapted from AIP Publishing.[189]

A Heckmann diagram in Figure 30 shows the interplay and cross coupling between thermal, electrical, and mechanical variables affecting a ferroelectric material. Thus, the electric displacement in Equation 23 will be dependent upon the mechanical strain, electric field, and temperature of the material. There can be significant cross-coupling between the different effects, for example thermally induced strain or thermoelastic coupling can generate an electrical signal through the piezoelectric effect. As such, there can be significant secondary and tertiary corrections to the pyroelectric coefficient and for tourmaline, triglycine sulfate (TGS), $(CH_2CF_2)_n$, and others the secondary pyroelectric coefficients are equal to or larger than the primary coefficient.

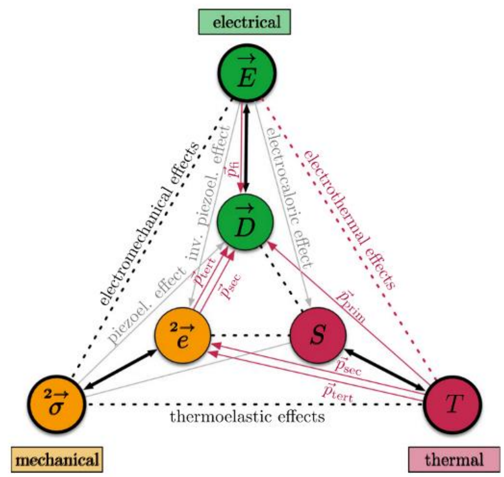

Figure 30: **The Heckmann Diagram.** Describing direct and cross-coupling terms between thermal, electrical, and mechanical state variables. Bold and non-bold circles represent intensive and extensive state variables, respectively. For reasons of simplicity magnetic properties are omitted. Figure from AIP Publishing.[189]

The updated pyroelectric coefficient accounting for all other changes to the displacement field from changes in temperature can be seen in Equation 25. For ensuing treatment, the pyroelectric coefficient will be treated as a scalar in the direction perpendicular to the conductors sandwiching the pyroelectric material or along the z-axis in this treatment.

$$p_{tot} = p_{prim} + p_{\sec} + p_{tert} + p_{fi} = \frac{\partial P_S}{\partial T} + \sum_{i,j,k}\left(\frac{\partial d_{ijk}\sigma_{ijk}}{\partial T} + \frac{\partial \mu_{ijk}\frac{\partial e_{ijk}}{\partial r_k}}{\partial T} + \varepsilon_0 \frac{\partial \varepsilon_{rijk}}{\partial T} E_{ijk} \right) \tag{25}$$

The primary pyroelectric coefficient, p_{prim}, is caused by an actual change in the spontaneous polarization from temperature fluctuations. The secondary coefficient, p_{sec}, captures the thermal effects on mechanical strain and the piezoelectric effect converting strain to a displacement field, where d_{ijk} is the piezoelectric tensor, σ_{ijk} is the mechanical stress tensor, and the indices i, j, and k are for the x, y, and z tensor components. The tertiary coefficient, p_{tert}, produces a polarization change due to spatial strain gradients ($\partial e/\partial r$), where μ_{nijk} is the flexoelectric tensor. Lastly, the field induced coefficient, p_{fi}, captures the temperature dependent changes in the relative dielectric permittivity tensor, ε_{rijk}. In general, the primary and secondary pyroelectric coefficients are the largest coefficients, where these two coefficients are shown for some common pyroelectric materials in Table 2.

Table 2: Pyroelectric Coefficients for Various Materials. Table from AIP Publishing.[181]

Material	Primary coefficient	Secondary coefficient	Total coefficient ($\mu C \cdot m^{-2} \cdot K^{-1}$)
Ferroelectrics			
$BaTiO_3$	−260	+60	−200
$PbZr_{0.95}Ti_{0.05}O_3$	−305.7	+ 37.7	−268
$LiNbO_3$	−95.8	+ 12.8	−83
$LiTaO_3$	−175	−1	−176
$Pb_3Ge_3O_{11}$	−110.5	+ 15.5	−95
$Ba_2NaNb_5O_{15}$	−141.7	+ 41.7	−100
$Sr_{0.5}Ba_{0.5}Nb_2O_6$	−502	−48	−550
$(CH_2CF_2)_n$	−14	−13	−27
Triglycine sulfate	+ 60	−330	−270
Nonferroelectrics			
CdSe	−2.94	−0.56	−3.5
CdS	−3.0	−1.0	−4.0
ZnO	−6.9	−2.5	−9.4
Tourmaline	−0.48	−3.52	−4.0
$Li_2SO_4 \cdot 2H_2O$	+ 60.2	+ 26.1	+ 86.3

The pyroelectric coefficient has units of [μC·m^{-2}·K^{-1}] and can be thought of as the amount of charge generated on the surface of the pyroelectric crystal from a 1 K change in temperature for a 1 m^2 area. Once the pyroelectric material is sandwiched between two conductors and connected to an external circuit, a pyroelectric current can be generated when heated or cooled. The pyroelectric current will be proportional to the area of the detector and can be given by Equation 26.

$$i_p = A\frac{dD}{dt} = A\frac{dD}{dT}\frac{dT}{dt} = Ap_{tot}\frac{dT}{dt} \qquad (26)$$

Thus, a pyroelectric detector is inherently a current source with a signal proportional to the area, pyroelectric coefficient, and rate of temperature change of the detector. Plugging in the temperature change from Equation 11 for a thermal detector exposed with a sinusoidally varying light source, the rate of temperature change can be given by Equation 27.

$$\frac{dT}{dt} = \frac{d\Delta T}{dt} = \frac{d}{dt}\left(\frac{\eta\Phi_0 R_{th}}{\sqrt{1+\omega^2\tau_{th}^2}}\right) = \frac{\omega\eta\Phi_0 R_{th}}{\sqrt{1+\omega^2\tau_{th}^2}} \qquad (27)$$

The current responsivity in this case for a sinusoidal signal can be given by Equation 28.

$$R_{i,pyro} = \frac{i_p}{\Phi_0} = p_{tot}A\frac{\omega\eta R_{th}}{\sqrt{1+\omega^2\tau_{th}^2}} \qquad (28)$$

For low frequencies $\omega \ll \tau_{th}^{-1}$, the current responsivity is proportional to ω. At frequencies greater than τ_{th}^{-1}, the responsivity approaches asymptotes to constant value indicating that pyroelectric detectors do not lose sensitivity for higher operation frequencies for a current readout approach. However, this derivation assumes the temperature change of the pyroelectric material occurs instantly upon absorption, where in reality the heat takes time to diffuse through the absorber into the pyroelectric material. As such, the responsivity response time of the pyroelectric detectors are inherently bound by the thermal diffusion time from the absorber into the pyroelectric material, which can be on the scale of ns to μs for traditional blackened absorbers. Nanophotonic absorbers on the other hand reduce the thermal diffusion time by localizing the absorption close to the pyroelectric material and can show thermal diffusion times on the order of 1's to 10's of picoseconds.[31]

5.2 Film-Coupled Nanocubes with Pyroelectric Film

Here, I experimentally and computationally demonstrate the pico- and nano-second dynamics of a room-temperature, pyroelectric photodetector which is integrated with a metallic metasurface that acts as a perfect absorber and on-chip spectral filter. The dimensions of the metasurface elements, and thus their associated plasmon resonance, solely define the detection wavelength of the detector without restrictions imposed by the bandgap of the material or instrinsic absorption features. Leveraging colloidal deposition and lithographic techniques, I demonstrate a pyroelectric detector with sub-nanosecond rise times and responsivities up to 180 mV/W. The detector structure consists of a film-coupled plasmonic metasurface[100] deposited on top of an aluminum nitride (AlN) pyroelectric film deposited on a p-type Si substrate as shown in Figure 31a.

Light incident upon these photodetectors interacts with the resonant plasmonic metasurface giving rise to the dip in reflectance shown in Figure 31d. At the fundamental plasmonic resonance, over 98 percent of the incident optical energy is converted into localized charge density oscillations confined to the metallic surfaces (i.e. localized surface plasmons) between the Ag nanocube and the Au film.[100] Subsequently, the localized surface plasmons decay at femtosecond timescales and generate heat through electron-phonon scattering (e-ph scattering) on the order of several picoseconds.[74,114,120,190] The generated heat then diffuses through the 75 nm thick Au film into the underlying AlN on the order of tens of picoseconds. A simulated heat map illustrates this diffusion process in Figure 31b-c, which shows the metamaterial unit cell 1 ps and 40 ps after excitation with a 100 femtosecond (fs) optical pulse. Pyroelectric materials, such as AlN, possess a temperature-dependent spontaneous polarization and upon heating, their polarization is altered. Uniquely, pyroelectric materials exhibit increased pyroelectric coefficients when heated below their Curie temperature which is ~2000˚C for AlN[191] and are thus well suited to ambient- or above- ambient temperature operation. Sandwiching the pyroelectric material between two conductive films allows electrical charges to accumulate on the conductor-pyroelectric interfaces in an amount proportional to the polarization as shown conceptually in Figure 31b-c. Time-varying optical/thermal signals alter the density of interfacial charges in the sandwiched structure generating a pyroelectric voltage which drives a current when connected to an external circuit as shown in Equation 26, where A is the detector area, p is the pyroelectric coefficient, and dT/dt is the rate of temperature change of the pyroelectric film. The produced time-varying pyroelectric signal is measured using a phase-sensitive electrical detection scheme utilizing a lock-in amplifier.

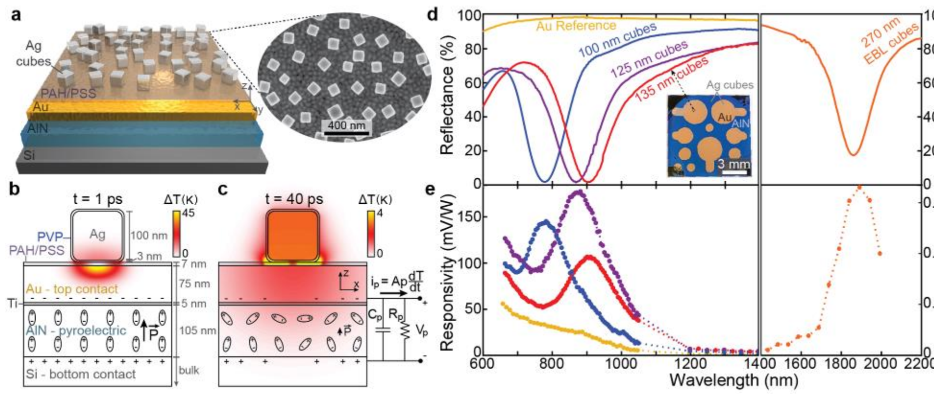

Figure 31: Pyroelectric-Metasurface Detector Concept. a) Schematic of the vertical detector structure with a plasmonic metasurface deposited on a poly-crystalline AlN pyroelectric layer. An SEM image of the fabricated metasurface with 100 nm Ag cubes. b-c) Depiction of thermal impulse response within a single metamaterial element 1 ps and 40 ps after an excitation pulse. The temperature change is overlaid with the pyroelectric detection concept and the equivalent circuit of the pyroelectric film. d) Reflection spectra of three colloidal metasurface-pyroelectric detectors, an Au reference detector, and an EBL fabricated metasurface-pyroelectric detector. Image of the 135 nm cube metasurface-pyroelectric detectors with 3.0, 2.0, 1.5, and 1.0 mm diameters. e) Normalized photovoltage spectra of the five different detectors showing a clear correlation with the absorption spectra. Figure from Nature Publishing.[31]

Experimentally, the colloidal metasurface-pyroelectric detectors are fabricated with two readily established techniques for both the pyroelectric films[192] and for the metasurfaces[65] capable of realizing detectors ranging from 0.0044 mm^2 to 7.0 mm^2 over wafer-scale areas. A top-down SEM image in Figure 31a shows the uniformity of the self-assembled 100 nm Ag nanocubes on an Au film. Electron-beam lithography (EBL) was used to fabricate resonances further into the infrared by interchanging the Ag nanocubes with 40 nm thick Au nanoparticles with larger edge lengths. To characterize the spectral responsivity, five spectrally-different detectors were fabricated as shown in Figure 31d-e, where three consist of colloidal metasurfaces with varied resonances by depositing 100, 125, or 135 nm edge length cubes, one of 250 nm edge length Au nanoparticles patterned with EBL, and one of an Au film as a control. The metasurface-pyroelectric detectors were exposed to a chopped, tunable laser, and the resultant photovoltage was measured for each wavelength. Figure 31d-e show clear agreement between the absorption spectra and responsivity, where the peak responsivities ranged between 0.11-0.18 V/W for the 7.0 mm^2 colloidal metasurfaces and showed greater than 30 dB of selectivity between the wavelengths of fundamental resonance and 1500 nm. The increasing responsivity of the Au control for shorter wavelengths occurs due to the interband absorption of Au and can be reduced using different plasmonic materials such as Pt, Ag and Al or mitigated through background subtraction. The EBL metasurfaces similarly show an agreement between the absorption spectrum and the spectral responsivity peaking at 0.33 mV/W for the 1900 nm wavelength for a 0.0072 mm^2 detector. By simply varying the nanoparticle size, the resonances of the metasurface-pyroelectric detectors displayed photovoltages between 660-2000 nm surpassing the spectral range of conventional InGaAs detectors.

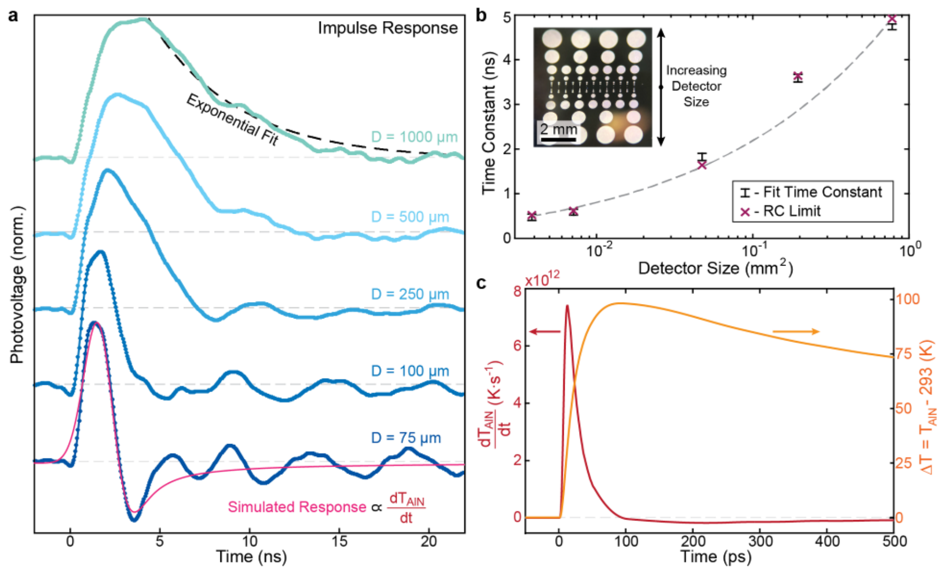

Figure 32: Temporal Metasurface-Pyroelectric Detector Response. a) Photovoltage impulse response of metasurface-pyroelectric detectors after excitation with a 100 fs laser pulse at time zero (0 ns). Detectors with different diameters, D, show varying response times and are overlaid with the simulated response for the 75 µm detector convolved with its' RC limit. b) Size-dependent exponential time constants extracted from fitting each impulse response, which are shown along with the RC limited responses and a dashed line to guide the eye. Inset image contains the fabricated metasurface-pyroelectric detectors with diameters ranging from 1000 µm to 75 µm. c) Simulated thermal impulse response for the 75 µm detector. The rate of temperature change, dT/dt, is directly proportional to the generated pyroelectric voltage as described by Equation 26. Figure from Nature Publishing.[31]

The inherent speed of these pyroelectric-metasurface detectors was found through analyzing the impulse response dynamics. Experimentally, the impulse response was measured by exciting the detectors with a 1 kHz, 100 fs laser at a wavelength of 800 nm provided by Prof. Smith and Prof. Litchinitser. Two physical mechanisms determine the ultimate speed of these detectors, the thermal time constant and the electrical time constant. The simulated temperature change, dT/dt, found with

COMSOL shows a 6 ps rise time with a 25 ps full-width half maximum (FWHM) which is significantly faster than the instrument and electrical responses in the actual device. As such, the capacitance of the sandwiched pyroelectric detectors is the dominant temporal aspect, due to the slower RC time constant. To experimentally investigate the temporal dependence of the metasurface-pyroelectric detectors, the capacitance of the detectors was varied by fabricating detectors with diameters ranging from 75-1000 μm. The impulse response for five different detector sizes is shown in Figure 32a along with the simulated response for the 75 μm detector. For each detector size, the impulse response was fit to a single-exponential decay and the extracted time constant is plotted according to the detector area in Figure 32b. The total RC time constant of the detector, probe, and oscilloscope is also overlaid on the size-dependence. The agreement between the RC time constant and the extracted exponential decay indicates that the RC time constant is indeed the dominant temporal factor for these detectors. Even with the RC-limited responses, the thermal detectors achieved response times down to a 500 ps exponential decay, a 1.67 ns full-width half maximum (FWHM), and a 300 MHz bandwidth as shown in Figure 33.

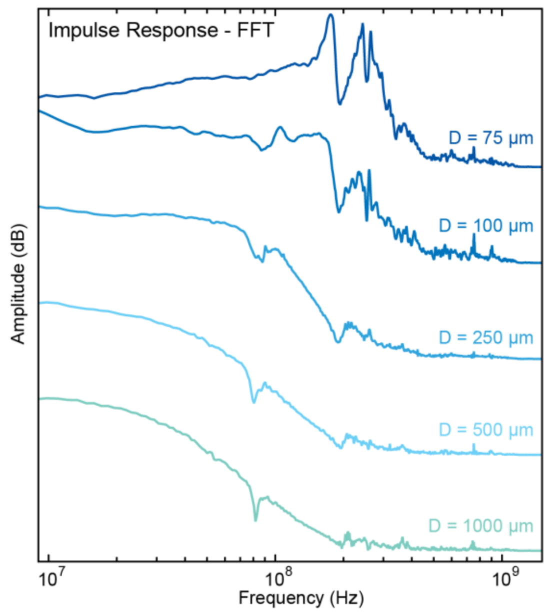

Figure 33: Bandwidth from the Impulse Response. The detectors are clearly limited by their electrical bandwidth as the thermal diffusion time does not change with the area of the detector, but the capacitance does. The smallest detector with the lowest capacitance shows the highest bandwidth as expected. The instrument limited response was found to be ~500 MHz due to the 1 GHz bandwidth of the oscilloscope and the capacitances of the detector and contacting probes, limiting the measurement out to the GHz regime. Figure from Nature Publishing.[31]

Computationally, finite-element simulations were used to estimate the thermal-temporal limits of the detectors. For plasmonic structures, the absorbed power density can be calculated via the conductive losses from charge oscillations induced by the plasmonic mode, which depends upon the local electric field, the oscillation frequency, and the imaginary permittivity.[120] In the vicinity of plasmonic nanostructures, large electric fields can produce highly-localized, sub-wavelength absorption regions (Figure 38). The electromagnetic simulations were then coupled into a solid-state heat transfer simulation, where the heat source is spatially-defined by the absorbed power density and temporally-defined by a 100 fs FWHM Gaussian pulse. The normalized temperature maps in Figure 31b-c were taken 1 ps and 40 ps after excitation. To account for any size-dependent thermal relaxation, full detectors were simulated with 75-1000 μm diameters, which showed less than 1 percent deviations in their extracted lifetimes between different detector sizes. The 75 μm thermal simulation included in Figure 32c shows an 10-90 percent rise time of 41 ps and a bi-exponential decay with a primary and secondary relaxation of 580 ps and 4.91 ns. To overlay the simulated and experimental results, the simulated photoresponse was calculated according to Equation 26, which relates the rate of temperature change (Figure 32c), the detector area (0.0044 mm^2), the termination resistance (51.8 Ω), and the pyroelectric coefficient. The pyroelectric coefficient for AlN was extracted by fitting the magnitude of the simulation to the experimental results, which was found to be 1.9 $\mu C/m^2K$ as compared to the directly measured 6-8 $\mu C/m^2K$ in a previous work.[193] The discrepancy between these values likely arises from transient absorption effects when exciting with the fs laser pulses, which are unaccounted for by the thermal simulations. For better visual comparison between the simulated and measured impulse responses, the simulated response was convolved with a 500 MHz Gaussian pulse corresponding to the experimental instrument-limited response time. The simulated and experimental impulse response for the 75 μm detector (Figure 32a) show precise temporal agreement for both the AlN depolarization and repolarization upon heating and cooling following the fs pulse. This agreement between the experimental and simulated results demonstrates the possibility of realizing much faster metasurface-pyroelectric detectors potentially with thermally-limited 25 ps response times.

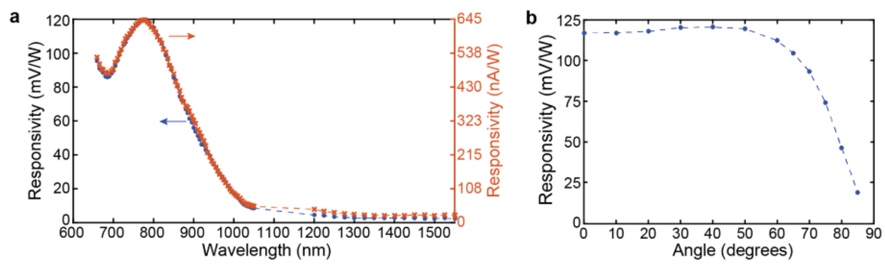

Figure 34: Responsivity Characterization. a) Photovoltage and photocurrent responsivities of a detector fabricated with 100 nm nanocubes. b) The angle dependent responsivity of the same detector showing large responsivities out to 60° angles. Figure from Nature Publishing.[31]

After demonstration of the picosecond-scale temporal dynamics, the detector responsivity was further characterized. Results from two different readout schemes for the pyroelectric detectors are shown in Figure 34a, where the low-impedance readout scheme allows for photocurrent measurements and the high-impedance readout for measuring photovoltage. Both readout schemes possess a spectral profile matching the 100 nm nanocube metasurface shown in Figure 31d-e. The angle dependence of the same detector is depicted in Figure 34b and shows the responsivity only decreases by 7 percent out to 60-degree angles, which closely follows the metasurface angular absorption profile shown previously.[65] The power dependence was then measured to characterize the noise and sensitivity of this detector. The noise floor of the 7.0 mm^2 detector is depicted in Figure 36a and shows an SNR of 1 for a laser power of 1.7 μW corresponding to an irradiance of 24 μW/cm². In pyroelectric/thermal detection there are multiple noise sources that determine the sensitivity of the detector such as Johnson noise, thermal noise, 1/f noise, and amplifier noise. In this work, Johnson noise dominates as it depends upon the resistance of the detector and its temperature, which can be large for the room-temperature pyroelectric films. The 675 kΩ resistance of the 7.0 mm² detector was extracted from an IV curve as shown in Figure 35.

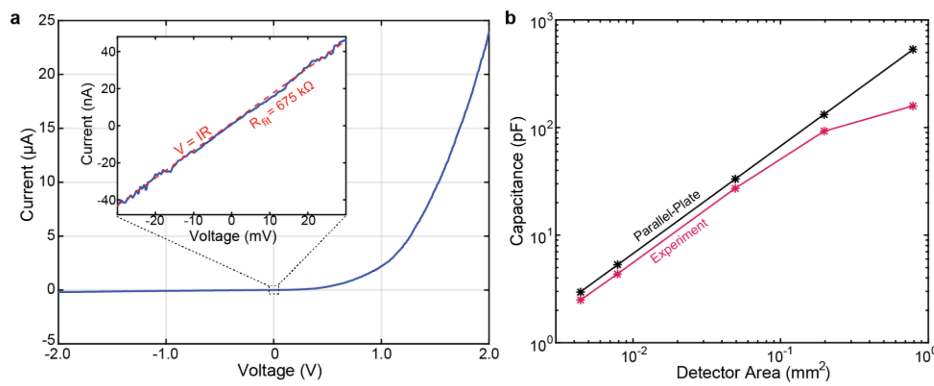

Figure 35: Electrical Characteristics. a) The Schottky diode response arising from the contact between the pyroelectric AlN and the Ti adhesion layer. The inset shows a linear I-V response for the area of device operation along with the linear fit showing a 675 kΩ resistance at low voltages. b) The size-dependent capacitance of the metasurface-pyroelectric detectors showing a near-ideal parallel plate capacitance for smaller detector sizes. Figure from Nature Publishing.[31]

The I-V behavior of this thermal detector is analogous to a diode response arising from the Schottky diode forming between the AlN and Ti adhesion layer. The p-type Si substrate and the p-type AlN will prevent the formation of a p-n junction. The inset shows an enlarged plot of the origin, where the I-V curve shows nearly resistive behavior for low voltages. The RC characteristics of the smaller diameter detectors, 75-

1000 μm, were measured with a LCR meter using a 1 MHz carrier frequency. The measured capacitances from the LCR meter are overlaid in Figure 35b with the corresponding parallel plate capacitances for each detector calculated from their areas. The impulse responses were measured on Prof. Padilla's Keysight InfiniiVision oscilloscope with a 1 GHz bandwidth and an 8 pF input capacitance. The effective capacitance of the micromanipulator, SMA, and contact was found to be 180 pF by fitting the extracted exponential time constants to that of the RC time constant of the entire electrical circuit. The contact capacitance can be significantly reduced by bonding the detectors to a printed circuit board (PCB) and using photolithographic contacts and wire bonding to connect the detectors to an SMA connector directly. The resistance of the oscilloscope termination, contact resistance, tungsten probe, and SMA cable was measured to be 51.8 Ω.

The theoretical Johnson noise for this detector with a high-impedance amplifier was 106 nV/√Hz as shown in Figure 36b which closely matches the mean measured NSD of 132 nV/√Hz. The low-impedance amplifier noise measurements showed better agreement between the calculated Johnson noise at 0.156 pA/√Hz and the mean NSD of 0.162 pA/√Hz. The noise equivalent power (NEP) is calculated by dividing the NSD by the spectral responsivity. As expected, the highest NEP of 679 nW/√Hz occurs at the highest responsivity equating to the peak metasurface absorptance as seen in Figure 35c and can be improved by cooling the detector to decrease the Johnson noise or through thermal isolation. The specific detectivity (D*) normalizes the performance to the detector size and is calculated by dividing the area of the detector by the NEP. As such, this metasurface-pyroelectric detector shows a peak detectivity of 3.9×10^5 Jones, which can be improved using back-thinned, thermally isolated pixels, cooling the detectors, or vacuum packaging of the detector. However, this demonstration focused upon the high-speed transient dynamics of the thermal diffusion through the pyroelectric detector necessitating the detectors are not thermally isolated. For practical devices and multispectral FPAs it is highly desirable to thermally isolate the detectors.

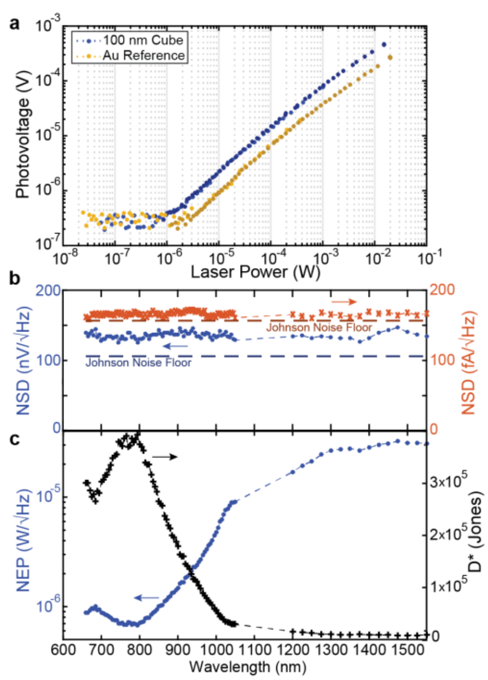

Figure 36: Noise Performance. a) Power dependence of detector with 100 nm cubes showing the noise floor for powers below 1 μW, and a nearly linear photovoltage for increasing powers. b) Noise spectral density (NSD) for both current and voltage measurements of the same detector. c) Noise equivalent power (NEP) calculated from the NSD showing μW sensitivity similar to the power dependence noise floor plotted along with the specific detectivity (D*). Figure from Nature Publishing.[31]

The simulations were conducted in COMSOL Multiphysics utilizing the Wave Optics module for the absorptive characteristics and the Heat Transfer module for the separate thermal simulations. The electromagnetic (EM) simulation was conducted in the frequency domain with the boundary conditions laid out in Figure 37. The results from the EM simulations were fed into a solid-state heat transfer simulation with the boundary conditions in Figure 37. The x-y boundary in air was held at a constant temperature to prevent reflections of the thermal impulse from the air. The x-y boundary in the Si substrate allowed $2.6 \cdot 10^7$ W/m^2K of constant heat flux arising from the thermal conductivity of Si (130 W/mK) and assuming the surface of constant temperature lies 5 μm below the simulated boundary. The heat flux boundary condition allowed for faster simulations and did not change the thermal relaxation dynamics when compared to simulations with thick Si substrates up to 10 μm.

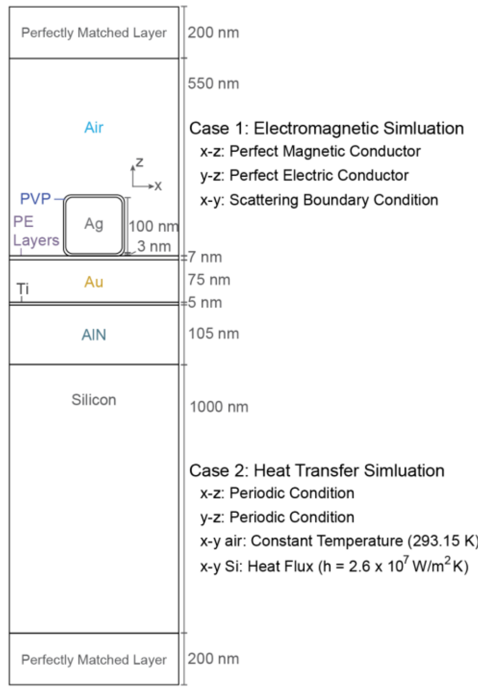

Figure 37: Metasurface Simulation Schematic. Schematic of a single metasurface element used for both the electromagnetic and heat transfer simulations and their associated boundary conditions. Figure from Nature Publishing.[31]

The absorptive characteristics of the detectors were simulated with the Wave Optics module to calculate the absorbed power density at the fundamental plasmon resonance. The absorbed power density shown in Figure 38b was calculated according to Equation 19. The electric field map is highly-localized in the gap region between the Ag cube and the Au film as shown in Figure 38a and is utilized for the absorbed power density calculation shown in Figure 38b. The absorption spectra shown in Figure 38c is overlaid with the absorption amount occurring in each of the metasurface constituents. The constituent absorptions were calculated by integrating the absorbed power density over the volume of the specific material. The structure was designed to localize the absorption in the Au film for faster thermal diffusion. Temporally, the plasmon is expected to produce a measurable thermal signature impulse that is delayed by 200 fs after the initial excitation, which is consistent with previous investigations showing a mean plasmon decay and e-e scattering time of 185 fs.[114] For the transient thermal simulations, a 100 fs Gaussian thermal pulse delayed by 200 fs was utilized for the temporal excitation and the absorbed power density for the spatial excitation, where the pulse power was modeled after actual experiments with a 100-fs laser excitation, 3 W/cm^2 averaged irradiance, and a 1 kHz repetition rate.

The full detector thermal simulations were similarly computed using the COMSOL Multiphysics package with the Heat Transfer module. A simplified model was essential to simulate the full detectors as a 75 μm detector covered in 100 nm nanocubes could contain up to 90,000 metasurface elements, which is not feasible to simulate individually. Thus, the thermal generation from the metasurface elements is assumed to be spatially uniform on the surface of the Au film. The simulated detectors with diameters ranging between 75-1000 μm consisted of a vertical stack of a 10 μm thick air buffer, a 75 nm Au film, a 105 nm AlN active layer, and a 20 μm thick Si substrate, where the thermal excitation was carried out through a boundary heat source on top of the 75 nm Au film. The same Gaussian 100 fs pulse was utilized for excitation and the transient dynamics were captured for the AlN film. A 2D simulation using radial symmetry was conducted since the detectors were circular, where all boundaries other than the axial symmetry were placed at a constant temperature of 293.15 K. Lateral diffusion for the macroscopic detectors larger than 25 μm diameters had a negligible effect on the thermal relaxation. These macroscopic simulations show close agreement with the thermal simulations of the single metasurface element despite ignoring the absorption and thermal diffusion from the Ag nanocubes.

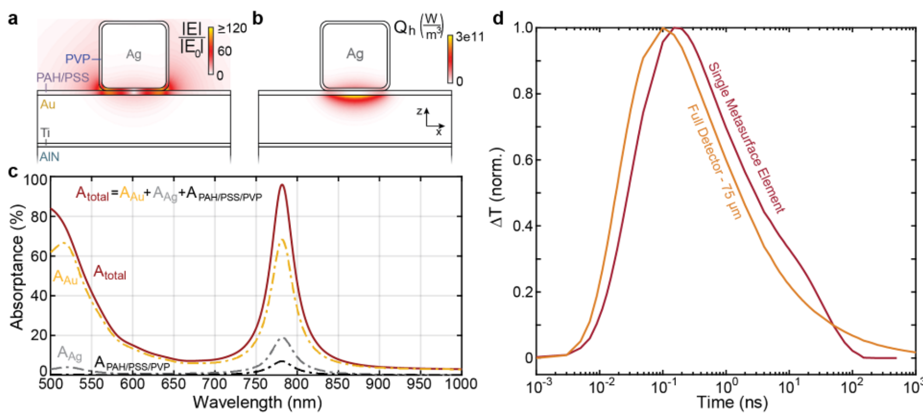

Figure 38: Metasurface Simulation Results. a) Electric-field profile of a plasmonic metasurface element at the fundamental plasmon resonance. b) Absorbed power density of nanostructure exposed with an irradiance of 3 W/cm2, showing the majority of absorption occurs in the Au. c) Simulated spectral absorption showing 96 percent absorption at the fundamental resonance around 780 nm. Dashed lines show absorption percentages from specific constituents of the plasmonic metasurface. d) Simulated temperature change of AlN film after excitation with a fs-pulse shown for two different simulations. Red: The single metasurface element simulation (red). Orange: The full detector simulation of the 75 μm diameter. Figure from Nature Publishing.[31]

In comparison to other high-speed infrared detectors, Table 3 summarizes the temporal resolution and NEP of commonly used near-infrared photodetectors and recent demonstrations.[32,194–197] The temporal resolution of this pyroelectric detector is six orders of magnitude faster than typical pyroelectric detectors because its' lack of thermal isolation and picosecond thermal diffusion through the integrated metasurface. The

NEP is slightly better for commercial detectors, because the responsivity this non-isolated detectors reduced by the larger thermal capacitance and conductance. However, simulations show these pyroelectric photodetectors can approach the carrier-limited lifetimes of high-performance Si and InGaAs photodiodes at the expense of extra noise. Furthermore, the presented detectors have a spectral bandwidth beyond that of InGaAs and could be utilized in spectral windows not covered by these common detectors. The spectral range is not included in the table below as several references did not characterize the detector's spectral range.

Table 3: Comparison of Common Near-Infrared Photodetectors. Table from Nature Publishing.[31]

Detector	Material	Temporal Resolution	NEP $nW/Hz^{0.5}$	Temperature	Reference
This Report (Pyroelectric)	AlN	1.67 ns - Exp. 25 ps - Sim.	679	Uncooled	
Standard Pyroelectric	PVDF/PANI	> 10 ms	235	Uncooled	[194]
Photoconductive	PbS	9 ms	417	Uncooled	[195]
Photoconductive	MCT	10 ns	0.210	Uncooled	Thorlabs PDAVJ10
Thermoelectric	Bi_2Te_3/Sb_2Te_3	337 μs	3.5	Uncooled	[32]
Photodiode	Sn-Perovskite	7.4 μs	0.015	Uncooled	[196]
Schottky	Si-Graphene	1.35 ns	0.35	Uncooled	[197]
Photodiode	InGaAs	80 ps	0.00044	Uncooled	Newport 818-BB-51

In conclusion, a room-temperature, ultrafast thermal photodetector has been demonstrated by integrating a metasurface with a nanometer-scale pyroelectric film enabling an instrument-limited 700 ps rise time, a 1.67 ns FWHM, and a 300 MHz bandwidth which is almost six orders of magnitude faster than previously demonstrated spectrally-selective thermal detectors.[32,54,62,171–174] Thermal transport simulations closely match the experimental results and show the potential for response times down to 25 ps for smaller detectors approaching that of semiconductor photodiodes with carrier-limited responses of ~30 ps.[198] On-chip spectral filters created by the integrated metasurfaces were used to realize spectrally-selective detection from 660-2000 nm. The wavelength range could be further extended into the ultraviolet-visible (UV-VIS) region through substitution of Au with Pt, Ag, or Al and into the mid-infrared by fabricating larger nanoparticles via EBL or inexpensive, large-area techniques such as deep-UV lithography or the synthesis of larger colloidal nanoparticles. These large-area devices show the potential for realizing uncooled, thermal photodetectors with high responsivities and GHz speeds without the spectral limitations of bandgap-based detectors. Furthermore, integrating these metasurface-pyroelectric photodetectors with multiscale patterning techniques[112] could enable on-chip multispectral focal plane arrays, where integration of dynamically tunable metasurfaces[123,124] could allow for spectral reconstruction with a single photodetector.[199,200]

5.3 Toward Multispectral FPAs with Metasurface-Pyroelectric Detectors

Current efforts on these metasurface-pyroelectric detectors are focused upon i) investigating the thermal diffusion limit out to 67 GHz bandwidths, and ii) creation of a 4x4 multispectral pixel array with simultaneous electrical readouts. For instance, a single pixel of the fabricated 4x4 multispectral pixel array is shown in Figure 39. The reflection and photovoltage spectra of this pixel is shown in Figure 31d, which is denoted as the 270 nm EBL detector since the metasurfaces were fabricated with electron-beam lithography.

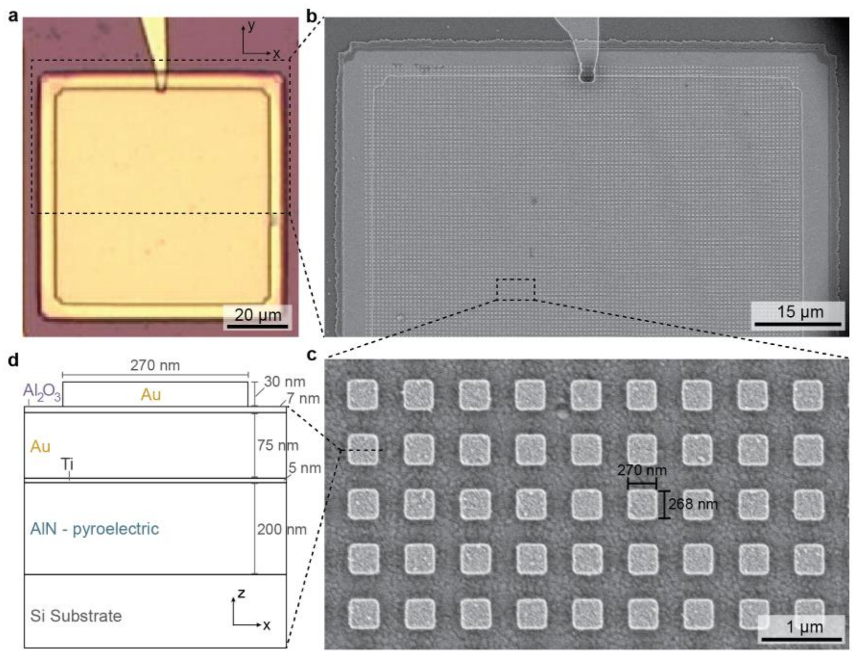

Figure 39: Multispectral Array of Metasurface-Pyroelectric Detectors. a) Microscope image of an 85x85 μm detector with a 75x75 μm active area and a 100 μm pixel pitch. b) SEM image of the detector showing the EBL fabricated nanoparticle array. c) SEM showing 270 nm Au nanoparticles fabricated on the detector. d) Cross-section of a single metasurface element in the center of the detector. Figure from Nature Publishing.[31]

These EBL metasurface-pyroelectric detectors were fabricated to demonstrate the potential of pyroelectrics to exhibit resonances and photovoltages over a broad wavelength range which is beyond the sensitivity of InGaAs and Si, where the EBL detector shown possesses a primary resonance 1850 nm. The 85×85 μm Au/AlN pads with their internal 75×75 μm active region can be clearly seen in Figure 38a along with the top contact with a trace leading to the edge of the sample at the top of the image. The metasurface deposited on the detector can be clearly seen in the SEM images of Figure 38b-c. The average lateral particle size is 269 ± 1 nm and possesses a 29.3% fill-fraction, where a cross-section of the metasurface elements are shown in Figure 39d. The resonance of the other detectors were changed by altering the edge-lengths of the EBL cubes between 50-350 nm, resulting in evenly spaced absorption resonances spanning from 700-2600 nm. While this initial demonstration possesses relatively large 100 μm pixel pitches, the pixel pitch can be pushed down to commercially-relevant sizes, 20 μm or below, with the maturation of the integrated readout circuit. The present readout consists of a single channel femtoampere electrometer amplifier wire-bonded to the desired detector, however a PCB with 16 amplifier channels with a multiplexed ADC is under development. There is much future work and maturation required to facilitate the technology transfer of these spectrally selective thermal detectors, but these detectors are a promising technology for realizing a new generation multispectral focal plane arrays.

6. Conclusion

Through this dissertation, I have demonstrated the promise of spectrally-selective thermal detectors for creation of multispectral FPAs for applications ranging from precision agriculture to industrial process monitoring. Through recent theoretical developments in other works, spectrally selective thermal detectors were shown to outperform ideal photoconductive and photovoltaic detectors from the MWIR to the VLWIR. In my initial work, I developed a colloidal metasurface platform capable of producing highly-absorbing filters over large areas with resonances spanning from 340-2740 nm, while allowing for the nanoscale thermal generation to be spatially engineered. Subsequently, I demonstrated that the deposition of colloidal nanoparticles can be laterally controlled for creation of multispectral metasurface arrays. I then integrated two dynamic spectral tuning mechanisms into the colloidal metasurfaces, promising for future creation of spectrally tunable photodetectors for spectral reconstruction. Furthermore, I integrated film-coupled colloidal metasurfaces with pyroelectric films that exhibited sub-nanosecond instrument limited response times, where finite-element simulations reveal the potential of these pyroelectric detectors to match the response times of state-of-the-art photodiodes. Current efforts are seeking to reveal the thermal diffusion limit of these metasurface-pyroelectric detectors out to 67 GHz, while non-isolated 4x4 multispectral detector arrays are being constructed from the metasurface-pyroelectric detectors for multispectral imaging demonstrations. Overall, these spectrally selective thermal detectors are a promising technology capable of disrupting the low cost, low form-factor spectral imaging market and provide an interesting platform to conduct research into photothermal generation and thermal diffusion at the nanoscale.

References

[1] Rogalski, A. Next decade in infrared detectors. in *Electro-Optical and Infrared Systems: Technology and Applications XIV* (eds. Huckridge, D. A., Ebert, R. & Bürsing, H.) 100 (SPIE, 2017). doi:10.1117/12.2300779.

[2] Pandya, S. *et al.* Pyroelectric energy conversion with large energy and power density in relaxor ferroelectric thin films. *Nat. Mater.* **17**, 432–438 (2018).

[3] Yang, Y. *et al.* Pyroelectric nanogenerators for harvesting thermoelectric energy. *Nano Lett.* **12**, 2833–2838 (2012).

[4] Mukherjee, S. & Muralidharan, B. Electronic Fabry-Perot Cavity Engineered Nanoscale Thermoelectric Generators. *Phys. Rev. Appl.* **12**, 024038 (2019).

[5] Kraemer, D. *et al.* High-performance flat-panel solar thermoelectric generators with high thermal concentration. *Nat. Mater.* **10**, 532–538 (2011).

[6] Lowe, A., Harrison, N. & French, A. P. Hyperspectral image analysis techniques for the detection and classification of the early onset of plant disease and stress. *Plant Methods* vol. 13 80 (2017).

[7] Gago, J. *et al.* UAVs challenge to assess water stress for sustainable agriculture. *Agricultural Water Management* vol. 153 9–19 (2015).

[8] Constantin, D., Rehak, M., Akhtman, Y. & Liebisch, F. Detection of crop properties by means of hyperspectral remote sensing from a micro UAV. in *Bildanalyse in der Landwirtschaft* vol. 88 129–137 (2015).

[9] Johnson, W. R. & Hook, S. J. Mid and thermal infrared remote sensing at the Jet Propulsion Laboratory. *Infrared Technol. Appl. XLII* **9819**, 98190H (2016).

[10] Sharma, L. K. & Bali, S. K. A review of methods to improve nitrogen use efficiency in agriculture. *Sustain.* **10**, 51 (2017).

[11] Vigneau, N., Rabatel, G., Roumet, P. & Ecarnot, M. Field hyperspectral imagery as a tool for plant monitoring : application to wheat nitrogen content. in *Conférence Internationale AgEng 2010 sur les Technologies agricoles* 6–8 (2010). doi:hal-00581329.

[12] Herrmann, I., Karnieli, A., Bonfil, D. J., Cohen, Y. & Alchanatis, V. SWIR-based spectral indices for assessing nitrogen content in potato fields. *Int. J. Remote Sens.*

31, 5127–5143 (2010).

[13] Balafoutis, A. *et al.* Precision agriculture technologies positively contributing to ghg emissions mitigation, farm productivity and economics. *Sustain.* **9**, 1339 (2017).

[14] Basso, B., Shuai, G., Zhang, J. & Robertson, G. P. Yield stability analysis reveals sources of large-scale nitrogen loss from the US Midwest. *Sci. Rep.* **9**, (2019).

[15] Farley, V. *et al.* Chemical agent detection and identification with a hyperspectral imaging infrared sensor. in *Electro-Optical Remote Sensing, Detection, and Photonic Technologies and Their Applications* (eds. Kamerman, G. W. et al.) vol. 6739 673918 (2007).

[16] Briottet, X. *et al.* Military applications of hyperspectral imagery. in *Targets and Backgrounds XII: Characterization and Representation* (eds. Watkins, W. R. & Clement, D.) vol. 6239 62390B (2006).

[17] Bao, J. & Bawendi, M. G. A colloidal quantum dot spectrometer. *Nature* **523**, 67–70 (2015).

[18] Jang, W. Y., Ku, Z., Urbas, A., Derov, J. & Noyola, M. J. Plasmonic superpixel sensor for compressive spectral sensing. *IEEE Trans. Geosci. Remote Sens.* **53**, 3471–3480 (2015).

[19] Goldsmith, J. H., Vangala, S., Hendrickson, J. R., Cleary, J. W. & Vella, J. H. Long-wave infrared selective pyroelectric detector using plasmonic near-perfect absorbers and highly oriented aluminum nitride. *J. Opt. Soc. Am. B* **34**, 1965 (2017).

[20] Jang, W. Y. *et al.* Experimental demonstration of adaptive infrared multispectral imaging using plasmonic filter array. *Sci. Rep.* **6**, 34876 (2016).

[21] Talghader, J. J., Gawarikar, A. S. & Shea, R. P. Spectral selectivity in infrared thermal detection. *Light Sci. Appl.* **1**, e24–e24 (2012).

[22] Christiansen, A. B. *et al.* Black metal thin films by deposition on dielectric antireflective moth-eye nanostructures. *Sci. Rep.* **5**, (2015).

[23] Li, J. M. *et al.* Electrodeposition and characterization of nano-structured black nickel thin films. *Trans. Nonferrous Met. Soc. China (English Ed.* **23**, 2300–2306 (2013).

[24] Zheng, B., Wang, W., Jiang, G. & Mei, X. Fabrication of broadband antireflective black metal surfaces with ultra-light-trapping structures by picosecond laser texturing and chemical fluorination. *Appl. Phys. B Lasers Opt.* **122**, 180 (2016).

[25] Pfund, A. H. Bismuth black and its applications. *Rev. Sci. Instrum.* **1**, 397–399 (1930).

[26] Lehman, J., Theocharous, E., Eppeldauer, G. & Pannell, C. Gold-black coatings for freestanding pyroelectric detectors. *Meas. Sci. Technol.* **14**, 916–922 (2003).

[27] More-Chevalier, J. *et al.* Black aluminum-coated Pt/Pb(Zr0.56Ti0.44)O3/Pt thin film structures for pyroelectric energy harvesting from a light source. *J. Appl. Phys.* **126**, 214501 (2019).

[28] Zabek, D., Seunarine, K., Spacie, C. & Bowen, C. Graphene Ink Laminate Structures on Poly(vinylidene difluoride) (PVDF) for Pyroelectric Thermal Energy Harvesting and Waste Heat Recovery. *ACS Appl. Mater. Interfaces* **9**, 9161–9167 (2017).

[29] Kruse, P. W. A comparison of the limits to the performance of thermal and photon detector imaging arrays. *Infrared Phys. Technol.* **36**, 869–882 (1995).

[30] Rogalski, A. *Infrared and Terahertz Detectors, Third Edition*. *Infrared and Terahertz Detectors, Third Edition* (CRC Press, 2019). doi:10.1201/b21951.

[31] Stewart, J. W., Vella, J. H., Li, W., Fan, S. & Mikkelsen, M. H. Ultrafast pyroelectric photodetection with on-chip spectral filters. *Nature Materials* vol. 19 158–162 (2020).

[32] Mauser, K. W. *et al.* Resonant thermoelectric nanophotonics. *Nat. Nanotechnol.* **12**, 770–775 (2017).

[33] Efetov, D. K. *et al.* Fast thermal relaxation in cavity-coupled graphene bolometers with a Johnson noise read-out. *Nat. Nanotechnol.* **13**, 797–801 (2018).

[34] Jones, R. C. The ultimate sensitivity of radiation detectors. *J. Opt. Soc. Am.* **37**, 879–890 (1947).

[35] Lewis, W. B. Fluctuations in streams of thermal radiation. *Proc. Phys. Soc.* **59**, 34–40 (1947).

[36] Wormser, E. M. Properties of Thermistor Infrared Detectors. *J. Opt. Soc. Am.* **43**, 15

(1953).

[37] Golay, M. J. E. The theoretical and practical sensitivity of the pneumatic infra-red detector. *Rev. Sci. Instrum.* **20**, 816–820 (1949).

[38] Rogalski, A. Infrared detectors: An overview. *Infrared Phys. Technol.* **43**, 187–210 (2002).

[39] Rogalski, A., Antoszewski, J. & Faraone, L. Third-generation infrared photodetector arrays. *J. Appl. Phys.* **105**, 091101 (2009).

[40] Datskos, P. G. Detectors: Figures of Merit. in *Encyclopedia of Optical and Photonic Engineering, Second Edition* 1–9 (CRC Press, 2015). doi:10.1081/E-EOE2-120009723.

[41] Rogalski, A. HgCdTe infrared detector material: History, status and outlook. *Reports Prog. Phys.* **68**, 2267–2336 (2005).

[42] Raman, A. P., Anoma, M. A., Zhu, L., Rephaeli, E. & Fan, S. Passive radiative cooling below ambient air temperature under direct sunlight. *Nature* **515**, 540–544 (2014).

[43] Kou, J. long, Jurado, Z., Chen, Z., Fan, S. & Minnich, A. J. Daytime Radiative Cooling Using Near-Black Infrared Emitters. *ACS Photonics* **4**, 626–630 (2017).

[44] Zhai, Y. *et al.* Scalable-manufactured randomized glass-polymer hybrid metamaterial for daytime radiative cooling. *Science (80-.).* **355**, 1062–1066 (2017).

[45] Li, W., Shi, Y., Chen, Z. & Fan, S. Photonic thermal management of coloured objects. *Nat. Commun.* **9**, 4240 (2018).

[46] Coppens, Z. J. & Valentine, J. G. Spatial and Temporal Modulation of Thermal Emission. *Adv. Mater.* **29**, 1701275 (2017).

[47] Gawarikar, A. S., Shea, R. P., Mehdaoui, A. & Talghader, J. J. Radiation heat transfer dominated microbolometers. in *2008 IEEE/LEOS International Conference on Optical MEMS and Nanophotonics, OPT MEMS* 178–179 (2008). doi:10.1109/OMEMS.2008.4607887.

[48] Abdel-Rahman, M. *et al.* Fabrication and design of vanadium oxide microbolometer. in *AIP Conference Proceedings* vol. 1809 020001 (2017).

[49] Middleton, C. F. & Boreman, G. D. Technique for thermal isolation of antenna-coupled infrared microbolometers. *J. Vac. Sci. Technol. B Microelectron. Nanom.*

Struct. **24**, 2356–2359 (2006).

[50] Bhan, R. K., Saxena, R. S., Jalwania, C. R. & Lomash, S. K. Uncooled infrared microbolometer arrays and their characterisation techniques. *Def. Sci. J.* **59**, 580–589 (2009).

[51] Deng, Y. Z., Tang, S. F., Zeng, H. Y., Wu, Z. Y. & Tung, D. K. Experiments on temperature changes of microbolometer under blackbody radiation and predictions using thermal modeling by COMSOL multiphysics simulator. *Sensors (Switzerland)* **18**, (2018).

[52] Schoeman, J. & du Plessis, M. Recent advances in the modelling of the thermal conductance of uncooled microbolometers. *Fourth Conf. Sensors, MEMS, Electro-Optic Syst.* **10036**, 100360B (2017).

[53] Tanrikulu, M. Y. *et al.* Single layer microbolometer detector pixel using ZnO material. in *Proceedings of SPIE* (eds. Fulop, G. F., Hanson, C. M., Norton, P. R., Andresen, B. F. & Miller, J. L.) vol. 1062417 46 (SPIE, 2018).

[54] Dao, T. D. *et al.* Hole Array Perfect Absorbers for Spectrally Selective Midwavelength Infrared Pyroelectric Detectors. *ACS Photonics* **3**, 1271–1278 (2016).

[55] Niesler, F. B. P., Gansel, J. K., Fischbach, S. & Wegener, M. Metamaterial metal-based bolometers. *Appl. Phys. Lett.* **100**, 203508 (2012).

[56] Tucker, E. *et al.* Near-field mapping of dipole nano-antenna-coupled bolometers. *J. Appl. Phys.* **114**, 33109 (2013).

[57] Wu, Y. *et al.* Mid-Infrared Nanometallic Antenna Assisted Silicon Waveguide Based Bolometers. *ACS Photonics* **6**, 3253–3260 (2019).

[58] Monshat, H., Liu, L. & Lu, M. A Narrowband Photo-Thermoelectric Detector Using Photonic Crystal. *Adv. Opt. Mater.* **7**, 1–8 (2019).

[59] Zolotavin, P., Evans, C. & Natelson, D. Photothermoelectric Effects and Large Photovoltages in Plasmonic Au Nanowires with Nanogaps. *J. Phys. Chem. Lett.* **8**, 1739–1744 (2017).

[60] Russer, J. A. *et al.* A nanostructured long-wave infrared range thermocouple detector. *IEEE Trans. Terahertz Sci. Technol.* **5**, 335–343 (2015).

[61] Pan, Y. *et al.* A Rapid Response Thin-Film Plasmonic-Thermoelectric Light Detector. *Sci. Rep.* **6**, (2016).

[62] Kuznetsov, S. A., Paulish, A. G., Navarro-Ciá, M. & Arzhannikov, A. V. Selective Pyroelectric Detection of Millimetre Waves Using Ultra-Thin Metasurface Absorbers. *Sci. Rep.* **6**, 1–11 (2016).

[63] Suen, J. Y. *et al.* Multifunctional metamaterial pyroelectric infrared detectors. *Optica* **4**, 276 (2017).

[64] Lassiter, J. B. *et al.* Plasmonic waveguide modes of film-coupled metallic nanocubes. *Nano Lett.* **13**, 5866–5872 (2013).

[65] Akselrod, G. M. *et al.* Large-Area Metasurface Perfect Absorbers from Visible to Near-Infrared. *Adv. Mater.* **27**, 8028–8034 (2015).

[66] Walter, R. *et al.* Large-area low-cost tunable plasmonic perfect absorber in the near infrared by colloidal etching lithography. *Adv. Opt. Mater.* **3**, 398–403 (2015).

[67] Moreau, A. *et al.* Controlled-reflectance surfaces with film-coupled colloidal nanoantennas. *Nature* **492**, 86–89 (2012).

[68] Zhao, J., Jaber, S., Mulvaney, P., Braun, P. V. & Giessen, H. Repetitive Hole-Mask Colloidal Lithography for the Fabrication of Large-Area Low-Cost Plasmonic Multishape Single-Layer Metasurfaces. *Adv. Opt. Mater.* **3**, 680–686 (2015).

[69] Knight, M. W. *et al.* Aluminum for plasmonics. *ACS Nano* **8**, 834–840 (2014).

[70] Olson, J. *et al.* Vivid, full-color aluminum plasmonic pixels. *Proc. Natl. Acad. Sci. U. S. A.* **111**, 14348–14353 (2014).

[71] Miyata, M., Hatada, H. & Takahara, J. Full-Color Subwavelength Printing with Gap-Plasmonic Optical Antennas. *Nano Lett.* **16**, 3166–3172 (2016).

[72] Olson, J. *et al.* High chromaticity aluminum plasmonic pixels for active liquid crystal displays. *ACS Nano* **10**, 1108–1117 (2016).

[73] Clausen, J. S. *et al.* Plasmonic metasurfaces for coloration of plastic consumer products. *Nano Lett.* **14**, 4499–4504 (2014).

[74] Zhu, X., Vannahme, C., Højlund-Nielsen, E., Mortensen, N. A. & Kristensen, A. Plasmonic colour laser printing. *Nat. Nanotechnol.* **11**, 325–329 (2016).

[75] Kumar, K. *et al.* Printing colour at the optical diffraction limit. *Nat. Nanotechnol.* **7**, 557–561 (2012).

[76] Goh, X. M. *et al.* Three-dimensional plasmonic stereoscopic prints in full colour. *Nat. Commun.* **5**, 1–8 (2014).

[77] Henzie, J., Lee, M. H. & Odom, T. W. Multiscale patterning of plasmonic metamaterials. *Nat. Nanotechnol.* **2**, 549–554 (2007).

[78] James, T. D., Mulvaney, P. & Roberts, A. The plasmonic pixel: Large area, wide gamut color reproduction using aluminum nanostructures. *Nano Lett.* **16**, 3817–3823 (2016).

[79] Wang, L. *et al.* Large Area Plasmonic Color Palettes with Expanded Gamut Using Colloidal Self-Assembly. *ACS Photonics* **3**, 627–633 (2016).

[80] Yu, R. *et al.* Structural Coloring of Glass Using Dewetted Nanoparticles and Ultrathin Films of Metals. *ACS Photonics* **3**, 1194–1201 (2016).

[81] Tan, S. J. *et al.* Plasmonic color palettes for photorealistic printing with aluminum nanostructures. *Nano Lett.* **14**, 4023–4029 (2014).

[82] Chen, T. & Reinhard, B. M. Assembling Color on the Nanoscale: Multichromatic Switchable Pixels from Plasmonic Atoms and Molecules. *Adv. Mater.* **28**, 3522–3527 (2016).

[83] Gu, Y., Zhang, L., Yang, J. K. W., Yeo, S. P. & Qiu, C. W. Color generation via subwavelength plasmonic nanostructures. *Nanoscale* **7**, 6409–6419 (2015).

[84] Chen, Q., Hu, X., Wen, L., Yu, Y. & Cumming, D. R. S. Nanophotonic Image Sensors. *Small* **12**, 4922–4935 (2016).

[85] Maier, S. A. Plasmonic field enhancement and SERS in the effective mode volume picture. *Opt. Express* **14**, 1957 (2006).

[86] Siegfried, T., Ekinci, Y., Martin, O. J. F. & Sigg, H. Gap plasmons and near-field enhancement in closely packed sub-10 nm gap resonators. *Nano Lett.* **13**, 5449–5453 (2013).

[87] Ciracì, C. *et al.* Probing the ultimate limits of plasmonic enhancement. *Science (80-.).* **337**, 1072–1074 (2012).

[88] Rose, A. *et al.* Control of radiative processes using tunable plasmonic nanopatch

antennas. *Nano Lett.* **14**, 4797–4802 (2014).

[89] Schuller, J. A. *et al.* Plasmonics for extreme light concentration and manipulation. *Nat. Mater.* **9**, 193–204 (2010).

[90] Hess, O. *et al.* Active nanoplasmonic metamaterials. *Nature Materials* vol. 11 573–584 (2012).

[91] Bai, Q., Perrin, M., Sauvan, C., Hugonin, J.-P. & Lalanne, P. Efficient and intuitive method for the analysis of light scattering by a resonant nanostructure. *Opt. Express* **21**, 27371 (2013).

[92] Walter, R. *et al.* Large-area low-cost tunable plasmonic perfect absorber in the near infrared by colloidal etching lithography. *Adv. Opt. Mater.* **3**, 398–403 (2015).

[93] Tittl, A. *et al.* Palladium-based plasmonic perfect absorber in the visible wavelength range and its application to hydrogen sensing. *Nano Lett.* **11**, 4366–4369 (2011).

[94] Bowen, P. T. & Smith, D. R. Coupled-mode theory for film-coupled plasmonic nanocubes. *Phys. Rev. B - Condens. Matter Mater. Phys.* **90**, 195402 (2014).

[95] Alaee, R., Albooyeh, M. & Rockstuhl, C. Theory of metasurface based perfect absorbers. *J. Phys. D. Appl. Phys.* **50**, 503002 (2017).

[96] Hao, J. *et al.* High performance optical absorber based on a plasmonic metamaterial. *Appl. Phys. Lett.* **96**, 48–51 (2010).

[97] Fang, Z., Zhen, Y. R., Fan, L., Zhu, X. & Nordlander, P. Tunable wide-angle plasmonic perfect absorber at visible frequencies. *Phys. Rev. B - Condens. Matter Mater. Phys.* **85**, 245401 (2012).

[98] Cheng, F., Yang, X. & Gao, J. Enhancing refractive index sensing capability with infrared plasmonic perfect absorbers. *Conf. Lasers Electro-Optics Eur. - Tech. Dig.* **2014-Janua**, 3185 (2014).

[99] Avitzour, Y., Urzhumov, Y. A. & Shvets, G. Wide-angle infrared absorber based on a negative-index plasmonic metamaterial. *Phys. Rev. B - Condens. Matter Mater. Phys.* **79**, 1–5 (2009).

[100] Baumberg, J. J., Aizpurua, J., Mikkelsen, M. H. & Smith, D. R. Extreme nanophotonics from ultrathin metallic gaps. *Nat. Mater.* **18**, 668–678 (2019).

[101] Chen, B. *et al.* Flat metallic surface gratings with sub-10 nm gaps controlled by atomic-layer deposition. *Nanotechnology* **27**, (2016).

[102] Abedini Dereshgi, S., Ghobadi, A., Hajian, H., Butun, B. & Ozbay, E. Ultra-Broadband, Lithography-Free, and Large-Scale Compatible Perfect Absorbers: The Optimum Choice of Metal layers in Metal-Insulator Multilayer Stacks. *Sci. Rep.* **7**, 14872 (2017).

[103] Ghobadi, A., Hajian, H., Butun, B. & Ozbay, E. Strong Light-Matter Interaction in Lithography-Free Planar Metamaterial Perfect Absorbers. *ACS Photonics* **5**, 4203–4221 (2018).

[104] Ding, F., Mo, L., Zhu, J. & He, S. Lithography-free, broadband, omnidirectional, and polarization-insensitive thin optical absorber. *Appl. Phys. Lett.* **106**, 61108 (2015).

[105] Kats, M. A., Blanchard, R., Genevet, P. & Capasso, F. Nanometre optical coatings based on strong interference effects in highly absorbing media. *Nat. Mater.* **12**, 20–24 (2013).

[106] Kats, M. A. *et al.* Ultra-thin perfect absorber employing a tunable phase change material. *Appl. Phys. Lett.* **101**, 221101 (2012).

[107] Li, Z., Butun, S. & Aydin, K. Large-area, Lithography-free super absorbers and color filters at visible frequencies using ultrathin metallic films. *ACS Photonics* **2**, 183–188 (2015).

[108] Wu, C. *et al.* Large-area wide-angle spectrally selective plasmonic absorber. *Phys. Rev. B - Condens. Matter Mater. Phys.* **84**, 1–7 (2011).

[109] Franklin, D., Frank, R., Wu, S. T. & Chanda, D. Actively addressed single pixel full-colour plasmonic display. *Nat. Commun.* **8**, 1–10 (2017).

[110] Akselrod, G. M. *et al.* Large-Area Metasurface Perfect Absorbers from Visible to Near-Infrared. *Adv. Mater.* **27**, 8028–8034 (2015).

[111] Ding, T., Herrmann, L. O., De Nijs, B., Benz, F. & Baumberg, J. J. Self-aligned colloidal lithography for controllable and tuneable plasmonic nanogaps. *Small* **11**, 2139–2143 (2015).

[112] Stewart, J. W., Akselrod, G. M., Smith, D. R. & Mikkelsen, M. H. Toward Multispectral Imaging with Colloidal Metasurface Pixels. *Adv. Mater.* **29**, 1602971

(2017).

[113] Moreau, A. *et al.* Controlled-reflectance surfaces with film-coupled colloidal nanoantennas. *Nature* **492**, 86–89 (2012).

[114] Sykes, M. E. *et al.* Enhanced generation and anisotropic Coulomb scattering of hot electrons in an ultra-broadband plasmonic nanopatch metasurface. *Nat. Commun.* **8**, 986 (2017).

[115] Mock, J. J. *et al.* Distance-dependent plasmon resonant coupling between a gold nanoparticle and gold film. *Nano Lett.* **8**, 2245–2252 (2008).

[116] Wang, Y., Zheng, Y., Huang, C. Z. & Xia, Y. Synthesis of Ag nanocubes 18-32 nm in edge length: The effects of polyol on reduction kinetics, size control, and reproducibility. *J. Am. Chem. Soc.* **135**, 1941–1951 (2013).

[117] Hoang, T. B., Huang, J. & Mikkelsen, M. H. Colloidal synthesis of nanopatch antennas for applications in plasmonics and nanophotonics. *J. Vis. Exp.* **2016**, 1–8 (2016).

[118] Zhang, Q. *et al.* Seed-Mediated Synthesis of Ag Nanocubes with Controllable Edge Lengths in the Range of 30-200 nm and Comparison of Their Optical Properties. *J. Am. Chem. Soc.* **132**, 11372–11378 (2010).

[119] Lin, Q. Y. *et al.* Strong Coupling between Plasmonic Gap Modes and Photonic Lattice Modes in DNA-Assembled Gold Nanocube Arrays. *Nano Lett.* **15**, 4699–4703 (2015).

[120] Kong, X. T., Khosravi Khorashad, L., Wang, Z. & Govorov, A. O. Photothermal Circular Dichroism Induced by Plasmon Resonances in Chiral Metamaterial Absorbers and Bolometers. *Nano Lett.* **18**, 2001–2008 (2018).

[121] Spitzer, F. *et al.* Enhancement of electron hot spot relaxation in photoexcited plasmonic structures by thermal diffusion. *Phys. Rev. B* **94**, 201118 (2016).

[122] Ogawa, S., Okada, K., Fukushima, N. & Kimata, M. Wavelength selective uncooled infrared sensor by plasmonics. *Appl. Phys. Lett.* **100**, 021111 (2012).

[123] Hoang, T. B. & Mikkelsen, M. H. Broad electrical tuning of plasmonic nanoantennas at visible frequencies. *Appl. Phys. Lett.* **108**, 183107 (2016).

[124] Peng, J. *et al.* Scalable electrochromic nanopixels using plasmonics. *Sci. Adv.* **5**,

eaaw2205 (2019).

[125] Tittl, A. *et al.* A Switchable Mid-Infrared Plasmonic Perfect Absorber with Multispectral Thermal Imaging Capability. *Adv. Mater.* **27**, 4597–4603 (2015).

[126] Wilson, W. M., Stewart, J. W. & Mikkelsen, M. H. Surpassing Single Line Width Active Tuning with Photochromic Molecules Coupled to Plasmonic Nanoantennas. *Nano Lett.* **18**, 853–858 (2018).

[127] Huang, Y. W. *et al.* Gate-Tunable Conducting Oxide Metasurfaces. *Nano Lett.* **16**, 5319–5325 (2016).

[128] König, T. A. F. *et al.* Electrically tunable plasmonic behavior of nanocube-polymer nanomaterials induced by a redox-active electrochromic polymer. *ACS Nano* **8**, 6182–6192 (2014).

[129] Xiong, K. *et al.* Switchable Plasmonic Metasurfaces with High Chromaticity Containing only Abundant Metals. *Nano Lett.* **17**, 7033–7039 (2017).

[130] Yao, Y. *et al.* Broad electrical tuning of graphene-loaded plasmonic antennas. *Nano Lett.* **13**, 1257–1264 (2013).

[131] Gutruf, P. *et al.* Mechanically tunable dielectric resonator metasurfaces at visible frequencies. *ACS Nano* **10**, 133–141 (2016).

[132] Huang, F. & Baumberg, J. J. Actively tuned plasmons on elastomerically driven Au nanoparticle dimers. *Nano Lett.* **10**, 1787–1792 (2010).

[133] Duan, X., Kamin, S. & Liu, N. Dynamic plasmonic colour display. *Nat. Commun.* **8**, 1–4 (2017).

[134] Strohfeldt, N. *et al.* Yttrium hydride nanoantennas for active plasmonics. *Nano Lett.* **14**, 1140–1147 (2014).

[135] Shao, L., Zhuo, X. & Wang, J. Advanced Plasmonic Materials for Dynamic Color Display. *Adv. Mater.* **30**, 1–18 (2018).

[136] Michel, A. K. U. *et al.* Reversible Optical Switching of Infrared Antenna Resonances with Ultrathin Phase-Change Layers Using Femtosecond Laser Pulses. *ACS Photonics* **1**, 833–839 (2014).

[137] Yang, Y. *et al.* Femtosecond optical polarization switching using a cadmium oxide-based perfect absorber. *Nat. Photonics* **11**, 390–395 (2017).

[138] Kats, M. A. *et al.* Thermal tuning of mid-infrared plasmonic antenna arrays using a phase change material. *Opt. Lett.* **38**, 368 (2013).

[139] Huang, J., Traverso, A. J., Yang, G. & Mikkelsen, M. H. Real-Time Tunable Strong Coupling: From Individual Nanocavities to Metasurfaces. *ACS Photonics* **6**, 838–843 (2019).

[140] Sautter, J. *et al.* Active tuning of all-dielectric metasurfaces. *ACS Nano* **9**, 4308–4315 (2015).

[141] Yin, X. *et al.* Beam switching and bifocal zoom lensing using active plasmonic metasurfaces. *Light Sci. Appl.* **6**, e17016–e17016 (2017).

[142] Rensberg, J. *et al.* Active Optical Metasurfaces Based on Defect-Engineered Phase-Transition Materials. *Nano Lett.* **16**, 1050–1055 (2016).

[143] Driscoll, T. *et al.* Dynamic tuning of an infrared hybrid-metamaterial resonance using vanadium dioxide. *Appl. Phys. Lett.* **93**, (2008).

[144] Wang, G., Chen, X., Liu, S., Wong, C. & Chu, S. Mechanical Chameleon through Dynamic Real-Time Plasmonic Tuning. *ACS Nano* **10**, 1788–1794 (2016).

[145] Baudrion, A. L. *et al.* Reversible strong coupling in silver nanoparticle arrays using photochromic molecules. *Nano Lett.* **13**, 282–286 (2013).

[146] Schwartz, T., Hutchison, J. A., Genet, C. & Ebbesen, T. W. Reversible Switching of Ultrastrong Light-Molecule Coupling. *Phys. Rev. Lett.* **106**, 196405 (2011).

[147] Zheng, Y. B., Kiraly, B., Cheunkar, S., Huang, T. J. & Weiss, P. S. Incident-angle-modulated molecular plasmonic switches: A case of weak exciton-plasmon coupling. *Nano Lett.* **11**, 2061–2065 (2011).

[148] Pala, R. A., Shimizu, K. T., Melosh, N. A. & Brongersma, M. L. A nonvolatile plasmonic switch employing photochromic molecules. *Nano Lett.* **8**, 1506–1510 (2008).

[149] Chikkaraddy, R. *et al.* How Ultranarrow Gap Symmetries Control Plasmonic Nanocavity Modes: From Cubes to Spheres in the Nanoparticle-on-Mirror. *ACS Photonics* **4**, 469–475 (2017).

[150] Tork, A. *et al.* Photochromic behavior of spiropyran in polymer matrices. *Appl. Opt.* **40**, 1180 (2001).

[151] Klajn, R. Spiropyran-based dynamic materials. *Chem. Soc. Rev.* **43**, 148–184 (2014).

[152] Cai, T., Bose, R., Solomon, G. S. & Waks, E. Controlled coupling of photonic crystal cavities using photochromic tuning. *Appl. Phys. Lett.* **102**, (2013).

[153] Sridharan, D., Waks, E., Solomon, G. & Fourkas, J. T. Reversible tuning of photonic crystal cavities using photochromic thin films. *Appl. Phys. Lett.* **96**, (2010).

[154] Herder, M. *et al.* Improving the fatigue resistance of diarylethene switches. *J. Am. Chem. Soc.* **137**, 2738–2747 (2015).

[155] Buback, J. *et al.* Ultrafast bidirectional photoswitching of a spiropyran. *J. Am. Chem. Soc.* **132**, 16510–16519 (2010).

[156] Chain, E. E. Optical properties of vanadium dioxide and vanadium pentoxide thin films. *Appl. Opt.* **30**, 2782 (1991).

[157] Zhou, Y. *et al.* Voltage-triggered ultrafast phase transition in vanadium dioxide switches. *IEEE Electron Device Lett.* **34**, 220–222 (2013).

[158] Kocer, H. *et al.* Thermal tuning of infrared resonant absorbers based on hybrid gold-VO 2 nanostructures. *Appl. Phys. Lett.* **106**, 161104 (2015).

[159] Song, Z., Wang, K., Li, J. & Liu, Q. H. Broadband tunable terahertz absorber based on vanadium dioxide metamaterials. *Opt. Express* **26**, 7148 (2018).

[160] Wang, S., Kang, L. & Werner, D. H. Hybrid Resonators and Highly Tunable Terahertz Metamaterials Enabled by Vanadium Dioxide (VO2). *Sci. Rep.* **7**, 1–8 (2017).

[161] Xu, G., Chen, Y., Tazawa, M. & Jin, P. Surface plasmon resonance of silver nanoparticles on vanadium dioxide. *J. Phys. Chem. B* **110**, 2051–2056 (2006).

[162] Shu, F. Z. *et al.* Dynamic Plasmonic Color Generation Based on Phase Transition of Vanadium Dioxide. *Adv. Opt. Mater.* **6**, 1–10 (2018).

[163] Kakiuchida, H., Jin, P., Nakao, S. & Tazawa, M. Optical properties of vanadium dioxide film during semiconductive-metallic phase transition. *Japanese J. Appl. Physics, Part 2 Lett.* **46**, (2007).

[164] Earl, S. K. *et al.* Tunable optical antennas enabled by the phase transition in vanadium dioxide. *Opt. Express* **21**, 27503 (2013).

[165] Dicken, M. J. *et al.* Frequency tunable near-infrared metamaterials based on VO_2 phase transition. *Opt. Express* **17**, 18330 (2009).

[166] Muskens, O. L. *et al.* Antenna-assisted picosecond control of nanoscale phase transition in vanadium dioxide. *Light Sci. Appl.* **5**, e16173-9 (2016).

[167] Koethe, T. C. *et al.* Transfer of spectral weight and symmetry across the metal-insulator transition in VO2. *Phys. Rev. Lett.* **97**, 1–4 (2006).

[168] Akselrod, G. M. *et al.* Large-Area Metasurface Perfect Absorbers from Visible to Near-Infrared. *Adv. Mater.* **27**, 8028–8034 (2015).

[169] Currie, M. *et al.* Asymmetric hysteresis in vanadium dioxide thin films. *Opt. Mater. Express* **9**, 3717 (2019).

[170] Currie, M., Mastro, M. A. & Wheeler, V. D. Characterizing the tunable refractive index of vanadium dioxide. *Opt. Mater. Express* **7**, 1697 (2017).

[171] Goldsmith, J. H., Vangala, S., Hendrickson, J. R., Cleary, J. W. & Vella, J. H. Long-wave infrared selective pyroelectric detector using plasmonic near-perfect absorbers and highly oriented aluminum nitride. *J. Opt. Soc. Am. B* **34**, 1965 (2017).

[172] Suen, J. Y. *et al.* Multifunctional metamaterial pyroelectric infrared detectors. *Optica* **4**, 276 (2017).

[173] Jung, J. Y. *et al.* Infrared broadband metasurface absorber for reducing the thermal mass of a microbolometer. *Sci. Rep.* **7**, 430 (2017).

[174] Ogawa, S. & Kimata, M. Wavelength- or polarization-selective thermal infrared detectors for multi-color or polarimetric imaging using plasmonics and metamaterials. *Materials (Basel).* **10**, 493 (2017).

[175] Stotlar, S. C. & McLellan, E. J. Developments In High-Speed Pyroelectric Detectors. *Opt. Eng.* **20**, 469–471 (1981).

[176] Roundy, C. B. & Byer, R. L. Subnanosecond pyroelectric detector. *Appl. Phys. Lett.* **21**, 512–515 (1972).

[177] Kreis, K., Potestio, R., Kremer, K. & Fogarty, A. C. Adaptive Resolution Simulations with Self-Adjusting High-Resolution Regions. *J. Chem. Theory Comput.* **12**, 4067–4081 (2016).

[178] Vieira, M. R. & Tsotras, V. J. Flexible pattern queries. *SpringerBriefs Comput. Sci.* **6**,

5–35 (2013).

[179] Peng, W. *et al.* Enhanced Performance of a Self-Powered Organic/Inorganic Photodetector by Pyro-Phototronic and Piezo-Phototronic Effects. *Adv. Mater.* **29**, 1–9 (2017).

[180] Lang, S. B. The history of pyroelectricity: From ancient greece to space missions. *Ferroelectrics* **230**, 99–108 (1999).

[181] Lang, S. B. Pyroelectricity: From ancient curiosity to modern imaging tool. *Phys. Today* **58**, 31–36 (2005).

[182] Roundy, C. B. Performance and Uses of High Speed Pyroelectric Detectors. *SPIE Semin Proc* **62**, 191–198 (1975).

[183] Liu, S. T. & Long, D. Pyroelectric Detectors and Materials. *Proc. IEEE* **66**, 14–26 (1978).

[184] Kumar, M., Patel, M., Lee, G. N. & Kim, J. Light-Induced All-Transparent Pyroelectric Photodetector. *ACS Appl. Nano Mater.* **1**, 319–324 (2018).

[185] Doan, A. T. *et al.* A MEMS-based quad-wavelength hybrid plasmonic-pyroelectric infrared detector. *Micromachines* **10**, 1–12 (2019).

[186] Kuznetsov, S. A., Paulish, A. G., Navarro-Ciá, M. & Arzhannikov, A. V. Selective Pyroelectric Detection of Millimetre Waves Using Ultra-Thin Metasurface Absorbers. *Sci. Rep.* **6**, (2016).

[187] Brownridge, J. D. Pyroelectric X-ray generator. *Nature* **358**, 287–288 (1992).

[188] Naranjo, B., Gimzewski, J. K. & Putterman, S. Observation of nuclear fusion driven by a pyroelectric crystal. *Nature* **434**, 1115–1117 (2005).

[189] Jachalke, S. *et al.* How to measure the pyroelectric coefficient? *Appl. Phys. Rev.* **4**, 21303 (2017).

[190] Spitzer, F. *et al.* Enhancement of electron hot spot relaxation in photoexcited plasmonic structures by thermal diffusion. *Phys. Rev. B* **94**, 201118 (2016).

[191] Yan, W. S. *et al.* Temperature dependence of the pyroelectric coefficient and the spontaneous polarization of AlN. *Appl. Phys. Lett.* **90**, 212102 (2007).

[192] Crisman, E. E., Derov, J. S., Drehman, A. J. & Gregory, O. J. Large pyroelectric

response from reactively sputtered aluminum nitride thin films. *Electrochem. Solid-State Lett.* **8**, H31 (2005).

[193] Fuflyigin, V., Salley, E., Osinsky, A. & Norris, P. Pyroelectric properties of AIN. *Appl. Phys. Lett.* **77**, 3075–3077 (2000).

[194] Ebrahim, S., Elshaer, A. M., Soliman, M. & Tayl, M. B. Pyroelectric infrared detector based on polyaniline/polyvinylidene fluoride blend. *Sensors Actuators, A Phys.* **238**, 389–396 (2016).

[195] De Iacovo, A., Venettacci, C., Colace, L., Scopa, L. & Foglia, S. Noise performance of PbS colloidal quantum dot photodetectors. *Appl. Phys. Lett.* **111**, (2017).

[196] Xu, X. *et al.* High-Performance Near-IR Photodetector Using Low-Bandgap MA0.5FA0.5Pb0.5Sn0.5I3 Perovskite. *Adv. Funct. Mater.* **27**, 1–6 (2017).

[197] Casalino, M. *et al.* Vertically Illuminated, Resonant Cavity Enhanced, Graphene-Silicon Schottky Photodetectors. *ACS Nano* **11**, 10955–10963 (2017).

[198] Gao, Y. *et al.* Photon-trapping microstructures enable high-speed high-efficiency silicon photodiodes. *Nat. Photonics* **11**, 301–308 (2017).

[199] Sakoğlu, Ü., Tyo, J. S., Hayat, M. M., Raghavan, S. & Krishna, S. Spectrally adaptive infrared photodetectors with bias-tunable quantum dots. *J. Opt. Soc. Am. B* **21**, 7 (2004).

[200] Bao, J. & Bawendi, M. G. A colloidal quantum dot spectrometer. *Nature* **523**, 67–70 (2015).

Biography

Jon W. Stewart is a National Defense Science and Engineering Graduate (NDSEG) Fellow in the group of Prof. Maiken H. Mikkelsen in the Electrical and Computer Engineering Department of Duke University. Prior to his graduate studies, he worked at Lockheed Martin's Advanced Technology Center developing LiDAR and MWIR camera payloads for space-born systems. He graduated summa cum laude with his B.S. in Engineering Physics and his B.S. in Electrical Engineering in 2014 from the University of Colorado at Boulder.

Published Papers

1. J.W. Stewart, N.C. Wilson, M.H. Mikkelsen, "Nanophotonic Absorbers Enhance Thermally Sensitive Photodetectors." **ACS Photonics**, under preparation (2020).

2. J.W. Stewart, T. Nebabu, M.H. Mikkelsen, "Control of Nanoscale Heat Generation with Lithography-Free Metasurface Absorbers." **Advanced Materials**, submitted (2020).

3. A.M. Boyce, J.W. Stewart, V.D. Wheeler, M.H. Mikkelsen, "Actively Tunable Metasurfaces via Plasmonic Nanogap Cavities with sub-10 nm VO2 Films." **Nano Letters**, under review (2020).

4. J.W. Stewart, J.H. Vella, W. Li, S. Fan, M.H. Mikkelsen, "Ultrafast Pyroelectric Photodetection with On-Chip Spectral Filters." **Nature Materials** 19, 158 (2020).

5. W.M. Wilson, J.W. Stewart, M.H. Mikkelsen, “Surpassing Single-Linewidth Active Tuning with Photochromic Molecules Coupled to Plasmonic Nanoantennas.” **Nano Letters** 18, 853 (2017).
6. M.E. Skyes, J.W. Stewart, et al. “Ultra-Broadband Hot Electron Response Dynamics in a Plasmonic Metasurface.” **Nature Communications** 8, 986 (2017).
7. J.W. Stewart, G.M. Akselrod, D.R. Smith, M.H. Mikkelsen, “Toward Multispectral Imaging with Colloidal Metasurface Pixels.” **Advanced Materials** 29, 1602971 (2017).